Characterization of Furan- and Thiophene-containing Bispyridyl Oligomers via Spectroscopic, Electrochemical, and TD-DFT Methods

*April E. Steen,[‡] Thomas L. Ellington,[‡] Suong T. Nguyen,[‡] Sivaraman Balasubramaniam, Indika Chandrasiri, Jared H. Delcamp, Gregory S. Tschumper, Nathan I. Hammer, and Davita L. Watkins**

Department of Chemistry and Biochemistry, University of Mississippi, University, Mississippi 38677

ABSTRACT. The study of π-conjugated oligomers has garnered significant interest due to their use in organic optoelectronic devices, such as organic light-emitting diodes or organic field-effect transistors. Herein we varied the inner heterocyclic units of pyridyl (Pyr) capped π-conjugated oligomers consisting of furan (F) and thiophene (T) subunits to afford homomeric (**Pyr$_2$F$_3$** and **Pyr$_2$T$_3$**) and heteromeric (**Pyr$_2$F$_2$T** and **Pyr$_2$T$_2$F**) molecules as applicable semiconducting building blocks. The oligomers were synthesized, and their solution and solid-state spectroscopic properties were characterized. Compared to their thiophene congeners, oligomers with furans directly attached to the pyridyl moieties (**Pyr$_2$F$_3$** and **Pyr$_2$F$_2$T**) gave rise to larger solution state quantum yields and optical band gaps. Oligomers possessing a central furan subunit (**Pyr$_2$F$_3$** and **Pyr$_2$T$_2$F**),

on the other hand, were found to be nearly non-emissive in the solid-state, which is attributed to non-radiative decay likely caused by π-π stacking interactions. Unlike the **Pyr$_2$T$_2$F** hybrid oligomer, **Pyr$_2$F$_2$T** not only exhibited a comparatively high solution-state quantum yield (7%), but also the brightest solid-state quantum yield emission (5%) and photostability (98%) when evaluated under ambient conditions. Density functional theory (DFT) computations support these trends, indicating the largest HOMO-LUMO energy gaps and optical band gaps are possessed by **Pyr$_2$F$_3$** and **Pyr$_2$F$_2$T**, while those of **Pyr$_2$T$_2$F** and **Pyr$_2$T$_3$** are the lowest among the oligomers considered here (*i.e.*, **Pyr$_2$F$_3$** > **Pyr$_2$F$_2$T** > **Pyr$_2$T$_2$F** > **Pyr$_2$T$_3$**). These results suggest that hybrid furan-thiophene oligomers—like that of **Pyr$_2$F$_2$T**—could serve as viable building blocks for optoelectronic devices, while possessing the positive attributes of both individual heterocycles in a synergistic manner.

INTRODUCTION

In the field of electronic devices, much attention has been given to π-conjugated organic molecules as low-cost and flexible alternatives to silicon-based devices. Such conjugated systems can be used to create a variety of optoelectronic devices such as organic photovoltaics (OPVs), organic light-emitting diodes (OLEDs), or organic field effect transistors (OFETs). These electrically conducting molecules possess HOMO-LUMO energy gaps ranging from *ca.* 1.5 eV to 3.0 eV and rigid π-conjugated backbones suitable for charge delocalization.[1-2] Numerous reports have been published highlighting the design of semiconducting materials, focusing on either the polymer or the oligomer.[1, 3] Many of these accounts employ subtle synthetic modifications within the π-conjugated backbone that afford significant changes in optoelectronic properties.[4] Due to its synthetic acces-

sibility, one of the most common building blocks used in the development of organic semiconducting materials is the sulfur-containing heterocycle thiophene.[5] Although thiophene-containing molecules are ubiquitous organic materials, they tend to suffer from low solubility and inefficient luminescence.[6]

More recently, studies have emerged focusing on their close analogues, oligofurans.[2, 5, 7-14] The presence of an oxygen atom instead of a sulfur atom in these five-membered aromatic heterocycles gives rise to electron-rich conjugated systems exhibiting tighter solid-state packing and greater rigidity when compared to those of thiophene analogues.[2, 15] In-depth analysis of oligofurans and oligothiophenes indicates that furan is smaller in molecular size than that of thiophene. This is a consequence of the greater atomic radius of sulfur compared to that of oxygen, 180 pm and 152 pm respectively.[16] While oligothiophenes experience more steric interactions and are twisted out of plane by roughly 20°, oligofurans possess high rigidity, planarity,[17] and low aromaticity,[18-19] yielding extensive charge delocalization. In addition, the furan molecule exhibits a larger dipole moment compared to that of thiophene, resulting in higher solubility in both nonpolar and polar solvents and higher fluorescence emission.[20] Compared to oligothiophenes, the ability of oligofurans to maintain better solubility in common organic solvents reduces the need for solubilizing side chains typically needed for solution processing. Such solubilizing alkyl chains complicate molecular interactions and disrupt π–π interactions, leading to decreased intermolecular interactions needed for charge migration.[21-22] Furthermore, furan is available from a variety of natural products, making it a renewable and sustainable synthetic resource.[11]

Oligofurans, however, have their own shortcomings; they possess relatively high HOMO-LUMO gaps (3.2-3.7 eV) and high-lying HOMOs, making them more susceptible to decomposition.[23-25] This relative instability can be overcome by the incorporation of thiophene building

blocks to form fused and/or alternating hybrid systems, in turn mitigating the decomposition inherent to the furan while also lowering the HOMO-LUMO energy gap.[24, 26-27] Improving upon the innate properties and increasing the stability of furan-based building blocks would allow for the production of stable high-performing materials that would be influential towards the design of new semiconducting constituents for device application.[11]

Herein, we describe the synthesis and comparative analysis of photophysical properties for novel hybrid oligomers. The molecules of interest are pyridyl capped alternating furan/thiophene (*i.e.,* heteromeric or hybrid) derivatives and their previously synthesized homomeric (*i.e.*, repeating thiophene or furan subunits) controls.[28,29] These oligomers (Figure 1), originally designed for coordination chemistry, have been selected since polymers are typically less amenable to molecular level tailoring and to characterization accuracies allowing for the precise comparison of materials that exhibit even subtle changes in properties due to structure variation. Systematic studies of the HOMO-LUMO energies via DFT calculations, cyclic voltammetry (CV), and absorption/emission spectroscopy are employed to comparatively explore the optical properties of these hybrid π-conjugated oligomers (*i.e.*, **Pyr$_2$F$_2$T** and **Pyr$_2$T$_2$F**) to their homomeric congeners (*i.e.*, **Pyr$_2$F$_3$** and **Pyr$_2$T$_3$**). This prescription provides a bottom-up approach when investigating oligofuran-based organic optoelectronic devices and their structural and electronic properties.

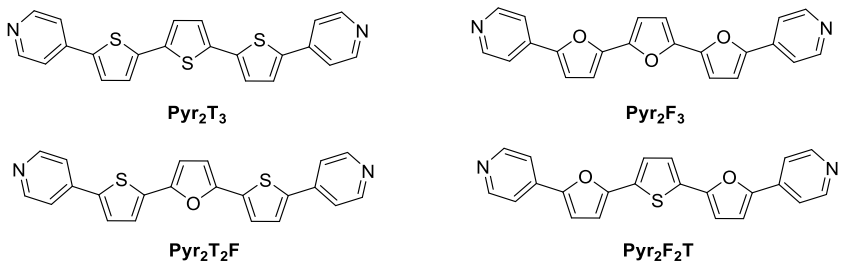

Figure 1. Molecular structures of each pyridyl-based homomeric and hybrid π-conjugated oligomer.

EXPERIMENTAL METHODS

Synthetic. Reagents and solvents were purchased from commercial sources and used without further purification unless otherwise specified. Tetrahydrofuran (THF), ether, dichloromethane (DCM), and dimethylformamide (DMF) were degassed in 20 L drums and passed through two sequential purification columns (activated alumina; molecular sieves for DMF) under a positive argon atmosphere. Thin layer chromatography (TLC) was performed on SiO_2-60 F254 aluminum plates with visualization by ultraviolet (UV) light or staining. Flash column chromatography was performed using Purasil SiO_2-60, 230–400 mesh from Whatman. Additional synthetic details can be found in the Supporting Information (SI).

Computational. Full geometry optimizations and harmonic vibrational frequency computations were performed on each ground state (S_0) oligomer (*i.e.*, **Pyr$_2$F$_3$**, **Pyr$_2$F$_2$T**, **Pyr$_2$T$_2$F**, and **Pyr$_2$T$_3$**) depicted in Figure 1 with the hybrid B3LYP[30-32] density functional in conjunction with a split-valence triple-ζ quality 6-311G(2*df*, 2*pd*) basis set.[33-34] This set of computations provides HOMO-LUMO energy gaps (E_g^{DFT}) which serve as approximations to the fundamental energy gaps.

A subsequent set of time-dependent density functional theory (TD-DFT)[35-38] single point energy computations were carried out using the S_0 structures and the same level of theory in order to estimate the vertical excitation energies ($E_{1\leftarrow0}^{vert}$), the maximum absorption wavelengths ($\lambda_{1\leftarrow0}^{vert}$), and the absorption spectra corresponding to the ten lowest lying singlet excited states (S_1).[39] Full TD-DFT geometry optimizations were also performed on the S_1 surface for each oligomer starting from the S_0 optimized structures. These optimized excited state structures were used to simulate the emission spectrum of each S_1 oligomer. The nature of the electronic transitions was determined from a set of natural orbital analyses that were performed at the B3LYP/6-311G(2*df*, 2*pd*) level of

theory on each ground and excited state oligomer. These prescriptions are based on the extensive calibration by Jacquemin and coworkers.[40]

The aforementioned computations provided a means for comparing the trends in the experimental and computational data. Additional computational details, as well as the optimized Cartesian coordinates (in Å), torsional angles, theoretically calculated absorption and emission spectra, and molecular orbital plots are reported in the SI.

Electrochemical Analysis. Cyclic voltammetry (CV) measurements were performed on a CH Instruments CHI-610E Analyzer potentiostat/galvanostat. All cyclic voltammograms were collected under argon blanket with doubly distilled DMF, which was degassed with argon just before use. Tetrabutylammonium hexafluorophosphate (Bu_4NPF_6) was used as the background electrolyte at a concentration of 0.10 mol dm^{-3} (M). A glassy carbon working electrode of surface area 50 μm^2, a platinum-wire counter electrode, and an Ag/AgCl/KCl (aq., sat.) reference electrode were used with a scan rate of 100 mV/second. Approximately 2 mg of sample in 3 mL of solution was used for each CV reported. **Pyr_2T_3** had a dramatically lower solubility likely leading to a lower concentration in solution. After data was collected, ferrocene was added, and a second CV taken with the internal standard to ensure no reference electrode drift had taken place during these measurements.

Values are reported versus a normal hydrogen electrode (NHE) with ferrocene taken as 0.70 V vs. NHE. $E_{(S+/S)}$ onset is reported by drawing a tangent line intercepting with scan flat region. An experimental estimate of the HOMO and LUMO energy levels for each molecule was obtained from the onset oxidation potential ($E_{ox(onset)}$) and the onset reduction potential ($E_{red(onset)}$) as follows: HOMO = –[4.4 V–$E_{Ox(onset)}$]; LUMO = –[4.4 V–$E_{red(onset)}$]; E_g^{CV} = LUMO–HOMO.[41] The corresponding voltammogram for each oligomer is reported in the SI.

Spectroscopic. Solutions of each of the four compounds were created using either HiPerSolv CHROMANORM toluene from BDH Analytical Chemicals or DMF from Fisher Scientific. To promote dissolution of solid, sonication was performed for 15 minutes. Argon was bubbled through each solution for one minute to remove oxygen. Solutions were prepared immediately before performing spectroscopic analyses.

UV-Vis absorption spectra were obtained using an Agilent 5000 UV-Vis NIR spectrometer. Solid-state absorbance (diffuse reflectance) spectra were obtained by directing light from a Xenon arc lamp onto the sample, which was placed inside a Stellar Net Inc. IC2 integrating sphere. The reflected light was collected using a solarization resistant fiber optic cable and was directed into an Ocean Optics USB2000 spectrometer for analysis. The obtained spectra were compared to a standard of Spectralon® in order to calculate the percent reflectivity, and these values were used in conjunction with the Kubelka-Munk function in order to generate the diffuse reflectance spectra.[42-43]

The fluorescence emission for both solid- and solution-states was obtained using a Nikon TE2000U inverted microscope with CCD detection with a pulsed 405 nm picosecond diode laser for excitation. Excited-state lifetimes were also obtained using a Nikon TE2000U inverted microscope and a PMD series single photon avalanche diode from PicoQuant with a 50 ps timing resolution in conjunction with a pulsed 405 nm ps diode laser. These values were fit to single exponential decay functions in order to calculate the lifetimes (τ). Solutions in DMF and toluene were prepared to compare the fluorescence emission and lifetimes between solutions. To measure the fluorescence photostability of the solid, the sample was irradiated for 6 hours with 405 nm excitation obtained by passing light from a xenon arc lamp through a monochromator. Emitted light was collected using a fiber optic cable and passed into an ACTON SpectraPro 2150i photodiode array.

One spectrum was obtained every minute for the duration of the experiment. The integrated emission of the final spectrum was divided by the integrated emission of the first spectrum to calculate percent photostability.[42]

Spectra for the determination of the absolute quantum yield of the solid-state (Φ_{solid}) were obtained over the range 200–1025 nm using the aforementioned integrating sphere, xenon lamp, monochromator selecting for 405 nm light, and an Ocean Optics Flame Series spectrometer. The sample was suspended in the center of the integrating sphere and light was passed through a port in order to illuminate the sample. The emission of the light source and the sample were collected and compared to a blank spectrum. The integrated area of the sample emission spectrum was divided by the integrated area of the light source emission spectrum in order to calculate the quantum yield, as detailed in the primary method based on diffuse reflectance described by Liu *et al.*[44] Absorption and emission spectra for the determination of the relative quantum yield of the solutions ($\Phi_{solution}$) in toluene were obtained as detailed above. Coumarin-153 obtained from Exciton was dissolved in 95% ethanol from Pharmco-AAPER to form the reference solution. Quantum yield values for the solutions were calculated using the optically dilute method described by Demas and Crosby.[45] All solutions were created at 10^{-5} M concentration.

RESULTS

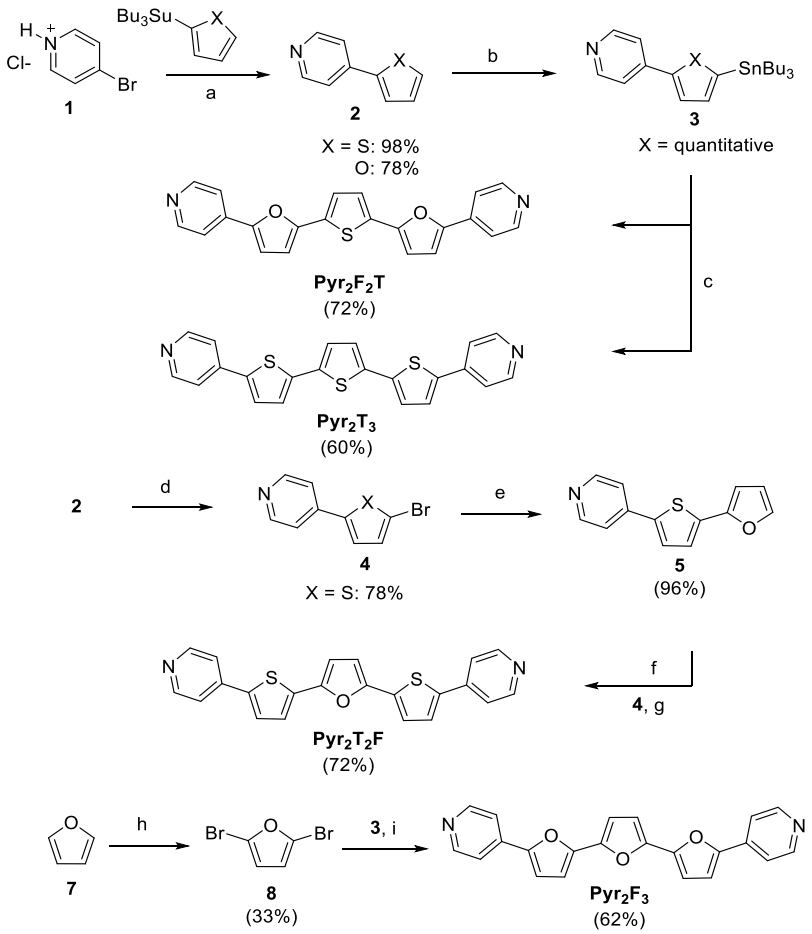

Scheme 1. a: TEA, $Pd(PPh_3)_4$, PhMe, reflux; **b**: *n*-BuLi, Bu_3SnCl, THF, –78 °C to room temperature (rt); **c**: 2,5-dibromothiophene, $Pd(PPh_3)_4$, PhMe/DMF, reflux; **d**: NBS, AcOH/$CHCl_3$, 60 °C; **e**: 2-tri-*n*-butylstannylfuran, $Pd(PPh_3)_4$, PhMe/DMF, reflux; **f**: *n*-BuLi, Bu_3SnCl, THF, –78 °C to rt; **g**: $Pd(PPh_3)_4$, PhMe/DMF, reflux; **h**: Br_2, DMF, rt; **i**: $Pd(PPh_3)_4$, PhMe/DMF, reflux

Synthesis. Preparation of the target oligomers primarily followed the literature reported syntheses of similar derivatives.[24, 28, 46] The syntheses were achieved as shown in Scheme 1. First, Stille coupling of bromopyridine (**1**) with either stannylated thiophene or furan afforded pyridyl thiophene and pyridyl furan in 98% and 78% yield, respectively. Stannylation of **2** generated **3** in quantitative yields for both the thiophene and furan starting material. Cross coupling of 2,5-dibromothiophene with two equivalents of **3** provided **Pyr2F2T** and **Pyr2T3** in 72% and 60% yield, respectively. On the other hand, treatment of **3** with 2,5-dibromofuran (**8**) produced **Pyr2F3** in

62% yield.[47] Seemingly, **Pyr$_2$T$_2$F** could be achieved from coupling **3** with **8** and was initially attempted; however, **8** was achieved in poor yield (33 %). Alternatively, the bromination of **2** (X = S) afforded **4** in 78% yield. Palladium-catalyzed coupling of **4** with stannylated furan yielded **5** in 96% yield, which was followed by stannylation of **5** and another cross-coupling reaction with **4** to afford **Pyr$_2$T$_2$F** in 72% yield. The structural integrity of each oligomer was confirmed by ^{1}H NMR, ^{13}C NMR, and high-resolution mass spectrometry (HRMS). A full synthetic description is included in the SI.

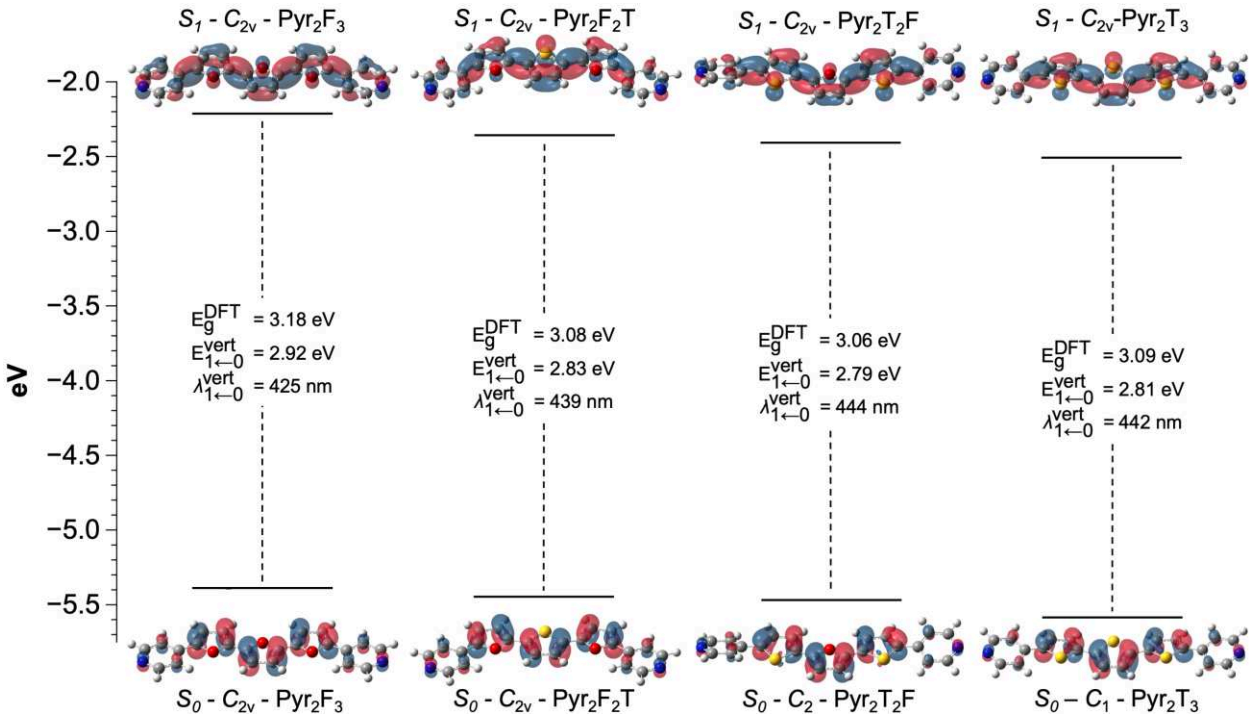

Figure 2. Ground state (S_0) HOMO-LUMO energy gaps (E_g^{DFT}), singlet excited state (S_1) vertical excitation energies ($E_{1\leftarrow0}^{vert}$), maximum wavelengths ($\lambda_{1\leftarrow0}^{vert}$), and molecular orbitals (HOMO for S_0 geometry and SOMO for S_1 geometry) projected onto the total electron density isosurface (0.036 a.u.) of each pyridyl-capped π-conjugated model oligomer at the B3LYP/6-311G(*2df,2pd*) level of theory. Enlarged S_0 and S_1 molecular orbitals are depicted in Figure S1 of the SI.

Computational. Optimized S_0 geometries and the point group symmetries of each oligomer at the B3LYP/6-311G(2*df*, 2*pd*) level of theory are depicted at the bottom of Figure 2, while the analogous TD-DFT results for S_1 are depicted at the top of Figure 2. It is important to note that the E_g^{DFT} values reported in Figure 2 serve as approximations to the fundamental energy gap, while the significantly smaller TD-DFT $E_{1\leftarrow 0}^{vert}$ values are more representative of the electronic transition.[48]

The pyridyl capped π-conjugated molecules studied here vary by the identity of their inner heterocyclic units. Only transoid and near-transoid (inter C=C–C=C torsional angle *ca*. 180°) structures are considered as it has been shown through torsional profiling that similar systems have lower electronic energies and are more thermodynamically stable than their cisoid (inter C=C-C=C angle *ca*. 0°) analogues.[5, 24, 49-50] As seen in Figure 2, all of the lowest lying optimized excited S_1 structures adopt planar transoid configurations with C_{2v} symmetry as do the optimized S_0 structures of **Pyr$_2$F$_3$** and **Pyr$_2$F$_2$T**, in which furan is bonded directly to pyridine. Conversely, the ground-state structures containing a thiophene subunit directly bonded to the pyridine moiety (*i.e.*, **Pyr$_2$T$_2$F** and **Pyr$_2$T$_3$**) exhibit minimum energy structures that are near-transoid with C_2 and C_1 symmetry, respectively. In the case of **Pyr$_2$T$_2$F**, the S_0 minimum energy structure deviates from planarity by *ca*. 19° as seen in the C=C-C=C torsional angle. This non-planar character occurs between the pyridine moieties and the nearest neighboring thiophene. The heteroatom-to-heteroatom torsional angles, between the central furan and the adjacent thiophenes, are nearly perfectly planar (179°). Although ground state structures of **Pyr$_2$T$_3$** also deviates from planarity, the heteroatom-to-heteroatom torsional angles between the central and neighboring thiophene breaks planarity by *ca*. 14°, while that between the pyridine moiety and the neighboring thiophene deviates from planarity by *ca.* 20°. Deviations in planarity have been attributed to repulsive interactions between the sulfur atom of a thiophene and either a pyridyl moiety (**Pyr$_2$T$_2$F**) or a pyridyl moiety

and an adjacent thiophene (**Pyr$_2$T$_3$**).[16,51-52] The S_0 results reported here are consistent with the minimum ground state energy structures of furan, thiophene, and alternating furan-thiophene oligomers previously reported in the literature.[24, 53]

Further insight into the geometrical and photophysical properties of the molecules was achieved by evaluating the frontier molecular orbitals of each oligomer. The excited-state form of the oligomers acquires a quinoid-like electronic configuration. The molecular orbitals for the four different oligomers are effectively comparable following an acceptor-donor-acceptor model in which electron density is localized primarily in the thiophene/furan chain for the HOMO and extends further along the carbon framework into the SOMO, or the singly occupied molecular orbital. The results from the DFT natural orbital analyses indicate that both the HOMO and SOMO are of π-nature supporting a π-π* electronic transition. In the C_{2v} and C_1 species, for example, these orbitals are solely composed of *p*-type atomic orbitals perpendicular to the molecular plane (Table S1). The HOMO exhibits π-bonding character about the C=C bonds in the five-membered rings and π-antibonding character about the C-C bonds between the five-membered rings. This character is reversed in the SOMO which also exhibits significant unhybridized *p*-orbital character on the oxygen and/or sulfur heteroatoms. Enlarged S_0 and S_1 molecular orbitals (Fig. S1) and computed absorption and emission spectra (Fig. S3) of **Pyr$_2$F$_3$**, **Pyr$_2$F$_2$T**, **Pyr$_2$T$_2$F**, and **Pyr$_2$T$_3$** can be found in the SI. Generally, the HOMO-LUMO energy gaps of furan-based oligomers are larger than those of thiophene systems.[16, 25] This trend is observed here where E_g^{DFT} exhibits an increase of 0.1 eV when going from **Pyr$_2$T$_3$** to **Pyr$_2$F$_3$**, which correlates well with the experimental observations that follow herein.

Cyclic voltammetry. Excellent optical and electrochemical properties are important characteristics of materials for organic device applications. Elaborating upon computational results, experimental analysis began with an investigation of electrochemical properties for each oligomer via cyclic voltammetry (Table 1, Fig. S4). All oxidations ($E_{(S+/S)}$) were observed as irreversible, even at fast scan rates of 1.0 V/s. **Pyr$_2$T$_2$F** (1.30 V), **Pyr$_2$F$_2$T** (1.22 V) and **Pyr$_2$F$_3$** (1.32 V) showed lower oxidation potentials than **Pyr$_2$T$_3$** (1.57 V), indicating higher HOMO levels for the furan containing oligomers.[54] Qualitatively, it is assumed that two close possible oxidation events were occurring for each substrate given the broadening of the oxidative waves. Although direct observation of these multiple oxidative waves was not apparent for (**Pyr$_2$F$_3$**), (**Pyr$_2$T$_2$F**) and (**Pyr$_2$T$_3$**), two peaks were distinctively seen for **Py$_2$F$_2$T** (Fig. S4).

Table 1. Electrochemical data in DMF.

	$E_{(S+/S)}$ onset (V)	$E_{(S+/S)}$ peak (V)	$E_{(S2+/S+)}$ peak (V)	$E_{(S/S-)}$ onset (V)	$E_{(S-/S2-)}$ peak (V)	HOMO (eV)	LUMO (eV)	E_g^{CV} (eV)
Pyr_2F_3	1.17	1.32	-	–1.64	–1.73	–5.57	–2.76	2.81
Pyr_2F_2T	1.06	1.22	1.37	–1.50	–1.66	–5.46	–2.90	2.56
Pyr_2T_2F	1.09	1.30	-	–1.44	–1.52	–5.49	–2.96	2.53
Pyr_2T_3	1.35	1.57	-	–1.33	–1.44	–5.75	–3.07	2.68

All reductions ($E_{(S/S-)}$) were observed to be reversible. In this case, the values (reported as the half-wave potential) indicate a clear trend that shows increasing the number of furans (*i.e.*, **Pyr$_2$F$_3$** > **Pyr$_2$F$_2$T** > **Pyr$_2$T$_2$F** > **Pyr$_2$T$_3$** in order of difficulty to reduce) leads to a shift toward more negative potentials versus NHE (*i.e.*, harder to reduce). This trend is followed by a second reduction event ($E_{(S-/S2-)}$), which is highlighted in Figure S4. Overall the observed experimental trends are consistent with those obtained from theoretical calculations, indicating that **Pyr$_2$F$_3$** (2.81 eV) possesses the largest HOMO-LUMO gap and the smallest value corresponds to **Pyr$_2$T$_2$F** (2.53

eV). A summary of the calculated electrochemical gaps (E_g^{CV}) obtained from CV are given in Table 1 for comparison to the calculated HOMO-LUMO gaps provided in Figure 2.

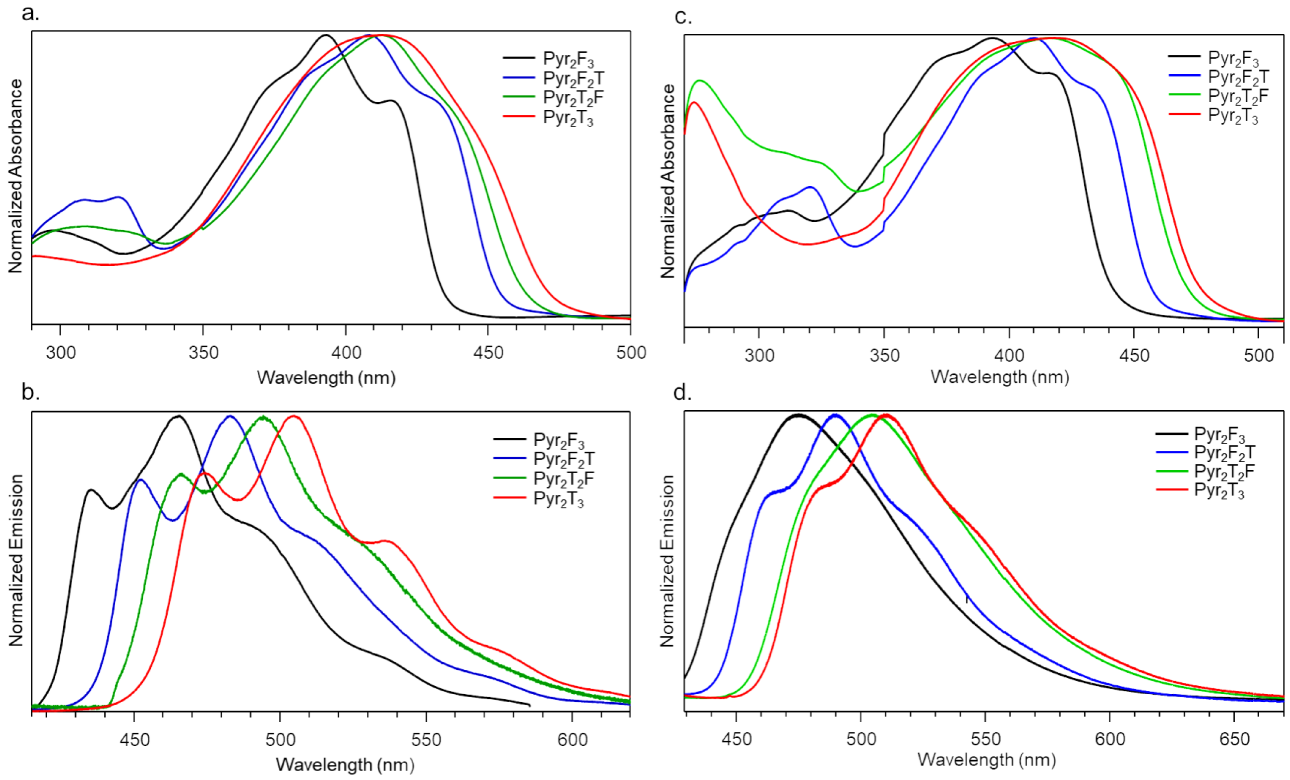

Figure 3. Solution phase spectra of the (a) absorption and (b) emission in toluene and the (c) absorption and (d) emission in DMF for **Pyr$_2$F$_3$** (black), **Pyr$_2$F$_2$T** (blue), **Pyr$_2$T$_2$F** (green), and **Pyr$_2$T$_3$** (red).

Spectroscopic. Supported by computational and electrochemical analysis, the optical behavior of the oligomers were studied. As summarized in Table 2 and shown in Figure 3, toluene solutions of each oligomer possess absorption profiles with λ_{max} = 393–413 nm and λ_{onset} = 465–504 nm. A minor difference in the absorption maximum of each molecule was observed when changing the solvent from toluene to DMF (λ_{max} = 393–418 nm and λ_{onset} = 475–510 nm), but their spectra are not significantly perturbed by solvent polarity.[55] The shift is modest (< 5 nm) for **Pyr$_2$F$_2$T**,

Pyr$_2$T$_2$F, and **Pyr$_2$T$_3$** and not observed for **Pyr$_2$F$_3$** as their spectra are not significantly perturbed by solvent polarity.[55] The experimental and computational results obtained for the absorbance are in agreement and can also be correlated to the corresponding maximum emission values.

Table 2. Maximum wavelengths associated with absorption (λ_{max}^{abs}) and emission (λ_{max}^{ems}), the Stokes shift between them, and the energetic gap of the optical transition (E_g^{opt}).

	λ_{max}^{abs} (nm)	λ_{max}^{ems} (nm)	Stokes shift (eV, [nm])	E_g^{opt} (eV, [nm])
	Solution – Toluene			
Pyr$_2$F$_3$	393	465	0.49 [72]	2.86 [434]
Pyr$_2$F$_2$T	408	483	0.47 [75]	2.74 [453]
Pyr$_2$T$_2$F	413	494	0.49 [81]	2.69 [460]
Pyr$_2$T$_3$	413	504	0.54 [91]	2.63 [472]
	Solution – DMF			
Pyr$_2$F$_3$	393	475	0.54 [82]	2.82 [440]
Pyr$_2$F$_2$T	410	489	0.49 [79]	2.69 [460]
Pyr$_2$T$_2$F	416	504	0.52 [88]	2.62 [473]
Pyr$_2$T$_3$	418	510	0.54 [92]	2.57 [482]
	Solid-state			
Pyr$_2$F$_3$	445	605	0.73 [159]	1.79 [692]
Pyr$_2$F$_2$T	473	598	0.55 [125]	2.12 [585]
Pyr$_2$T$_2$F	473	621	0.62 [148]	1.76 [705]
Pyr$_2$T$_3$	474	603	0.56 [129]	2.16 [573]

[a]Optical band gaps were calculated from the lowest energy onset and converted to eV.

The top panels of Figure 3 (a and c) show that each oligomer exhibits a broad absorption band ranging from *ca*. 350–470 nm with a weak vibronic shoulder that diminishes when increasing the number of thiophene subunits. These vibronic shoulders in the absorption spectra indicate the systems with greater numbers of furan subunits possess greater rigidity.[2] The bands at longer wavelength arise from π-π* electronic transitions of the conjugated systems and correspond to a transition from the ground singlet-state to the lowest excited singlet-state of each molecule.[56] The other lower intensity absorption peaks below 325 nm correspond to a transition to higher-lying singlet

states. This is supported by TD-DFT where electronic transitions corresponding to spectral features *ca.* 325 nm have oscillator strengths that are nearly an order of magnitude smaller ($f \leq 0.17$) than the lowest excited singlet-state of each molecule ($f \cong 1.5$). The onset absorption wavelengths as well as the absorption maxima of the π-π* transitions show a small but gradual red-shift with the addition of thiophene units in the order of **Pyr$_2$F$_3$**, **Pyr$_2$F$_2$T**, **Pyr$_2$T$_2$F**, and **Pyr$_2$T$_3$**. The trend in a shift to lower energy as the number of thiophene subunits present in the system increases is seen due to the increased degree of π-electron delocalization.[56]

As predicted computationally ($\lambda_{1\leftarrow 0}^{\text{vert}}$ in Figures 2, S1 and S3), increasing the number of thiophene subunits results in an experimental red-shifts in the absorption maxima (*i.e.*, 20-25 nm shift) when going from **Pyr$_2$F$_3$** to **Pyr$_2$T$_3$** (Table 2). Similarly, a decrease in the optical gap can be seen as the number of furan subunits in the system is reduced. These two trends are evident in the data contained in the last column of Table 2. Molar extinction coefficients were also calculated from the absorption spectra using the Beer-Lambert law. The homomeric congeners, **Pyr$_2$F$_3$** and **Pyr$_2$T$_3$**, possessed the greatest values for the molar extinction coefficient (ε): 2.9×10^4 M^{-1} cm^{-1} and 2.4×10^4 M^{-1} cm^{-1}, respectively. **Pyr$_2$T$_2$F** exhibited a decrease in ε (2.0×10^4 M^{-1} cm^{-1}) while **Pyr$_2$F$_2$T** exhibited the lowest value of the four oligomers (7.8×10^3 M^{-1} cm^{-1}).

Emission profiles are depicted in Figures 3b and 3d and the summary of these results is tabulated in Table 2. Effects of the oligomeric framework and thiophene/furan ratio are more pronounced in the fluorescence data. There is a noticeable increase in wavelength emission maxima with a decrease in furan rings (*ca.* 35–40 nm). Well-defined vibronic features are observed for emission spectra of the oligomers in toluene. The vibrational structure observed in the emission spectra for all four compounds are due to the rigid and planar nature of the excited state geometry

for the oligomers.[16] However, these spectral features are greatly diminished in DMF. This difference in emission data (toluene vs. DMF) is attributed to changes in vibrational energy levels due to solvent-solute interactions. More polar solvents tend to limit the appearance of vibrational fine structure by compressing vibrational energies within a given state.[55, 57]

Similar to the absorbance data, the shifts in emission maximum upon variation of solvent are marginal (*i.e.*, $\leq$ 10 nm), indicating that the optical properties of the oligomers are not significantly affected by solvent polarity. The observed Stokes-shifts point to, in some degree, the presence of intramolecular transfer of electron density from the furan/thiophene core to the pyridyl caps, particularly for **Pyr$_2$T$_2$F** and **Pyr$_2$T$_3$**.[58-59] In addition, the Stokes-shift (the energetic difference between the absorption and emission maximum) is higher for **Pyr$_2$T$_3$** (0.54 eV) when compared with **Pyr$_2$F$_3$** and **Pyr$_2$F$_2$T**, which indicates that the oligomers containing more furan units have more rigid backbones and less structural reorganization upon photoexcitation. Indeed, such has been observed in previous reports[2, 11, 13, 17] and is supported by theory as the first excited state geometry was found to be planar (Figs. 3 and S1).

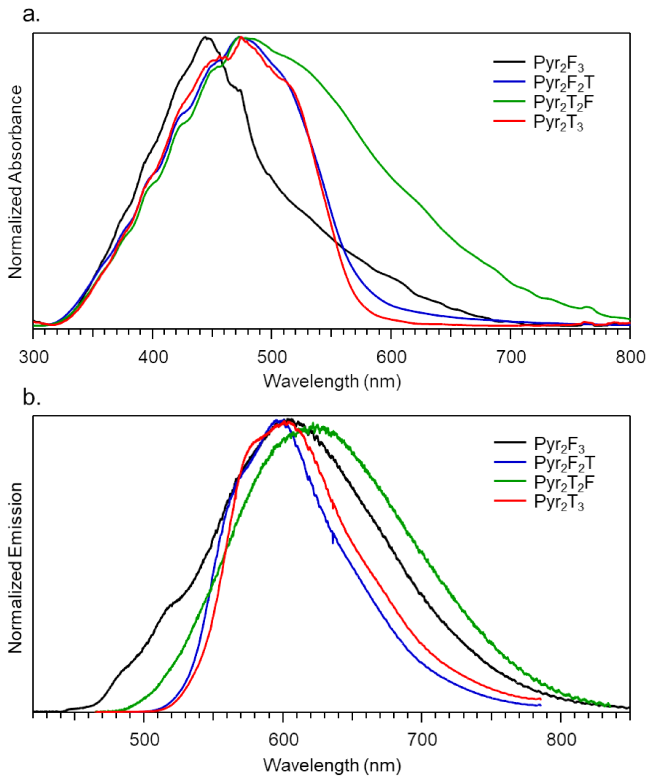

Figure 4. Solid-state (a) diffuse reflectance and (b) emission spectra of **Pyr$_2$F$_3$** (black), **Pyr$_2$F$_2$T** (blue), **Pyr$_2$T$_2$F** (green), and **Pyr$_2$T$_3$** (red).

Figure 4 shows the solid-state absorption and emission curves for the oligomers. Red-shifts ranging from 50 nm to 60 nm were observed for the π-π* transition absorption bands in the solid-state. The red-shifted absorption is indicative of molecules with a more coplanar conformation in the solid. This is significant for **Pyr$_2$T$_2$F**, which possesses a broadened spectrum when compared to the other oligomers considered here. Unlike that of the solution-phase spectra, there is no apparent trend in absorption or emission maxima. Interestingly, the oligomers exhibit relatively similar solid-state emission profiles but differ in absorption (*i.e.*, spectral features, especially for **PyrF$_3$**). Presumably, this is due to conformational variations and are rationalized via theory: the optimized excited S_1 structures for each oligomer is that of C_{2v} symmetry while the S_0 minimum

energy structures deviate consisting of C_{2v} (**Pyr$_2$F$_3$** and **Pyr$_2$F$_2$T**), C_2 (**Pyr$_2$T$_2$F**), and C_1 (**Pyr$_2$T$_3$**) symmetry. When comparing the spectral profiles for solution to that of solid-state, such is evident with deviations resulting from environment. An analysis of the Stokes-shift reveals that **Pyr$_2$F$_3$** possesses the largest shift of the four compounds (λ_{max} = 159 nm), while **Pyr$_2$F$_2$T** and **Pyr$_2$T$_3$** have the smallest shifts with nearly identical Stoke-shift values (λ_{max} = 125 nm and 129 nm, respectively). **Pyr$_2$T$_2$F** exhibits a Stokes-shift midway between the two with a maximum wavelength of 148 nm.

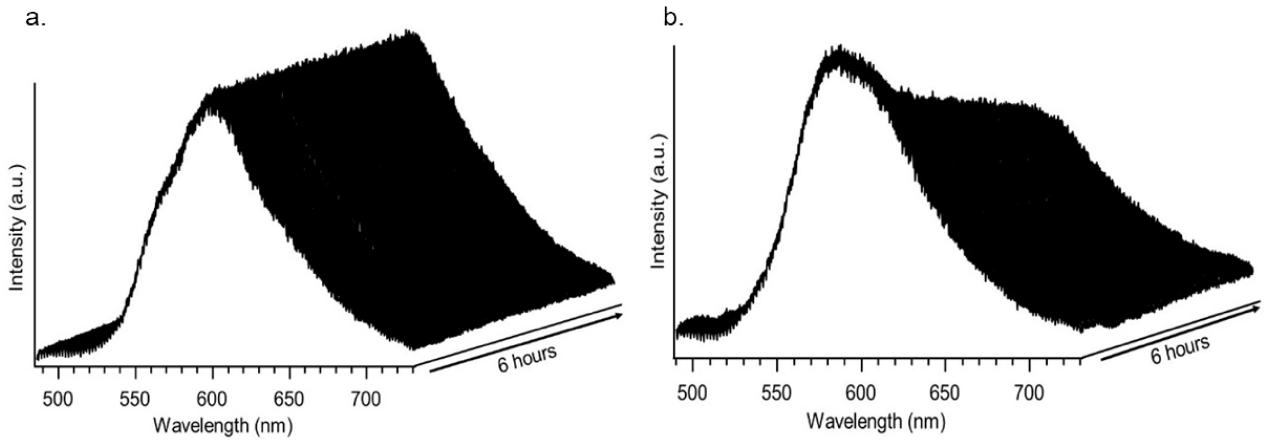

Figure 5. Photostability of solid-state (a) **Pyr$_2$F$_2$T** and (b) **Pyr$_2$T$_3$** and over 6 hours.

Figure 5 shows the solid-state photostability of **Pyr$_2$T$_3$** and **Pyr$_2$F$_2$T** with constant irradiation under ambient conditions. Due to the low incident power density required for these measurements (0.06mW/cm^2), **Pyr$_2$F$_3$** and **Pyr$_2$T$_2$F** did not have sufficient fluorescence emission for photostability analysis. **Pyr$_2$F$_2$T** was found to have a significantly higher photostability (98%) when compared to **Pyr$_2$T$_3$** (74%), possibly due to differences in packing in the solid state. Low, nearly

identical quantum yields were obtained for **Pyr$_2$F$_2$T** and **Pyr$_2$T$_3$**, with **Pyr$_2$F$_2$T** exhibiting the largest solid-state quantum yield of 5%. When estimating the solution quantum yield relative to Coumarin-153, a trend in increasing quantum yield is observed with increasing number of furan subunits. This trend can be attributed to a decrease in the heavy atom effect, which causes intersystem crossing and leads to lower fluorescent quantum yields.[42] Additionally, this trend is correlated with the observed Stokes shifts where more thiophene groups leads to larger Stokes shifts due to larger reorganizations. These reorganizations often diminish fluorescent quantum yields. Similar trends have been previously observed in other furan-thiophene containing systems.[29]

Table 3. Excited state lifetimes (τ), solid-state photostability, and quantum yields (Φ).

	Φ_{solid}	$\Phi_{solution}$	Photostability[a]	τ_{solid} (ns)	$\tau_{toluene}$ (ns)	τ_{DMF} (ns)
Pyr$_2$F$_3$	<1%	8%	--	τ_1=0.7 τ_2=3.1	1.5	1.8
Pyr$_2$F$_2$T	5%	7%	98%	1.1	0.8	0.9
Pyr$_2$T$_2$F	<1%	6%	--	τ_1=0.5 τ_2=1.9	1.2	1.1
Pyr$_2$T$_3$	3%	3%	74 %	0.9	0.6	0.6

[a]**Pyr$_2$F$_3$** and **Pyr$_2$T$_2$F** are not sufficiently emissive in the solid-state to allow for photostability analysis.

Excited state lifetimes of all four compounds in solution- and solid-state are included in Table 3 and Figures S5-7. Uncertainties in the fits of the exponential decay curves are included in Table S10. **Pyr$_2$F$_3$** and **Pyr$_2$T$_2$F** were found to have biexponential lifetimes in the solid state while **Pyr$_2$F$_2$T** and **Pyr$_2$T$_3$** both exhibited single exponential lifetimes. The biexponential lifetimes observed in the solid likely arise due to intermolecular interactions between neighboring molecules.

It is possible that the molecular density in the solid is greater for **Pyr$_2$F$_3$** and **Pyr$_2$T$_2$F**, as is seen when comparing oligofurans to their oligothiophenes counterparts, thus leading to stronger intermolecular interactions.[2] The lifetime in solution is expected to be longer than in the solid-state due to the decrease in intermolecular noncovalent interactions in solution; however, the opposite was seen for **Pyr$_2$F$_2$T** and **Pyr$_2$T$_3$**. These values obtained in toluene were compared to the lifetimes in DMF to see if this decrease in the solution-state lifetime relative to the solid-state lifetime for **Pyr$_2$F$_2$T** and **Pyr$_2$T$_3$** was a result of solvent interactions with the two compounds. The trend in shortening of the lifetimes for **Pyr$_2$F$_2$T** and **Pyr$_2$T$_3$** in solution compared to the solid remain consistent between toluene and DMF.

DISCUSSION

A noted goal of this work was to identify materials possessing both solution and solid-state properties that were comparable to, if not better than the ubiquitous thiophene. In designing these materials for optoelectronics and device fabrication, processability of the organic π-conjugated materials is necessary.[24] Oligofurans are noted to be more soluble than oligothiophenes, but the former compounds are less stable than the latter ones.[25, 60] This increased solubility of furan-containing systems compared to thiophene-containing systems is well documented.[42] We suggest that by developing alternating furan-thiophene oligomers, solubility will increase. Indeed, there is a noticeable improvement in solubility with the addition of furan subunits. For both electrochemical and photophysical experiments, sonication was needed for **Pyr$_2$T$_3$** and **Pyr$_2$T$_2$F**. In contrast, both **Pyr$_2$F$_2$T** and **Pyr$_2$F$_3$** were readily dissolved in both toluene and DMF at various concentrations, which demonstrates that they are soluble in both non-polar and polar solvents, facilitating solution-phase processing and straightforward characterizations.

Appropriate solvation afforded solution-state analysis of electrochemical properties which correlates well with results obtained from computational analysis. Oxidation potentials were shown to decrease with the addition of furan rings while reduction potentials became more negative (higher energy). This trend is common as furan-based molecules typically show irreversible oxidation and a tendency for the oxidation potential values to be lower energy than oligothiophenes of similar molecular framework.[61] We detected broad oxidation waves for **Pyr$_2$F$_3$**, **Pyr$_2$T$_2$F** and **Pyr$_2$T$_3$** and two separate peaks for **Py$_2$F$_2$T**. Observation of multiple irreversible peaks is distinctive for oligofurans and oligothiophenes and corresponds to oxidation processes in which possible side reactions occur.[28] Although, the formation of other products was not observed, such cannot be ruled out.

Solution-phase absorption and emission profiles for each oligomer show characteristic spectral features representative of furan and thiophene-based oligomers.[5,13,22,6g,12b,27] **Pyr$_2$T$_2$F** and **Pyr$_2$F$_2$T** oligomers exhibited absorption maxima and onset values quite close to that of the **Pyr$_2$T$_3$**. Consistent with theoretical calculations and electrochemical data, these results indicate that HOMO-LUMO gaps of **Pyr$_2$T$_2$F** and **Pyr$_2$F$_2$T** are analogous to that of **Pyr$_2$T$_3$** yet smaller than that of **Pyr$_2$F$_3$**. The absorption and emission maxima for the oligomers were nearly independent of solvent polarity. The lack of distinct changes in the absorption and emission maxima suggest that the polarity of the ground- and excited-states for each oligomer are similar.[62-63] Interestingly, the spectroscopic features—specifically, broadening in absorption and vibronically structured emission bands—differ with solvent polarity. Taking into account the Stokes-shift values and DFT calculation, the data supports the differing geometries of the ground- and excited states for each oligomer.

The observation that solution phase quantum yield increases with furan subunits is not unexpected. Surprising are results for oligomers possessing central furan units (**Pyr$_2$F$_3$** and **Pyr$_2$T$_2$F**). These oligomers showed a decrease in spectral feature resolution going from nonpolar to polar solvents and were nearly non-emissive in the solid-state. π-stacking is likely the dominant force between molecules in the solid-state, which could lead to the quenching observed in the solid-state emission of **Pyr$_2$F$_3$** and **Pyr$_2$T$_2$F** oligomers. As the strength and the number of inter-molecular π interactions decrease (*i.e.*, solid- vs solution-phase), quenching is limited, leading to non-zero quantum yields for all solution-phase oligomers. These intermolecular interactions are also likely the cause of the biexponential lifetimes observed for these two systems. The mixed oligomer with a central thiophene subunit (**Pyr$_2$F$_2$T**) possesses the greatest observed solid state quantum yield (5%) while also preserving strong emission in solution (7%); this system also exhibits the highest solid-state photostability (98% after 6 hours) of the oligomers investigated herein, making it attractive for use in device applications. These results suggest that the hybrid oligomer **Pyr$_2$F$_2$T** could serve as a viable competitor to homomeric thiophene-based optoelectronic building blocks.

CONCLUSIONS

Application-relevant semiconducting building blocks of heteromeric molecules (**Pyr$_2$F$_2$T** and **Pyr$_2$T$_2$F**) were successfully synthesized. Employing DFT calculations and cyclic voltammetry, systematic studies of the HOMO-LUMO energies, geometrical and photophysical properties were achieved and compared to experimental results. The DFT computations indicate that both the HOMO and LUMO are of π-nature supporting a π-π* electronic transition with the lowest energy excited-state TD-DFT structures for those identified as planar, with C_{2v} point group symmetries.

Solution-phase absorption and emission profiles for each oligomer show characteristic spectral features representative of furan and thiophene with broad absorption band ranging from *ca.* 350–470 nm and emission maxima ranging from *ca.* 475–575 nm. Solid-state absorption and emission curves for the oligomers were red-shifted by 50-60 nm relative to solution-phase data. Compared to their homomeric (**Pyr$_2$F$_3$** and **Pyr$_2$T$_3$**) congeners, hybrid oligomers displayed superior optoelectronic properties. Specifically, **Pyr$_2$F$_2$T** exhibited comparatively higher solution-state and solid-state quantum yields as well as greater photostability; in addition, this heteromeric compound was found to possess a smaller HOMO-LUMO gap than either homomeric system. In summary, the work provides an example of a promising building block for bottom-up approaches to organic semiconducting devices.

Conflicts of Interest

There are no conflicts to declare.

ASSOCIATED CONTENT

Supporting Information

Electronic Supplementary Information (ESI) available: details of the theoretical calculations, NMR spectra, and supplementary results. See DOI: 10.1039/x0xx00000x

AUTHOR INFORMATION

Corresponding Author

* E-mail: dwatkins@olemiss.edu

Present Addresses

†If an author's address is different than the one given in the affiliation line, this information may be included here.

Author Contributions

The manuscript was written through contributions of all authors. All authors have given approval to the final version of the manuscript. ‡These authors contributed equally.

Funding Sources

National Science Foundation OIA-1539035

National Science Foundation CHE-1652094

National Science Foundation CHE-1664998

Notes

Any additional relevant notes should be placed here.

ACKNOWLEDGMENT: S.T.N, S.B., I.C., and D.L.W. appreciate financial support of this work from the National Science Foundation CAREER Award under Grant Numbers CHE-1652094. A.E.S., J.H.D. and N.I.H. acknowledge support from the National Science Foundation Grant Number OIA-1539035. T.L.E. and G.S.T. acknowledge support from the National Science Foundation under Grant Number CHE-1664998 and the computational resources provided by the Mississippi Center for Supercomputing Research.

ABBREVIATIONS

Pyr, pyridine; T, thiophene; F, furan.

REFERENCES

1. Jeffries-El, M.; Kobilka, B. M.; Hale, B. J., Optimizing the Performance of Conjugated Polymers in Organic Photovoltaic Cells by Traversing Group 16. *Macromolecules* **2014,** *47* (21), 7253-7271.
2. Gidron, O.; Bendikov, M., α-Oligofurans: An Emerging Class of Conjugated Oligomers for Organic Electronics. *Angew. Chem. Int. Ed.* **2014,** *53* (10), 2546-2555.
3. Coropceanu, V.; Li, H.; Winget, P.; Zhu, L. Y.; Bredas, J. L., Electronic-Structure Theory of Organic Semiconductors: Charge-Transport Parameters and Metal/Organic Interfaces. In *Annual Review of Materials Research, Vol 43*, Clarke, D. R., Ed. 2013; Vol. 43, pp 63-87.
4. Zamoshchik, N.; Sheynin, Y.; Bendikov, M., Toward the rational design of conjugated oligomers and polymers: Systematic study of the substituent effect in oligothiophenes. *Isr. J. Chem.* **2014,** *54* (5-6), 723-735.
5. Gidron, O.; Diskin-Posner, Y.; Bendikov, M., α-Oligofurans. *J. Am. Chem. Soc.* **2010,** *132* (7), 2148-2150.
6. Rasmussen, S. C.; Evenson, S. J.; McCausland, C. B., Fluorescent thiophene-based materials and their outlook for emissive applications. *Chem. Commun.* **2015,** *51* (22), 4528-4543.
7. Tibaoui, T.; Ayachi, S.; Chemek, M.; Alimi, K., New bridged oligofuran for optoelectronic applications. *Spectrochim Acta A Mol Biomol Spectrosc* **2015,** *142*, 25-33.
8. Xiong, Y.; Wang, M.; Qiao, X.; Li, J.; Li, H., Syntheses and properties of π-conjugated oligomers containing furan-fused and thiophene-fused aromatic units. *Tetrahedron* **2015,** *71* (5), 852-856.
9. Walker, B.; Tamayo, A. B.; Dang, X.-D.; Zalar, P.; Seo, J. H.; Garcia, A.; Tantiwiwat, M.; Nguyen, T.-Q., Nanoscale Phase Separation and High Photovoltaic Efficiency in Solution-Processed, Small-Molecule Bulk Heterojunction Solar Cells. *Adv. Funct. Mater.* **2009,** *19* (19), 3063-3069.
10. Woo, C. H.; Beaujuge, P. M.; Holcombe, T. W.; Lee, O. P.; Fréchet, J. M. J., Incorporation of Furan into Low Band-Gap Polymers for Efficient Solar Cells. *J. Am. Chem. Soc.* **2010,** *132* (44), 15547-15549.
11. Gidron, O.; Dadvand, A.; Sheynin, Y.; Bendikov, M.; Perepichka, D. F., Towards "green" electronic materials. [small alpha]-Oligofurans as semiconductors. *Chem. Commun.* **2011,** *47* (7), 1976-1978.
12. Ferron, C. C.; Delgado, M. C. R.; Gidron, O.; Sharma, S.; Sheberla, D.; Sheynin, Y.; Bendikov, M.; Navarrete, J. T. L.; Hernandez, V., [small alpha]-Oligofurans show a sizeable extent of [small pi]-conjugation as probed by Raman spectroscopy. *Chem. Commun.* **2012,** *48* (53), 6732-6734.
13. Gidron, O.; Varsano, N.; Shimon, L. J. W.; Leitus, G.; Bendikov, M., Study of a bifuran vs. bithiophene unit for the rational design of [small pi]-conjugated systems. What have we learned? *Chem. Commun.* **2013,** *49* (56), 6256-6258.
14. Sheberla, D.; Patra, S.; Wijsboom, Y. H.; Sharma, S.; Sheynin, Y.; Haj-Yahia, A.-E.; Barak, A. H.; Gidron, O.; Bendikov, M., Conducting polyfurans by electropolymerization of oligofurans. *Chemical Science* **2015,** *6* (1), 360-371.
15. Huang, J.-D.; Wen, S.-H.; Deng, W.-Q.; Han, K.-L., Simulation of Hole Mobility in α-Oligofuran Crystals. *J. Phys. Chem. B* **2011,** *115* (10), 2140-2147.
16. Bunz, U. H. F., α-Oligofurans: Molecules without a Twist. *Angew. Chem. Int. Ed.* **2010,** *49* (30), 5037-5040.
17. Sharma, S.; Bendikov, M., α-oligofurans: A computational study. *Chem.: Eur. J* **2013,** *19* (39), 13127-13139.

18. Horner, K. E.; Karadakov, P. B., Chemical bonding and aromaticity in furan, pyrrole, and thiophene: A magnetic shielding study. *J. Org. Chem.* **2013,** *78* (16), 8037-8043.
19. Najmidin, K.; Kerim, A.; Abdirishit, P.; Kalam, H.; Tawar, T., A comparative study of the aromaticity of pyrrole, furan, thiophene, and their aza-derivatives. *J. Mol. Model.* **2013,** *19* (9), 3529-3535.
20. Shimizu, Y.; Azumi, T., Mechanism of external heavy atom effect on intersystem crossing in fluid solutions. Analysis based on fluorescence decay data. *J. Phys. Chem.* **1982,** *86* (1), 22-26.
21. Shetty, A. S.; Zhang, J.; Moore, J. S., Aromatic π-Stacking in Solution as Revealed through the Aggregation of Phenylacetylene Macrocycles. *J. Am. Chem. Soc.* **1996,** *118* (5), 1019-1027.
22. Kraft, A.; Grimsdale, A. C.; Holmes, A. B., Electroluminescent Conjugated Polymers—Seeing Polymers in a New Light. *Angew. Chem. Int. Ed.* **1998,** *37* (4), 402-428.
23. Yiu, A. T.; Beaujuge, P. M.; Lee, O. P.; Woo, C. H.; Toney, M. F.; Fréchet, J. M. J., Side-Chain Tunability of Furan-Containing Low-Band-Gap Polymers Provides Control of Structural Order in Efficient Solar Cells. *J. Am. Chem. Soc.* **2011,** *134* (4), 2180-2185.
24. Miyata, Y.; Nishinaga, T.; Komatsu, K., Synthesis and Structural, Electronic, and Optical Properties of Oligo(thienylfuran)s in Comparison with Oligothiophenes and Oligofurans. *J. Org. Chem.* **2005,** *70* (4), 1147-1153.
25. Cao, H.; Rupar Paul, A., Recent Advances in Conjugated Furans. *Chem.: Eur. J* **2017,** *23* (59), 14670-14675.
26. Henssler, J. T.; Matzger, A. J., Regiochemical Effects of Furan Substitution on the Electronic Properties and Solid-State Structure of Partial Fused-Ring Oligothiophenes. *J. Org. Chem.* **2012,** *77* (20), 9298-9303.
27. D'Andrade, B. W.; Datta, S.; Forrest, S. R.; Djurovich, P.; Polikarpov, E.; Thompson, M. E., Relationship between the ionization and oxidation potentials of molecular organic semiconductors. *Org. Electron.* **2005,** *6* (1), 11-20.
28. Hayoun Barak, A.; De Ruiter, G.; Lahav, M.; Sharma, S.; Gidron, O.; Evmenenko, G.; Dutta, P.; Bendikov, M.; Van Der Boom, M. E., Coordination-based molecular assemblies of oligofurans and oligothiophenes. *Chem.: Eur. J* **2013,** *19* (27), 8821-8831.
29. Seixas De Melo, J.; Elisei, F.; Becker, R. S., Photophysical studies of mixed furan, pyrrole, and thiophene-containing oligomers with three and five rings. *J. Chem. Phys.* **2002,** *117* (9), 4428-4435.
30. Becke, A. D., Density-functional thermochemistry. III. The role of exact exchange. *J. Chem. Phys.* **1993,** *98* (7), 5648-5652.
31. Miehlich, B.; Savin, A.; Stoll, H.; Preuss, H., Results obtained with the correlation energy density functionals of becke and Lee, Yang and Parr. *Chem. Phys. Lett.* **1989,** *157* (3), 200-206.
32. Lee, C.; Yang, W.; Parr, R. G., Development of the Colle-Salvetti correlation-energy formula into a functional of the electron density. *Physical Review B* **1988,** *37* (2), 785-789.
33. Krishnan, R.; Binkley, J. S.; Seeger, R.; Pople, J. A., Self-consistent molecular orbital methods. XX. A basis set for correlated wave functions. *J. Chem. Phys.* **1980,** *72* (1), 650-654.
34. McLean, A. D.; Chandler, G. S., Contracted Gaussian basis sets for molecular calculations. I. Second row atoms, Z=11–18. *J. Chem. Phys.* **1980,** *72* (10), 5639-5648.
35. Casida, M. E.; Jamorski, C.; Casida, K. C.; Salahub, D. R., Molecular excitation energies to high-lying bound states from time-dependent density-functional response theory: Characterization and correction of the time-dependent local density approximation ionization threshold. *J. Chem. Phys.* **1998,** *108* (11), 4439-4449.

36. Stratmann, R. E.; Scuseria, G. E.; Frisch, M. J., An efficient implementation of time-dependent density-functional theory for the calculation of excitation energies of large molecules. *J. Chem. Phys.* **1998,** *109* (19), 8218-8224.
37. Van Caillie, C.; Amos, R. D., Geometric derivatives of excitation energies using SCF and DFT. *Chem. Phys. Lett.* **1999,** *308* (3–4), 249-255.
38. Bauernschmitt, R.; Ahlrichs, R., Treatment of electronic excitations within the adiabatic approximation of time dependent density functional theory. *Chem. Phys. Lett.* **1996,** *256* (4–5), 454-464.
39. Laurent, A. D.; Jacquemin, D., TD-DFT benchmarks: A review. *Int. J. Quantum Chem* **2013,** *113* (17), 2019-2039.
40. Brémond, E.; Savarese, M.; Adamo, C.; Jacquemin, D., Accuracy of TD-DFT Geometries: A Fresh Look. *J. Chem. Theory Comput* **2018,** *14* (7), 3715-3727.
41. Bredas, J. L.; Silbey, R.; Boudreaux, D. S.; Chance, R. R., Chain-length dependence of electronic and electrochemical properties of conjugated systems: polyacetylene, polyphenylene, polythiophene, and polypyrrole. *J. Am. Chem. Soc.* **1983,** *105* (22), 6555-6559.
42. Tyson, G. E.; Tokmic, K.; Oian, C. S.; Rabinovich, D.; Valle, H. U.; Hollis, T. K.; Kelly, J. T.; Cuellar, K. A.; McNamara, L. E.; Hammer, N. I.; Webster, C. E.; Oliver, A. G.; Zhang, M., Synthesis, characterization, photophysical properties, and catalytic activity of an SCS bis(N-heterocyclic thione) (SCS-NHT) Pd pincer complex. *Dalton Transactions* **2015,** *44* (32), 14475-14482.
43. Zhang, Y.; Autry, S. A.; McNamara, L. E.; Nguyen, S. T.; Le, N.; Brogdon, P.; Watkins, D. L.; Hammer, N. I.; Delcamp, J. H., Near-Infrared Fluorescent Thienothiadiazole Dyes with Large Stokes Shifts and High Photostability. *J. Org. Chem.* **2017,** *82* (11), 5597-5606.
44. Liu, Y. S.; de Mayo, P.; Ware, W. R., Photophysics of polycyclic aromatic hydrocarbons adsorbed on silica gel surfaces. 3. Fluorescence quantum yields and radiative decay rate constants derived from lifetime distributions. *J. Phys. Chem.* **1993,** *97* (22), 5995-6001.
45. Crosby, G. A.; Demas, J. N., Measurement of photoluminescence quantum yields. Review. *J. Phys. Chem.* **1971,** *75* (8), 991-1024.
46. Hucke, A.; Cava, M. P., Synthesis of Mixed Thiophene/Furan Oligomers by Stille Coupling. *J. Org. Chem.* **1998,** *63* (21), 7413-7417.
47. Ramalingan, C.; Lee, I.-S.; Kwak, Y.-W., Novel Furanylarylene Arylsulfonylindolesulfonamides: Synthesis and Their Antibacterial Evaluation. *Chem. Pharm. Bull.* **2009,** *57* (6), 591-596.
48. Bredas, J.-L., Mind the gap! *Materials Horizons* **2014,** *1* (1), 17-19.
49. Bloom, J. W. G.; Wheeler, S. E., Benchmark Torsional Potentials of Building Blocks for Conjugated Materials: Bifuran, Bithiophene, and Biselenophene. *J. Chem. Theory Comput* **2014,** *10* (9), 3647-3655.
50. Fichou, D., Structural order in conjugated oligothiophenes and its implications on opto-electronic devices. *J. Mater. Chem.* **2000,** *10* (3), 571-588.
51. Zade, S. S.; Bendikov, M., Twisting of Conjugated Oligomers and Polymers: Case Study of Oligo- and Polythiophene. *Chem.: Eur. J* **2007,** *13* (13), 3688-3700.
52. Vujanovich, E. C.; Bloom, J. W. G.; Wheeler, S. E., Impact of Neighboring Chains on Torsional Defects in Oligothiophenes. *J. Phys. Chem. A* **2012,** *116* (11), 2997-3003.
53. Hayoun Barak, A.; de Ruiter, G.; Lahav, M.; Sharma, S.; Gidron, O.; Evmenenko, G.; Dutta, P.; Bendikov, M.; van der Boom, M. E., Coordination-Based Molecular Assemblies of Oligofurans and Oligothiophenes. *Chem.: Eur. J* **2013,** *19* (27), 8821-8831.

54. Kumagai, A.; Fukumoto, H.; Yamamoto, T., Chemical and Electrochemical Oxidation of Thiophene−Pyridine and Thiophene−Pyrimidine Co-Oligomers in Solutions. *J. Phys. Chem. B* **2007,** *111* (28), 8020-8026.
55. Robinson, J. W. F., Eileen S.; Frame, George M., II, *Undergraduate Instrumental Analysis*. 7th ed.; CRC Press: 2014.
56. Seixas de Melo, J.; Elisei, F.; Gartner, C.; Aloisi, G. G.; Becker, R. S., Comprehensive Investigation of the Photophysical Behavior of Oligopolyfurans. *J. Phys. Chem. A* **2000,** *104* (30), 6907-6911.
57. *Advances in Multi-Photon Processes and Spectroscopy*. WORLD SCIENTIFIC: 2008; Vol. Volume 18, p 304.
58. Liu, X.; Cole, J. M.; Xu, Z., Substantial intramolecular charge transfer induces long emission wavelengths and mega Stokes shifts in 6-aminocoumarins. *The Journal of Physical Chemistry C* **2017,** *121* (24), 13274-13279.
59. Haberhauer, G.; Gleiter, R.; Burkhart, C., Planarized Intramolecular Charge Transfer: A Concept for Fluorophores with both Large Stokes Shifts and High Fluorescence Quantum Yields. *Chem.: Eur. J* **2016,** *22* (3), 971-978.
60. Politis, J. K.; Nemes, J. C., Synthesis and Characterization of Regiorandom and Regioregular Poly(3-octylfuran). *J. Am. Chem. Soc.* **2001,** *123* (11), 2537-2547.
61. Distefano, G.; Jones, D.; Guerra, M.; Favaretto, L.; Modelli, A.; Mengoli, G., Determination of the electronic structure of oligofurans and extrapolation to polyfuran. *J. Phys. Chem.* **1991,** *95* (24), 9746-9753.
62. Pina, J.; de Melo, J. S.; Breusov, D.; Scherf, U., Donor–acceptor–donor thienyl/bithienyl-benzothiadiazole/quinoxaline model oligomers: experimental and theoretical studies. *Phys. Chem. Chem. Phys.* **2013,** *15* (36), 15204-15213.
63. Homocianu; Airinei, A.; Dorohoi, D., *Solvent effects on the electronic absorption and fluorescence spectra*. 2011; Vol. 2(1), p 011105.

TABLE OF CONTENTS IMAGE:

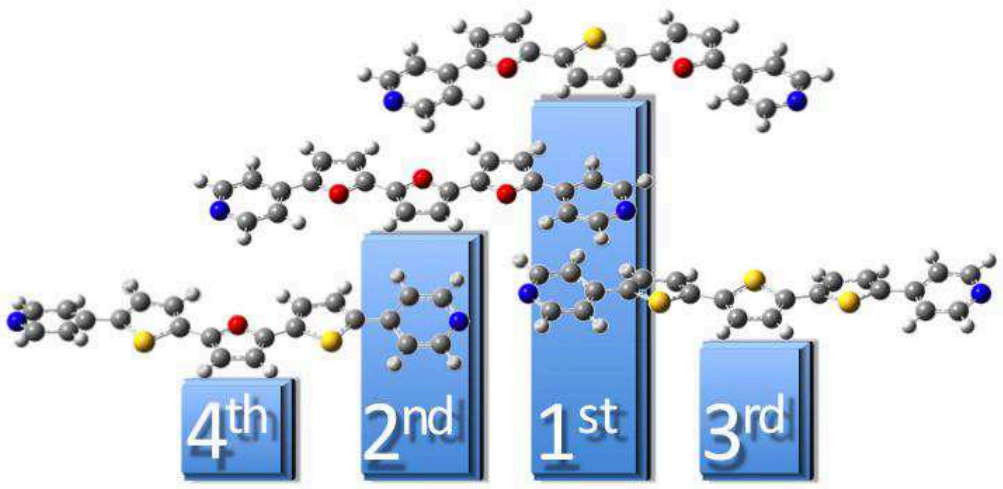

Combining furan and thiophene building blocks together creates new oligomers with enhanced properties.

SUPPORTING INFORMATION

Characterization of Furan- and Thiophene-containing Bispyridyl Oligomers via Spectroscopic, Electrochemical, and TD-DFT Methods

April E. Steen,[‡] Thomas L. Ellington,[‡] Suong T. Nguyen,[‡] Sivaraman Balasubramaniam, Indika Chandrasiri, Jared H. Delcamp, Gregory S. Tschumper, Nathan I. Hammer, and Davita L. Watkins

[†]Department of Chemistry, P.O Box 1848, University of Mississippi, University, Mississippi 38677, United States

*To whom correspondence should be addressed: dwatkins@olemiss.edu

Table of Contents Pages

General Information

All reactants (Fisher Scientific, Pittsburgh, PA, USA) and deuterated solvents (99.9 atom% D, Sigma-Aldrich, St. Louis, MO, USA) were purchased and used as received. THF and DMF were degassed in 20 L drums and passed through two sequential purification columns (activated alumina; molecular sieves for DMF) under a positive argon atmosphere. All synthetic procedures were carried out under argon atmosphere using standard schlenk line techniques unless otherwise stated. Thin layer chromatography (TLC) was performed on SiO_2-60 F_{254} aluminum plates with visualization by UV light. Flash column chromatography was performed using Silica gel technical grade, pore size 60 Å, 230−400 mesh particle size, 40−63 μm particle size from Sigma-Aldrich. ^1H (^{13}C) NMR were recorded on Mercury 300 or INOVA 500 spectrometer. Chemical shifts (δ) are given in parts per million (ppm) relative to TMS and referenced to residual protonated solvent purchased from Cambridge Isotope Laboratories, Inc. ($CDCl_3$: δH 7.26 ppm, δC 77.16 ppm; DMSO-d_6: δH 2.50 ppm, δC 39.52 ppm). Abbreviations used are s (singlet), d (doublet), t (triplet), q (quartet), quin (quintet), hp (heptet), b (broad), and m (multiplet). Electrospray ionization (ESI) high resolution mass spectra (HRMS) were recorded on an Agilent 6210 TOF spectrometer with MassHunter software.

All coupling reactions were carried out under constant degassing using nitrogen gas i.e. purging nitrogen through solution.

Synthetic Details

Reported below are the full synthetic details for the preparation of **Pyr_2T_3, Pyr_2T_2F, Pyr_2F_2T,** and **Pyr_2F_3**.[1-3]

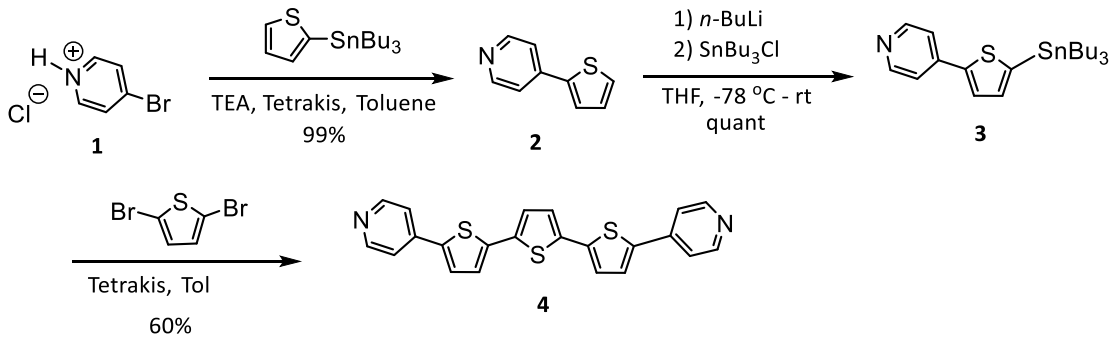

Scheme S1. Synthesis of **Pyr_2T_3** (**4**).

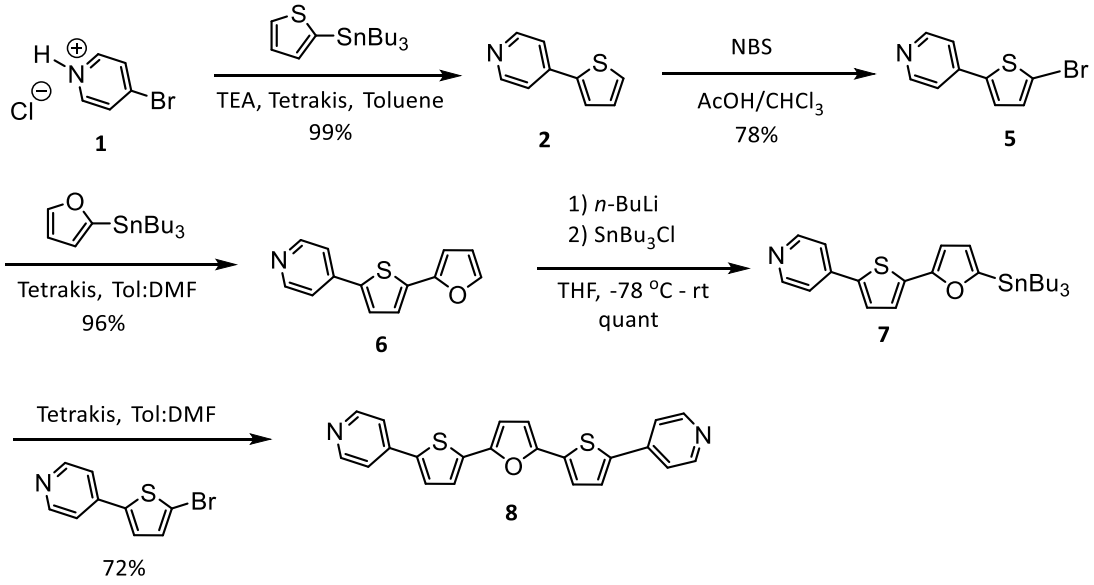

Scheme S2. Synthesis of **Pyr_2T_2F (8)**.

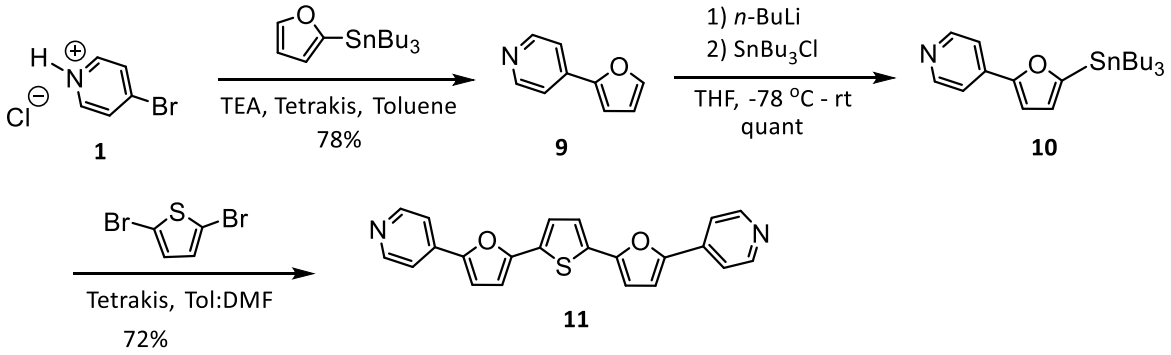

Scheme S3. Synthesis of **Pyr_2F_2T (11)**.

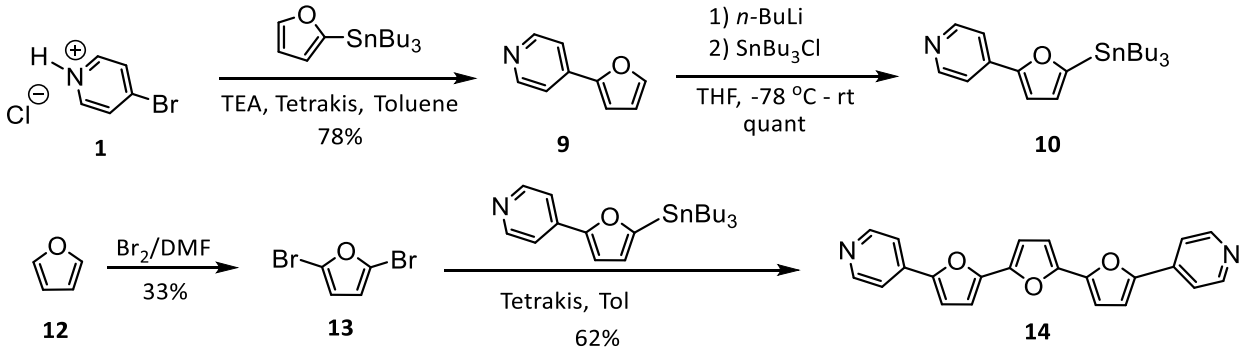

Scheme S4. Synthesis of **Pyr_2F_3 (14)**.

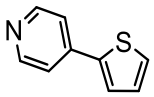

4-(Thiophen-2-yl)pyridine (2). To a degassed mixture of 4-bromopyridine hydrochloride (6.00 g, 30.85 mmol) in dry toluene (150 mL) and triethylamine (4.3 mL, 30.85 mmol) mixture, $[Pd(PPh_3)]_4$ (3.57 g, 3.09 mmol) was added and stirred at room temperature for 30 min under constant degassing. To this reaction mixture, 2-tri-*n*-butylstannylthiophene (10.75 mL, 33.94 mmol) was added and the resulting solution was stirred at room temperature for another 30 min under constant degassing. The reaction mixture was heated to reflux for 30 h. After being cooled to room temperature, the mixture was filtered through celite. The organic layer was evaporated and the crude product was purified by flash column chromatography (3% triethylamine in hexanes/ethyl acetate, 1:1). The pure product was obtained as white solid in 99% yields (4.95 g): ^{1}H NMR ($CDCl_3$, 300 MHz) δ 8.59 (d, 2H), 7.51 (d,1H), 7.48 (d, 2H), 7.42 (d, 1H), 7.14 (m, 1H). The ^{1}H NMR data matches that found in the literature.[4]

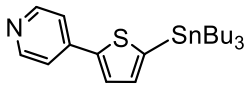

4-(5-(Tributylstannyl)thiophen-2-yl)pyridine (3). To a stirred solution of 4-(thiophen-2-yl)pyridine **(2)** (725 mg, 4.5 mmol) in dry THF (23 mL), *n*-butyllithium in hexane (2.5 M, 2.34 mL, 5.85 mmol) was added dropwise at -78 °C. The reaction mixture was stirred at this temperature for 30 min before being added tributyltin chloride (1.34 mL, 4.95 mmol) in dropwise fashion. The resulting mixture was allowed to attain room temperature and stirred for 12 h. The reaction was quenched with saturated ammonium chloride solution and the product was extracted twice with ethyl acetate. The organic layers were combined, washed with water followed by brine solution, dried over $MgSO_4$, and concentrated under reduced pressure. The product was obtained as red brown oil in 100% yields (2.03 g) without any purification: ^{1}H NMR ($CDCl_3$, 500 MHz) δ 8.57 (d, 2H), 7.60 (d, 1H), 7.48 (dd, 2H), 7.19 (d, 1H), 1.58 (t, 6H), 1.36 (m, 6H), 1.14 (t, 6H), 0.80 (t, 9H). The ^{1}H NMR data matches that found in the literature. [5]

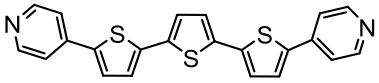

5,5''-Di(pyridin-4-yl)-2,2':5',2''-terthiophene (4). To a degassed mixture of 2,5-Dibromothiophene (250 µL, 2.25 mmol) in dry toluene (22 mL), $[Pd(PPh_3)]_4$ (520 mg, 0.45 mmol) was added under constant degassing and stirred for 30 min. To this 4-(5-(tributylstannyl)thiophen-2-yl)pyridine **(3)** (2.03 g, 4.5 mmol) was added and the resulting solution was degassed for additional 30 min before being heated to reflux for 24 h. During the cooling process, solid started precipitating from the reaction mixture. The reaction mixture was filtered and washed with ethyl acetate (25 ml). The crude product was then dissolved in acetone and filtered to remove black particles. Acetone was evaporated to obtain the pure product as yellow orange solid in 60 % yields (1.08 g) ^{1}H NMR ($CDCl_3$, 500 MHz) δ 8.61 (d, 4H), 7.46 (m, 6H), 7.22 (s, 2H), 7.19 (s, 2H). 13C NMR (126 MHz, CDCl3) δ 150.48, 150.45, 140.86, 140.79, 139.94, 138.57, 136.30, 126.26, 125.42, 125.16, 124.98, 119.53, 119.47. The ^{1}H and ^{13}C NMR data matches that found in the literature.

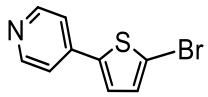

4-(5-Bromothiophen-2-yl)pyridine (5). To a degassed mixture of 4-(thiophen-2-yl)pyridine **(2)** in chloroform (30 mL) and glacial acetic acid (30 mL), *N*-bromosuccinimide (0.85 g, 4.80 mmol) was added slowly at room temperature. The resulting mixture was heated to reflux for 1.5 h to 3.0 h, until the solution turned into purple color. The reaction progress was monitored by 1H-NMR. Upon completion, the reaction mixture was poured into ice bath containing excess sodium bicarbonate to neutralize the acid, the layers were separated and organic layer was washed with water, brine solution, dried over $MgSO_4$, and evaporated to dryness. The product was obtained as brown solid in 78% yields (0.8189 g) without any purification: ^{1}H NMR ($CDCl_3$, 300 MHz) δ 8.60 (dd, 2H), 7.38 (dd, 2H), 7.25 (d, 1H), 7.10 (d, 1H). The ^{1}H data matches that found in the literature. [6]

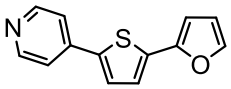

4-(5-(Furan-2-yl)thiophen-2-yl)pyridine (6). To a degassed mixture of 4-(5-bromothiophen-2-yl)pyridine **(5)** (2.30 g, 9.58 mmol) in dry toluene (40 mL) and dry *N,N*-dimethylformamide (40 mL), $[Pd(PPh_3)]_4$ (1.11 g, 0.96 mmol) was added and stirred at constant degassing for 30 min at room temperature. To the reaction mixture, 2-tri-*n*-butylstannylthiophene (3.92 mL, 12.45 mmol) was added and the resulting solution was degassed for additional 30 min before being heated to reflux for 30 h. After being cooled to room temperature, the reaction mixture was quenched using saturated sodium bicarbonate solution. Ethyl acetate was added and layers were separated. The organic layer was washed with water, dried over $MgSO_4$, and concentrated under reduced pressure. The crude product was purified by flash column chromatography (3% triethylamine in hexanes/ethyl acetate, 1:1). The pure product was obtained as light yellow solid in 96% yields (2.11 g): ^{1}H NMR ($CDCl_3$, 300 MHz) δ 8.59 (d, 2H), 7.47 (d, 1H), 7.46 (d, 2H), 7.44 (d, 1H), 7.27 (s, 1H), 6.60 (d, 1H) , 6.49 (t, 1H); ^{13}C NMR ($CDCl_3$, 126 MHz) δ 150.55, 148.92, 142.43, 141.21, 139.44, 135.46, 126.16, 123.66, 119.59, 112.10, 106.35. The ^{1}H and ^{13}C data match that found in the literature.[7]

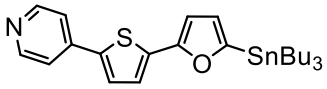

4-(5-(5-(Tributylstannyl)furan-2-yl)thiophen-2-yl)pyridine (7). To a stirred solution of 4-(5-(furan-2-yl)thiophen-2-yl)pyridine **(6)** (480 mg, 2.11 mmol) in dry THF (12 mL), *n*-butyllithium in hexane (2.5 M, 1.09 mL, 2. 74 mmol) was added dropwise at -78 ºC. The mixture was stirred at this temperature for 30 min. Tributyltin chloride (630 µL, 2.32 mmol) was added drop by drop at this temperature and stirred for 1 h. The reaction mixture was slowly brought to room temperature and stirred for 12 h. The reaction mixture was quenched with saturated ammonium chloride solution and the product was extracted twice with ethyl acetate. The organic layers were combined, washed with water, brine solution and dried over $MgSO_4$, and concentrated under reduced pressure. The product was obtained as red brown oil in 100% yields (1.23 g) without any purification: ^{1}H NMR ($CDCl_3$, 300 MHz) δ 8.58 (d, 2H), 7.46 (d, 2H), 7.44 (d, 1H), 7.22 (d, 1H), 6.61 (s, 2H), 1.60 (m, 6H), 1.37 (m, 6H), 1.13 (t, 6H), 0.92 (t, 9H)

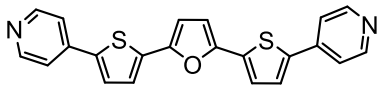

2,5-Bis(5-(pyridin-4-yl)thiophen-2-yl)furan (8). To a degassed mixture of 4-(5-bromothiophen-2-yl)pyridine **(5)** (486 mg, 2.0 mmol) in dry toluene (10 mL) and *N,N*-dimethylformamide (10 mL), $[Pd(PPh_3)]_4$ (232 mg, 0.2 mmol) was added and stirred at room temperature for 30 min under constant degassing. To this, 4-(5-(5-(tributylstannyl)furan-2-yl)thiophen-2-yl)pyridine **(7)** (1 g, 2.0 mmol) was added and stirred at room temperature for another 30 min under constant degassing before being heated to reflux for 12 h. After being cooled to room temperature, the reaction mixture was evaporated under reduced pressure. The crude product was purified via flash column chromatography (3% triethylamine in chloroform/methanol, 9:1) to obtain pure product as orange solid in 72% yields (550 mg): ^{1}H NMR ($CDCl_3$, 300 MHz) δ 8.61 (d, 4H) , 7.48 (d, 6H), 7.34 (d, 2H), 6.68 (d, 2H); ^{13}C NMR ($CDCl_3$, 126 MHz) δ 150.58, 148.57, 141.07, 139.91, 134.67, 126.30, 124.09, 119.58, 108.73; HRMS (ESI-TOF) calculated 386.4870 for $C_{22}H_{14}N_2OS_2$ $(M+H)^+$, found 387.0619.

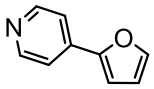

4-(furan-2-yl)pyridine (9): To a degassed mixture of 4-bromopyridine hydrochloride (3.00 g, 30.85 mmol) in toluene (75 mL) and triethylamine (2.15 mL, 30.85 mmol, $[Pd(PPh_3)]_4$ (1.8 g, 3.09 mmol) was added and stirred at constant degassing for 30 min at room temperature. To this, 2-tri-*n*-butylstannylfuran (5.4 mL, 33.94 mmol) was added and the resulting solution was degassed for additional 30 min before being heated to reflux for 30 h. The reaction mixture was cooled to room temperature, the mixture was filtered through celite. The crude product was purified by flash column chromatography (3% triethylamine in hexanes/ethyl acetate, 1:1). The pure product was obtained as white solid in 78% yields (2.3 g): ^{1}H NMR ($CDCl_3$, 300 MHz) δ 8.59 (d, 2H), 7.51 (d,1H), 7.48 (d, 2H), 7.42 (d, 1H), 7.14 (t or dd, 1H). The ^{1}H NMR data matches that found in the literature.[4]

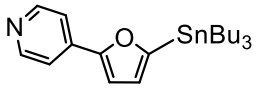

4-(5-(Tributylstannyl)furan-2-yl)pyridine (10). To a stirred solution of 4-(furan-2-yl)pyridine **(9)** (142 mg, 0.98 mmol) in dry THF (5 mL), *n*-butyllithium in hexane (2.5 M, 520 µL, 1.27 mmol) was added dropwise at -78 °C. The mixture was stirred at this temperature for 30 min before being added tributyltin chloride (291 µL, 1.07 mmol) in dropwise fashion. The resulting mixture was allowed to attain room temperature and stirred for 12 h. The reaction was quenched with saturated ammonium chloride solution and the product was extracted twice with ethyl acetate. The organic layers were combined, washed with water followed by brine solution, dried over $MgSO_4$, and concentrated under reduced pressure. The product was obtained as red brown oil in 100% yields (500 mg) without any purification: ^{1}H NMR ($CDCl_3$, 300 MHz) δ 8.58 (d, 2H), 7.50 (d, 2H), 6.89 (d, 1H), 6.66 (d, 1H), 1.61 (m, 6H), 1.35 (m, 6H), 1.13 (t, 6H), 0.91 (t, 9H). The ^{1}H data matches that found in the literature. [5]

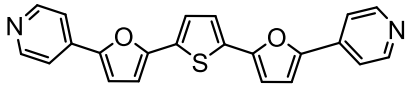

2,5-Bis(5-(pyridin-4-yl)furan-2-yl)thiophene (11). To a degassed mixture of 2,5-Dibromothiophene (368 µL, 3.11 mmol) in dry toluene (30 mL) and *N,N*-dimethylformamide (30 mL), $[Pd(PPh_3)]_4$ (718 mg, 0.62 mmol) was added and stirred at constant degassing for 30 min at room temperature. To this, 4-(5-(tributylstannyl)furan-2-yl)pyridine **(10)** (2.03 g, 4.5 mmol) was added and the resulting solution was degassed for additional 30 min before being heated to reflux for 12 h. After being cooled to room temperature, the reaction mixture was concentrated under reduced pressure. The crude product was purified by flash column chromatography (3% triethylamine in chloroform/methanol, 9:1) to obtain the pure product as orange solid in 72% yields (696 mg): 1H NMR ($CDCl_3$, 300 MHz) δ 8.63 (d, 4H), 7.57 (d, 4H), 7.34 (s, 2H), 6.97 (d, 2H), 6.69 (d, 2H); ^{13}C NMR ($CDCl_3$, 126 MHz) δ 150.61, 150.46, 150.29, 136.92, 132.41, 124.31, 117.65, 111.25, 108.13. ; HRMS (ESI-TOF) calculated 370.4260 for $C_{22}H_{14}N_2O_2S$ $(M+H)^+$, found 371.0849.

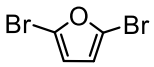

2,5-Dibromofuran (13). To a solution of furan (3.20 mL, 44 mmol) in dry *N,N*-dimethylformamide (45 mL) at 15-20 °C was added bromine (4.51 mL, 88 mmol) cautiously in a dropwise fashion. After the addition was completed, the resulting solution was stirred for 12h. The reaction was quenched by careful addition of saturated sodium bicarbonate solution at 0 °C. The product was extracted twice with ethyl acetate. The organic layers were combined, washed with water, dried over $MgSO_4$ and concentrated under reduced pressure. The crude product was purified via vacuum distillation and was obtained as brown oil in 33% yields (3.25 g): ^1H NMR ($CDCl_3$, 500 MHz) δ 6.31 (s, 2H); ^{13}C NMR (126 MHz, $CDCl_3$) δ 121.57, 114.10. The ^1H and ^{13}C data match that found in the literature.[2]

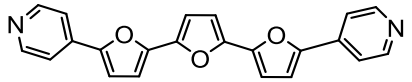

5,5''-Di(pyridin-4-yl)-2,2':5',2''-terfuran (14). To a degassed solution of 2,5-Dibromofuran (280 µL, 2.80 mmol) in dry toluene (40 mL), $[Pd(PPh_3)]_4$ (520 mg, 0.24 mmol) was added and stirred at constant degassing for 30 min at room temperature. To this 4-(5-(tributylstannyl)furan-2-yl)pyridine **(10)** (2.43 g, 5.60 mmol) was added and the resulting solution was degassed for additional 30 min before being heated to reflux for 24 h. During the cooling process, solid started precipitating from the reaction mixture. The reaction mixture was filtered and washed with ethyl acetate (50 ml). The crude solid was then dissolved in acetone and filtered to remove black particles. Acetone was evaporated to obtain pure product as yellow orange solid in 62% yields (1.22 g): ^1H NMR ($CDCl_3$, 500 MHz) δ 8.64 (d, 4H), 7.58 (d, 4H), 7.00 (d, 2H), 6.83 (s, 2H), 6.80 (d, 2H); ^{13}C NMR ($CDCl_3$, 126 MHz) δ 150.85, 150.41, 147.15, 145.79, 136.95, 117.70, 110.94, 108.60, 108.32. The ^1H and ^{13}C data match that found in the literature.[3]

Structure Refinement and Computational Details

All ground state (S_0) and excited state (S_1) computations were performed using a pruned numerical integration grid composed of 175 radial shells (250 radial shells for sulfur atoms) and 974 angular points per shell along with a threshold of $< 10^{-9}$ for the RMS change in the density matrix during the self-consistent field procedure. The threshold for removing linear dependent basis functions (magnitude of the eigen values of the overlap matrix) was tightened from 10^{-6} to 10^{-7}. All electronic energies have been converged to least 10^{-9} E_h while the Cartesian forces of the gradient did not exceed 10^{-5} E_h $Bohr^{-1}$for all geometry optimizations. Pure angular momentum basis functions (i.e., 5*d*, 7*f*, etc.) were used instead of their Cartesian counterparts (i.e., 6*d*, 10*f*, etc.). All molecular orbital figures were constructed via projection onto a total electron density isosurface (0.035 a.u.) at the B3LYP/6-311G(2*df*,2*pd*) (for S_0) and TD-B3LYP/6-311G(2*df*,2*pd*) (for S_1) levels of theory.

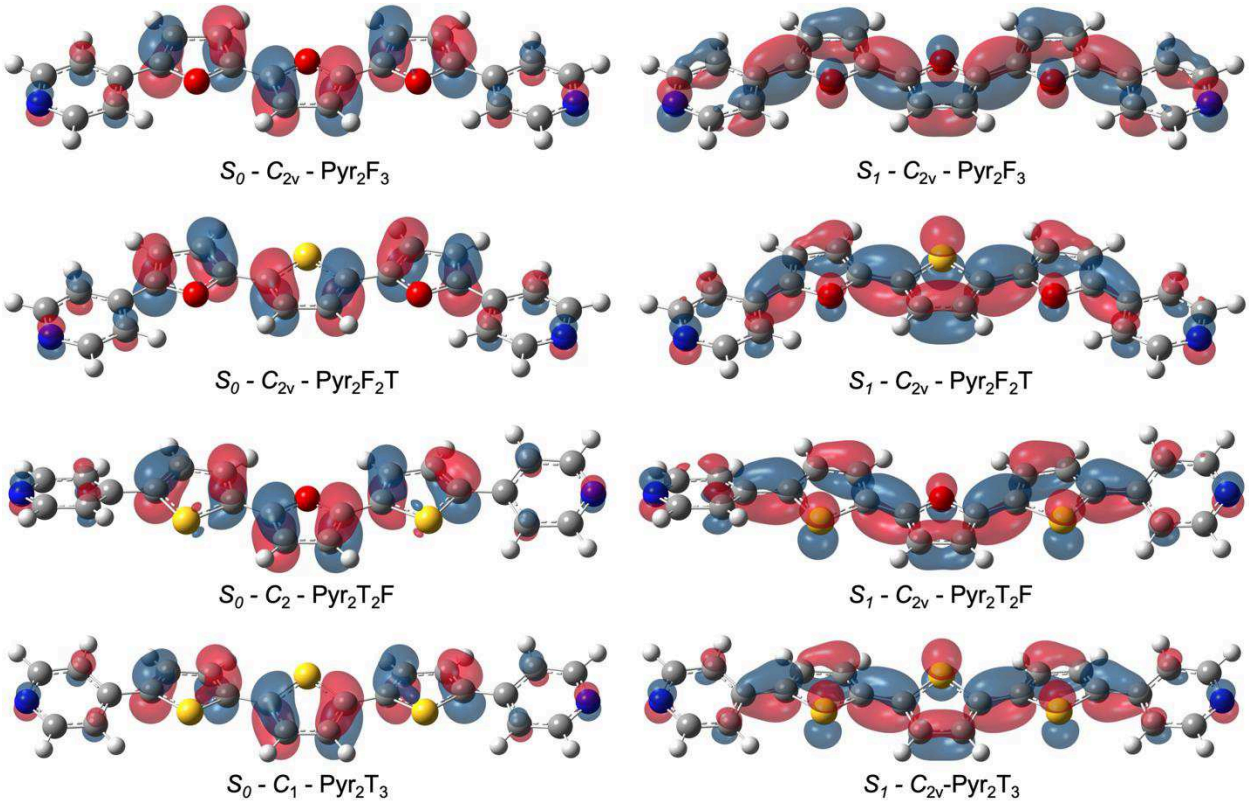

Figure S1. Ground state (S_0) and excited state (S_1) Molecular orbitals (HOMO for S_0 geometry and SOMO for S_1 geometry) projected onto a total electron density isosurface (0.035 a.u.) at the B3LYP/6-311G(2*df*,2*pd*) level of theory.

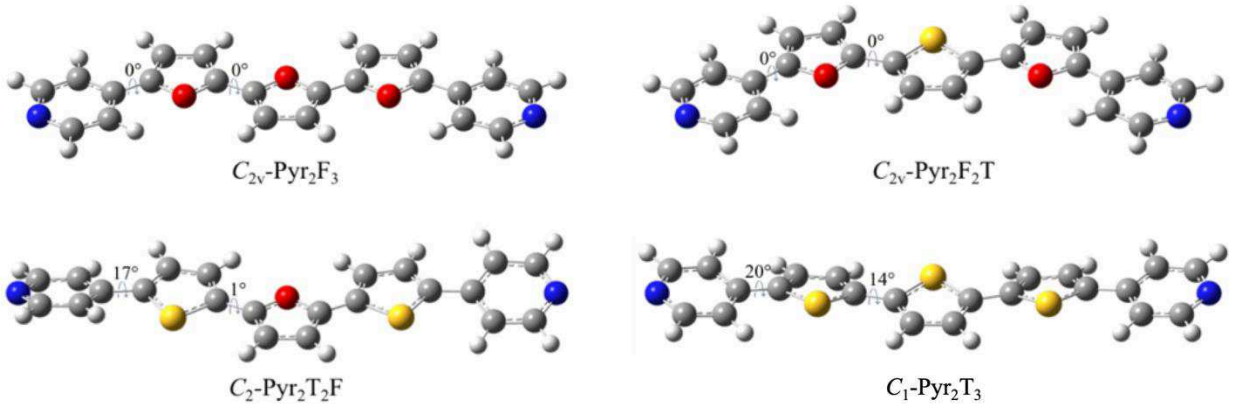

Figure S2. Ground State structures of model oligomers computed at the B3LYP/6-311G(2df,2pd) level of theory. Torsional angles between the inner heterocycles and the pyridyl moieties are indicated in the figure.

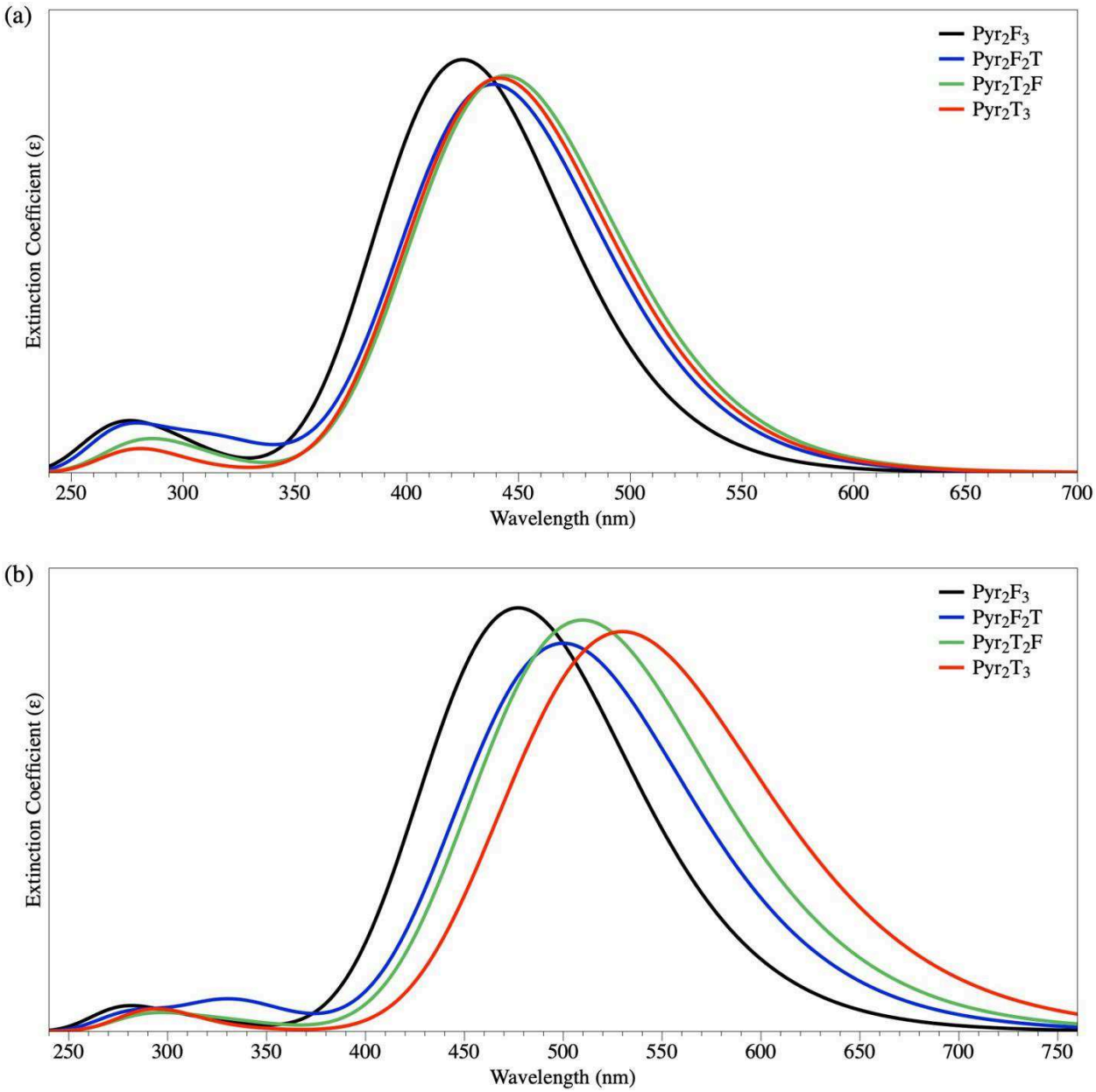

Figure S3. Computed (a) absorption and (b) emission spectra of Pyr_2F_3, Pyr_2F_2T, Pyr_2T_2F, and Pyr_2T_3 from TD-DFT at the B3LYP/6-311G(2*df*, 2*pd*) level of theory. Each absorption and emission curve correspond to the 10 lowest energy excited states and were constructed with a Gaussian line function (FWHM = 0.7 eV). The absorption spectrum corresponds to the lowest 10 energy excited states and the emission spectra corresponds to the lowest energy excited state. The features in the theoretical spectra around 300 nm correspond to higher energy excited states, which exhibit much smaller oscillator strengths ($f < 0.05$) than that of the lowest energy excited state ($f \cong 1.50$).

Table S1. Vertical excitation energies ($E^{vert}_{1\leftarrow 0}$ in eV), oscillator strengths (*f*) of the lowest energy excitation, and atomic orbital contributions of each oligomer at the TD-DFT B3LYP/6-311G(2*df*, 2*pd*) level of theory.

	$\mathbf{E^{vert}_{1\leftarrow 0}}$	***f***	**atomic orbital character**
Pyr_2F_3	2.92	1.54	HOMO: *p*-type LUMO: *p*-type
Pyr_2F_2T	2.83	1.45	HOMO: *p*-type LUMO: *p*-type
Pyr_2T_2F	2.79	1.48	HOMO: *p*-type LUMO: *p*-type
Pyr_2T_3	2.81	1.46	HOMO: *p*-type LUMO: *p*-type

Table S2. B3LYP/6-311G(2*df*,2*pd*) optimized Cartesian coordinates (in Å) and the number of imaginary frequencies (n_i) for ground-state C_{2v} - **Pyr_2F_3**.

$n_i = 0$	*x*	*y*	*z*
C	1.098997	0.031492	0.000000
C	0.708173	1.343206	0.000000
C	–0.708173	1.343206	0.000000
C	–1.098997	0.031492	0.000000
O	0.000000	–0.779511	0.000000
H	1.363723	2.195614	0.000000
H	–1.363723	2.195614	0.000000
C	–4.578640	–0.617065	0.000000
C	–4.173809	–1.924559	0.000000
C	–2.758364	–1.924687	0.000000
C	–2.374268	–0.610360	0.000000
O	–3.473487	0.192285	0.000000
H	–4.815772	–2.787872	0.000000
H	–2.100030	–2.774832	0.000000
C	2.374268	–0.610360	0.000000
C	2.758363	–1.924687	0.000000
C	4.173809	–1.924560	0.000000

C	4.578640	–0.617065	0.000000
O	3.473486	0.192285	0.000000
H	2.100030	–2.774832	0.000000
H	4.815772	–2.787872	0.000000
C	–8.276564	–0.069794	0.000000
C	–7.058346	–0.727054	0.000000
C	–5.876534	0.023885	0.000000
C	–6.011254	1.416441	0.000000
C	–7.281841	1.971075	0.000000
N	–8.409414	1.258905	0.000000
H	–9.197607	–0.642190	0.000000
H	–7.032266	–1.807706	0.000000
H	–5.138814	2.052458	0.000000
H	–7.397957	3.049350	0.000000
C	7.281840	1.971074	0.000000
C	6.011254	1.416441	0.000000
C	5.876534	0.023884	0.000000
C	7.058345	–0.727055	0.000000
C	8.276564	–0.069794	0.000000
N	8.409414	1.258904	0.000000
H	7.397957	3.049349	0.000000
H	5.138814	2.052458	0.000000
H	7.032266	–1.807707	0.000000
H	9.197606	–0.642190	0.000000

Table S3. B3LYP/6-311G(2*df*,2*pd*) optimized Cartesian coordinates (in Å) and the number of imaginary frequencies (n_i) for ground-state C_{2v} - **Pyr$_2$F$_2$T**.

$n_i = 0$	*x*	*y*	*z*
C	1.252022	–0.632489	–0.013510
C	0.702126	0.628381	–0.007920

C	–0.705663	0.625784	0.007837
C	–1.250902	–0.637106	0.013600
H	1.305041	1.522873	–0.013408
H	–1.311874	1.518046	0.013201
C	–4.797474	–0.551095	0.071123
C	–4.677231	–1.913539	0.024794
C	–3.293926	–2.207902	–0.003800
C	–2.635491	–1.006146	0.026156
O	–3.547619	0.006695	0.072633
H	–5.485306	–2.623591	0.014735
H	–2.837955	–3.181912	–0.043837
C	2.637963	–0.996420	–0.026016
C	3.300828	–2.195734	0.004105
C	4.683038	–1.896272	–0.024530
C	4.798253	–0.533400	–0.071046
O	3.546348	0.019774	–0.072633
H	2.848455	–3.171413	0.044276
H	5.493728	–2.603335	–0.014374
C	–8.299167	0.755778	0.133324
C	–7.245038	–0.139876	0.082044
C	–5.932417	0.346273	0.120100
C	–5.773453	1.733455	0.208412
C	–6.900209	2.539920	0.253605
N	–8.151586	2.080214	0.218089
H	–9.319428	0.389490	0.104042
H	–7.445121	–1.199766	0.010891
H	–4.787661	2.172328	0.242874
H	–6.788640	3.616473	0.322523
C	6.889566	2.565330	–0.253953

C	5.765794	1.754718	–0.208649
C	5.929876	0.368144	–0.120147
C	7.244282	–0.113153	–0.082025
C	8.295099	0.786378	–0.133428
N	8.142631	2.110249	–0.218374
H	6.774025	3.641454	–0.323019
H	4.778389	2.189945	–0.243171
H	7.448275	–1.172287	–0.010726
H	9.316705	0.423862	–0.104096
S	0.002795	–1.846059	0.000128

Table S4. B3LYP/6-311G(2*df*,2*pd*) optimized Cartesian coordinates (in Å) and the number of imaginary frequencies (n_i) for ground-state C_2 - **Pyr$_2$T$_2$F**.

$n_i = 0$	*x*	*y*	*z*
C	–1.104462	–0.765743	0.004728
C	–0.707356	–2.076772	0.003585
C	0.707358	–2.076773	–0.003526
C	1.104464	–0.765743	–0.004702
H	–1.355496	–2.935943	0.007718
H	1.355498	–2.935943	–0.007638
C	4.832328	0.426415	–0.003463
C	4.019406	1.534027	–0.021847
C	2.643306	1.235635	–0.027127
C	2.381237	–0.115296	–0.009410
H	4.404597	2.541937	–0.056068
H	1.861680	1.978593	–0.049438
C	–2.381235	–0.115296	0.009419
C	–2.643304	1.235636	0.027104
C	–4.019404	1.534028	0.021818
C	–4.832326	0.426415	0.003461

H	–1.861678	1.978595	0.049397
H	–4.404594	2.541939	0.056014
C	8.442985	1.383020	0.348123
C	7.061083	1.476367	0.368758
C	6.289673	0.367157	–0.000866
C	6.994106	–0.785996	–0.365092
C	8.380149	–0.775891	–0.345044
N	9.113460	0.282632	0.000674
H	9.044414	2.239026	0.633896
H	6.592833	2.396135	0.688981
H	6.471942	–1.679709	–0.678886
H	8.929179	–1.667357	–0.627640
C	–8.380147	–0.775882	0.345073
C	–6.994103	–0.785987	0.365121
C	–6.289671	0.367158	0.000866
C	–7.061081	1.476358	–0.368784
C	–8.442983	1.383012	–0.348145
N	–9.113458	0.282632	–0.000669
H	–8.929176	–1.667341	0.627692
H	–6.471939	–1.679692	0.678936
H	–6.592831	2.396118	–0.689030
H	–9.044412	2.239011	–0.633939
S	–3.862286	–1.023292	–0.015139
S	3.862288	–1.023292	0.015171
O	0.000001	0.040636	0.000003

Table S5. B3LYP/6-311G(2*df*,2*pd*) optimized Cartesian coordinates (in Å) and the number of imaginary frequencies (n_i) for ground-state C_1 - **Pyr$_2$T$_3$**.

$n_i = 0$	*x*	*y*	*z*
C	–1.257943	–0.007295	0.197238

C	–0.705252	1.220018	0.481266
C	0.702307	1.219876	0.492585
C	1.258822	–0.007372	0.216382
H	–1.301551	2.093301	0.701236
H	1.295867	2.092138	0.723540
C	5.161527	–0.364330	–0.004920
C	4.619329	–1.622120	0.101897
C	3.213934	–1.632641	0.191688
C	2.649712	–0.377935	0.151157
H	5.220482	–2.517623	0.148137
H	2.630297	–2.533803	0.309214
C	–2.647826	–0.378272	0.114263
C	–3.207600	–1.635514	0.094013
C	–4.613470	–1.626095	0.014080
C	–5.160926	–0.366918	–0.030493
H	–2.619861	–2.540079	0.147934
H	–5.208218	–2.526091	–0.026524
C	8.868828	–0.514066	–0.562916
C	7.543392	–0.910717	–0.492833
C	6.567275	0.014079	–0.101012
C	7.016740	1.306900	0.190261
C	8.366692	1.602451	0.080819
N	9.296021	0.719592	–0.285978
H	9.628442	–1.226287	–0.865908
H	7.273729	–1.922296	–0.760883
H	6.327091	2.073793	0.515853
H	8.718896	2.603105	0.305828
C	–8.334069	1.576344	–0.584865
C	–6.980647	1.283078	–0.522228

C	–6.568122	0.009803	–0.113799
C	–7.583550	–0.897939	0.212645
C	–8.908015	–0.505206	0.110017
N	–9.300015	0.709295	–0.280097
H	–8.657339	2.561580	–0.902327
H	–6.258358	2.036521	–0.805878
H	–7.347536	–1.892903	0.562138
H	–9.697672	–1.204418	0.362280
S	0.002796	–1.179063	–0.085550
S	–3.896718	0.831516	0.021130
S	3.892562	0.829984	–0.014632

Table S6. TD-B3LYP/6-311G(2*df*,2*pd*) optimized Cartesian coordinates (in Å) and the number of imaginary frequencies (n_i) for excited-state C_{2v} - **Pyr$_2$F$_3$**.

$n_i = 0$	*x*	*y*	*z*
C	1.104446	0.005316	0.000013
C	0.693712	1.342691	–0.000006
C	–0.693712	1.342691	–0.000003
C	–1.104446	0.005316	0.000017
O	0.000000	–0.814584	0.000027
H	1.354017	2.191587	–0.000019
H	–1.354017	2.191587	–0.000014
C	–4.575937	–0.593640	0.000023
C	–4.164677	–1.921740	0.000043
C	–2.771722	–1.931646	0.000044
C	–2.361933	–0.598665	0.000026
O	–3.467038	0.215970	0.000013
H	–4.814634	–2.778898	0.000054
H	–2.116055	–2.784481	0.000056
C	2.361933	–0.598666	0.000017

C	2.771722	–1.931646	0.000035
C	4.164677	–1.921741	0.000028
C	4.575937	–0.593640	0.000006
O	3.467038	0.215970	0.000000
H	2.116055	–2.784481	0.000050
H	4.814634	–2.778898	0.000037
C	–8.267177	–0.081215	0.000009
C	–7.049114	–0.731453	0.000021
C	–5.862126	0.029086	0.000012
C	–6.011928	1.430154	–0.000007
C	–7.284521	1.971079	–0.000018
N	–8.411634	1.250646	–0.000010
H	–9.184876	–0.659363	0.000015
H	–7.018772	–1.812207	0.000036
H	–5.145184	2.074208	–0.000014
H	–7.409154	3.048697	–0.000033
C	7.284521	1.971078	–0.000050
C	6.011928	1.430153	–0.000033
C	5.862126	0.029086	–0.000011
C	7.049114	–0.731453	–0.000007
C	8.267177	–0.081215	–0.000025
N	8.411634	1.250645	–0.000046
H	7.409154	3.048696	–0.000067
H	5.145184	2.074207	–0.000037
H	7.018772	–1.812207	0.000010
H	9.184876	–0.659363	–0.000022

Table S7. TD-B3LYP/6-311G(2*df*,2*pd*) optimized Cartesian coordinates (in Å) and the number of imaginary frequencies (n_i) for excited-state C_{2v} - **Pyr$_2$F$_2$T**.

$n_i = 0$	x	y	z
C	1.255036	–0.593845	–0.000475
C	0.688826	0.697487	0.000022
C	–0.688827	0.697487	0.000567
C	–1.255038	–0.593844	0.000528
H	1.301132	1.585327	–0.000049
H	–1.301132	1.585327	0.000992
C	–4.783752	–0.495639	0.001839
C	–4.646089	–1.876570	0.001612
C	–3.282851	–2.162751	0.001069
C	–2.609021	–0.938800	0.000985
O	–3.536647	0.075290	0.001462
H	–5.453360	–2.587740	0.001809
H	–2.818402	–3.133890	0.000773
C	2.609019	–0.938801	–0.001139
C	3.282848	–2.162754	–0.001786
C	4.646087	–1.876575	–0.002336
C	4.783751	–0.495644	–0.002004
O	3.536647	0.075287	–0.001268
H	2.818397	–3.133893	–0.001846
H	5.453356	–2.587746	–0.002893
C	–8.299756	0.740856	0.003257
C	–7.234571	–0.138333	0.002816
C	–5.921484	0.371261	0.002328
C	–5.789145	1.772643	0.002329

C	–6.929190	2.556445	0.002792
N	–8.175748	2.073987	0.003254
H	–9.314083	0.356948	0.003637
H	–7.418866	–1.203581	0.002855
H	–4.811569	2.231036	0.001961
H	–6.837324	3.637279	0.002790
C	6.929194	2.556437	–0.001820
C	5.789148	1.772637	–0.001538
C	5.921485	0.371255	–0.002256
C	7.234571	–0.138341	–0.003239
C	8.299757	0.740846	–0.003443
N	8.175752	2.073977	–0.002753
H	6.837331	3.637271	–0.001265
H	4.811573	2.231031	–0.000759
H	7.418864	–1.203590	–0.003853
H	9.314083	0.356936	–0.004205
S	–0.000002	–1.826317	–0.000216

Table S8. TD-B3LYP/6-311G(2*df*,2*pd*) optimized Cartesian coordinates (in Å) and the number of imaginary frequencies (n_i) for excited-state C_{2v} - **Pyr$_2$T$_2$F**.

$n_i = 0$	x	y	z
C	-1.110024	-0.717816	0.000005
C	-0.693508	-2.054023	0.000026
C	0.693510	-2.054023	0.000034
C	1.110026	-0.717816	0.000018
H	-1.346773	-2.909416	0.000034
H	1.346775	-2.909416	0.000049
C	4.831209	0.417408	0.000029
C	4.008781	1.547148	0.000008
C	2.651729	1.268144	0.000001

C	2.367238	-0.104808	0.000017
H	4.403109	2.551322	-0.000005
H	1.873539	2.015233	-0.000016
C	-2.367235	-0.104808	-0.000011
C	-2.651727	1.268144	-0.000029
C	-4.008779	1.547148	-0.000041
C	-4.831207	0.417409	-0.000033
H	-1.873536	2.015234	-0.000033
H	-4.403107	2.551322	-0.000053
C	8.438167	1.413009	0.000078
C	7.060685	1.522352	0.000064
C	6.268754	0.355962	0.000043
C	6.973907	-0.863546	0.000039
C	8.356823	-0.856607	0.000054
N	9.103187	0.251876	0.000074
H	9.047107	2.310627	0.000094
H	6.608816	2.503690	0.000071
H	6.448982	-1.809480	0.000022
H	8.898222	-1.796504	0.000051
C	-8.356821	-0.856606	-0.000021
C	-6.973905	-0.863546	-0.000009
C	-6.268752	0.355963	-0.000042
C	-7.060683	1.522352	-0.000087
C	-8.438165	1.413009	-0.000096
N	-9.103185	0.251877	-0.000064
H	-8.898220	-1.796503	0.000004
H	-6.448980	-1.809480	0.000029
H	-6.608814	2.503690	-0.000118
H	-9.047105	2.310628	-0.000131

S	-3.852789	-1.036686	-0.000008
S	3.852791	-1.036686	0.000041
O	0.000001	0.094762	0.000000

Table S9. TD-B3LYP/6-311G(2*df*,2*pd*) optimized Cartesian coordinates (in Å) and the number of imaginary frequencies (n_i) for excited-state C_{2v} - **Pyr$_2$T$_3$**.

$n_i = 0$	*x*	*y*	*z*
C	-1.263824	-0.009335	0.001243
C	-0.688924	1.277135	0.000791
C	0.688935	1.277131	-0.000478
C	1.263827	-0.009342	-0.001074
H	-1.290042	2.174187	0.001405
H	1.290058	2.174179	-0.000988
C	5.148376	-0.355183	-0.004620
C	4.581106	-1.629923	-0.004192
C	3.195430	-1.640703	-0.002927
C	2.620546	-0.360413	-0.002324
H	5.175849	-2.530146	-0.004768
H	2.601174	-2.542644	-0.002426
C	-2.620545	-0.360398	0.002466
C	-3.195436	-1.640686	0.002928
C	-4.581112	-1.629898	0.004221
C	-5.148375	-0.355155	0.004810
H	-2.601185	-2.542630	0.002306
H	-5.175860	-2.530117	0.004693
C	8.884831	-0.578529	-0.008201
C	7.559832	-0.972038	-0.007097
C	6.543444	0.003589	-0.005835
C	6.978245	1.342369	-0.005825
C	8.332649	1.624063	-0.006989

N	9.292659	0.695304	-0.008169
H	9.667373	-1.329508	-0.009169
H	7.322224	-2.025942	-0.007241
H	6.267500	2.157805	-0.004887
H	8.666547	2.656005	-0.006967
C	-8.332638	1.624108	0.007380
C	-6.978236	1.342407	0.006146
C	-6.543441	0.003625	0.006097
C	-7.559834	-0.971997	0.007376
C	-8.884831	-0.578482	0.008552
N	-9.292652	0.695353	0.008576
H	-8.666530	2.656052	0.007402
H	-6.267486	2.157839	0.005193
H	-7.322231	-2.025902	0.007489
H	-9.667377	-1.329457	0.009537
S	-0.000002	-1.236135	0.000012
S	-3.888027	0.858913	0.003705
S	3.888034	0.858891	-0.003396

Cyclic Voltammetry

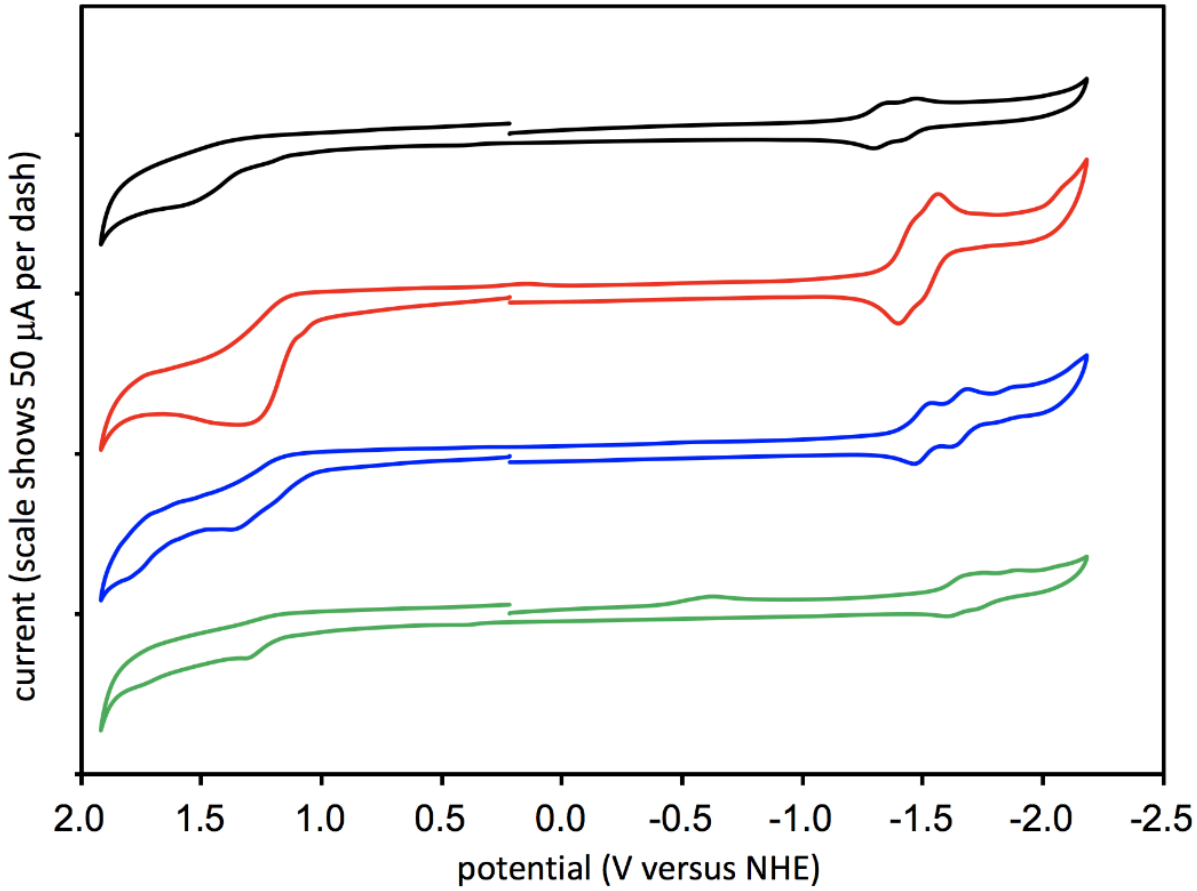

Figure S4. CV scans of **Pyr_2T_3** (black), **Pyr_2T_2F** (red), **Pyr_2F_2T** (blue), and **Pyr_2F_3** (green).

Fluorescence Lifetime Decay Curves and Exponential Decay Fits

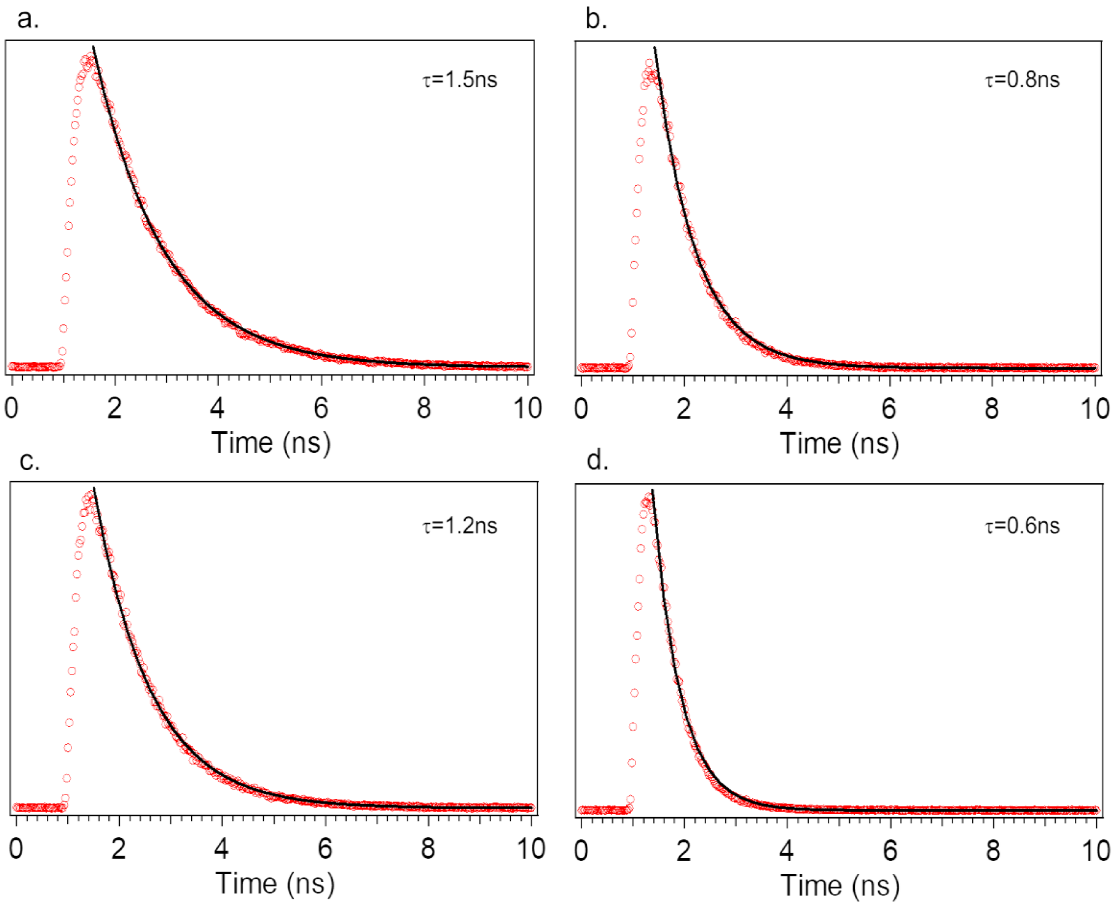

Figure S5. Fluorescence lifetime decay curves and single exponential decay fits of **Pyr_2F_3** (a), **Pyr_2F_2T** (b), **Pyr_2T_2F** (c), and **Pyr_2T_3** (d) in toluene.

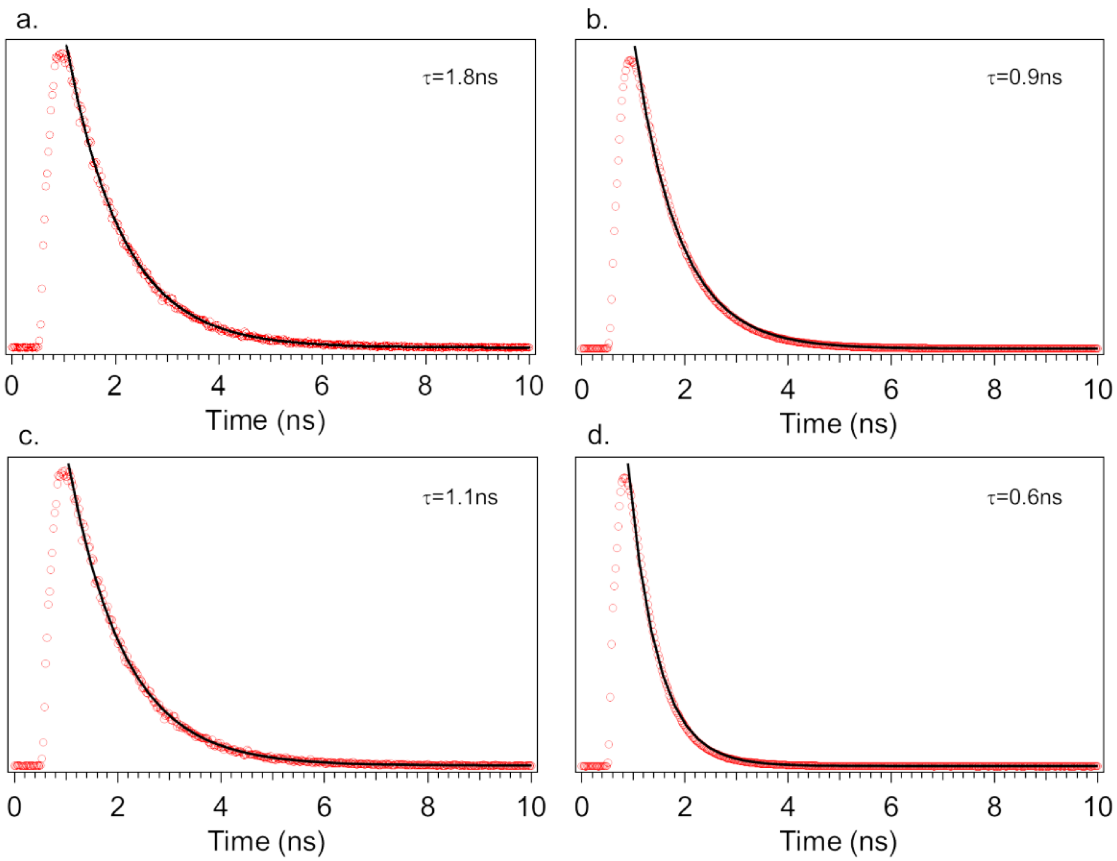

Figure S6. Fluorescence lifetime decay curves and single exponential decay fits of **Pyr$_2$F$_3$** (a), **Pyr$_2$F$_2$T** (b), **Pyr$_2$T$_2$F** (c), and **Pyr$_2$T$_3$** (d) in DMF.

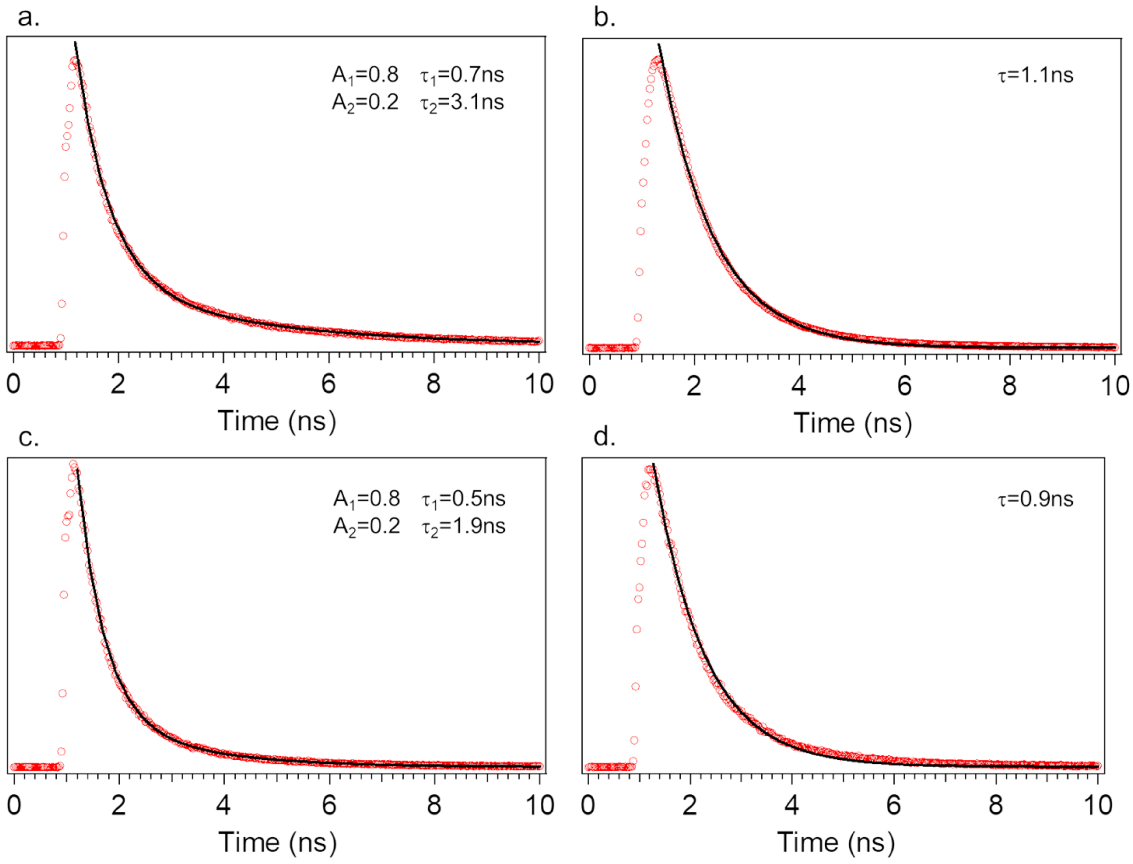

Figure S7. Fluorescence lifetime decay curves and exponential decay fits of **Pyr_2F_3** (a), **Pyr_2F_2T** (b), **Pyr_2T_2F** (c), and **Pyr_2T_3** (d) in the solid state. The amplitudes associated with each lifetime have been included for systems with biexponetial fluorescent decay lifetimes.

Table S10. Uncertainties in the decay curve fits used to calculate the lifetimes of **Pyr_2F_3**, **Pyr_2F_2T**, **Pyr_2T_2F**, and **Pyr_2T_3** in the solid state, in toluene, and in DMF. For biexponential decay fits, the uncertainties associated with the fit for both lifetimes have been included.

	Solid	**Toluene**	**DMF**
Pyr_2F_3	τ_1=0.003 ns τ_2=0.025 ns	0.002 ns	0.001 ns
Pyr_2F_2T	0.001 ns	0.002 ns	0.001 ns
Pyr_2T_2F	τ_1=0.002 ns τ_2=0.018 ns	0.002 ns	0.002 ns
Pyr_2T_3	0.002 ns	0.001 ns	0.001 ns

^{1}H and ^{13}C NMR Spectra

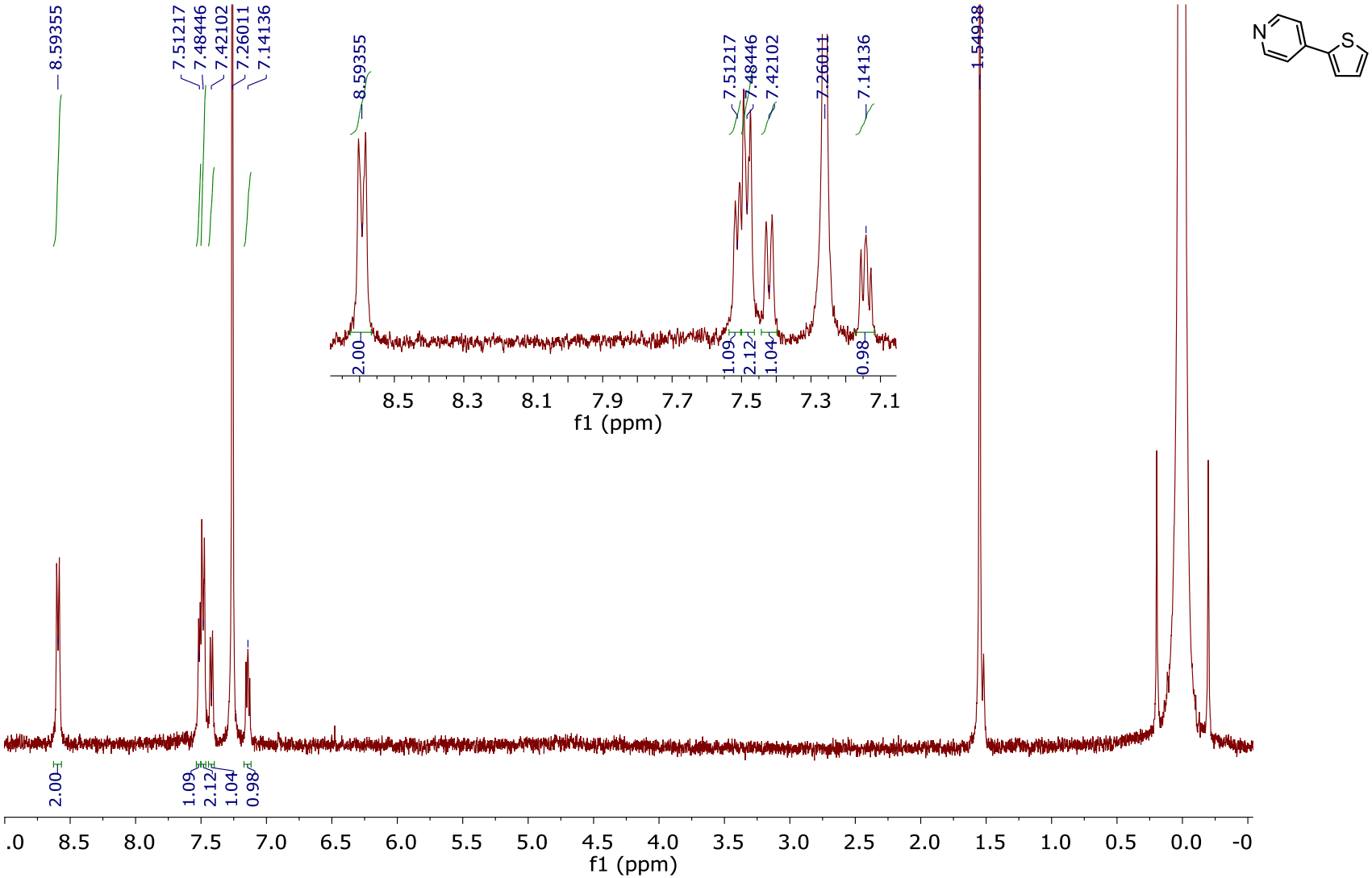

Figure S8. ^{1}H NMR spectrum of compound **2** ($CDCl_3$, 300 MHz).

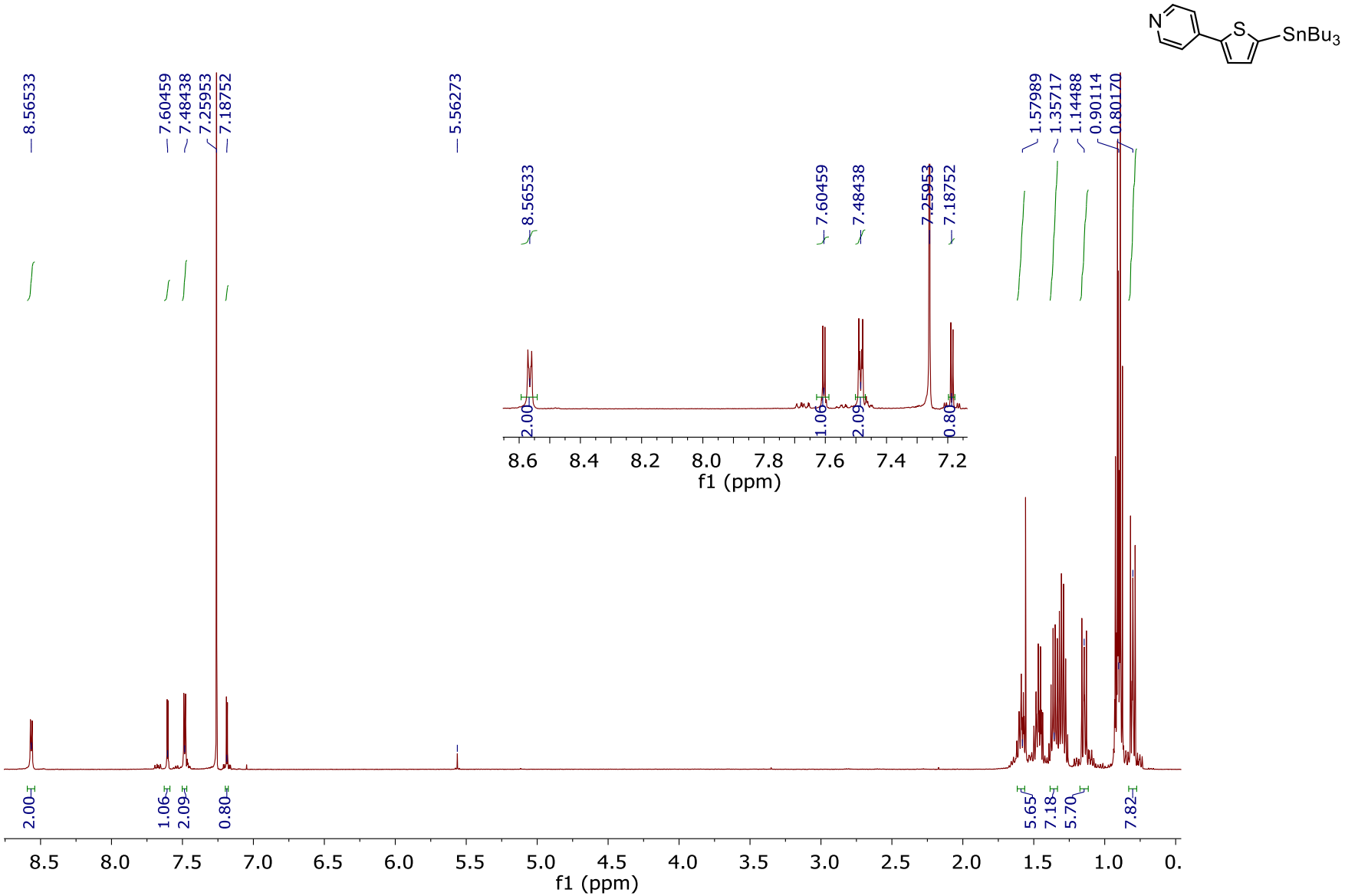

Figure S9. ^{1}H NMR spectrum of compound **3** ($CDCl_3$, 500 MHz).

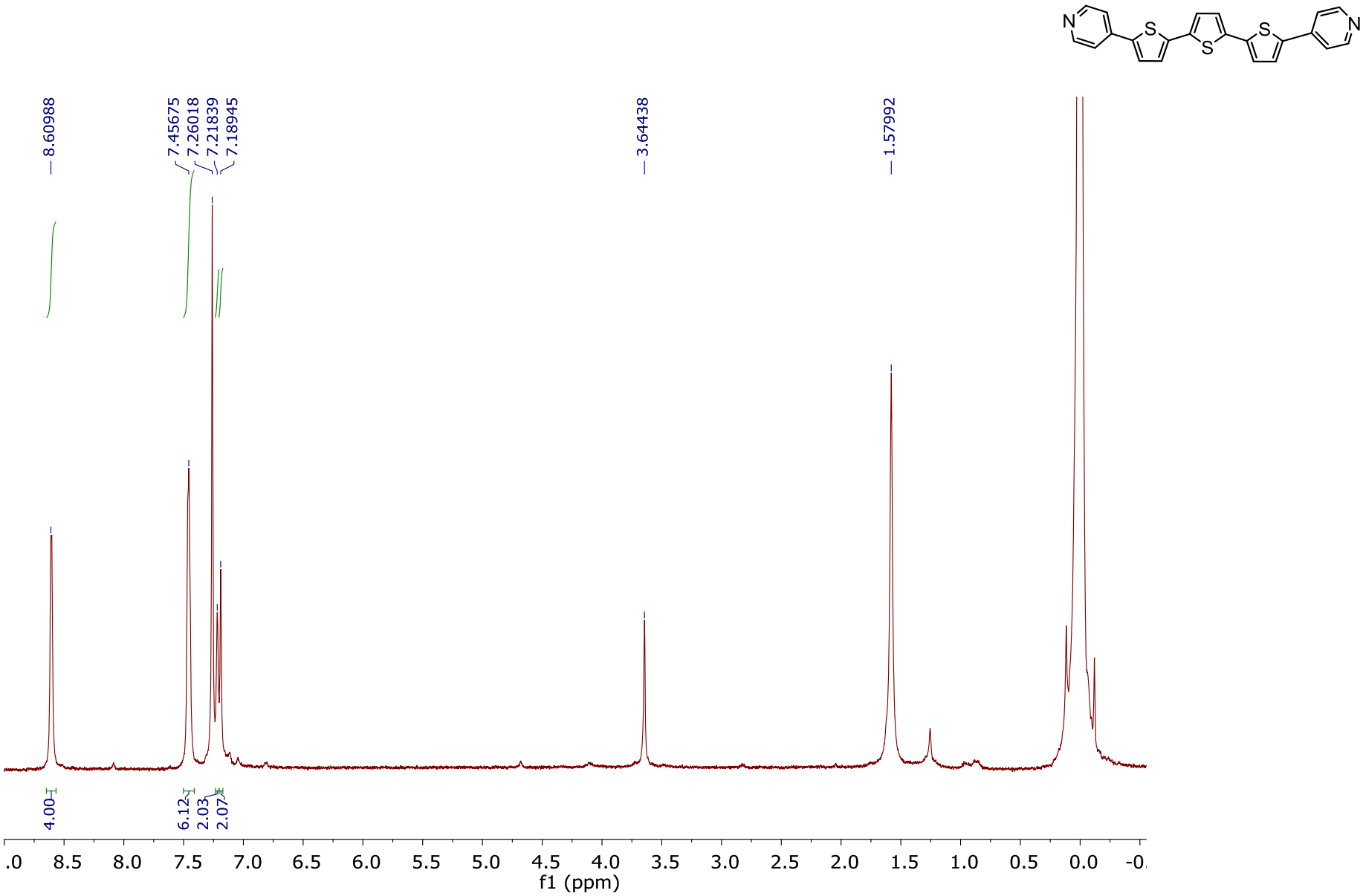

Figure S10. ^{1}H NMR spectrum of compound **4** ($CDCl_3$, 500 MHz).

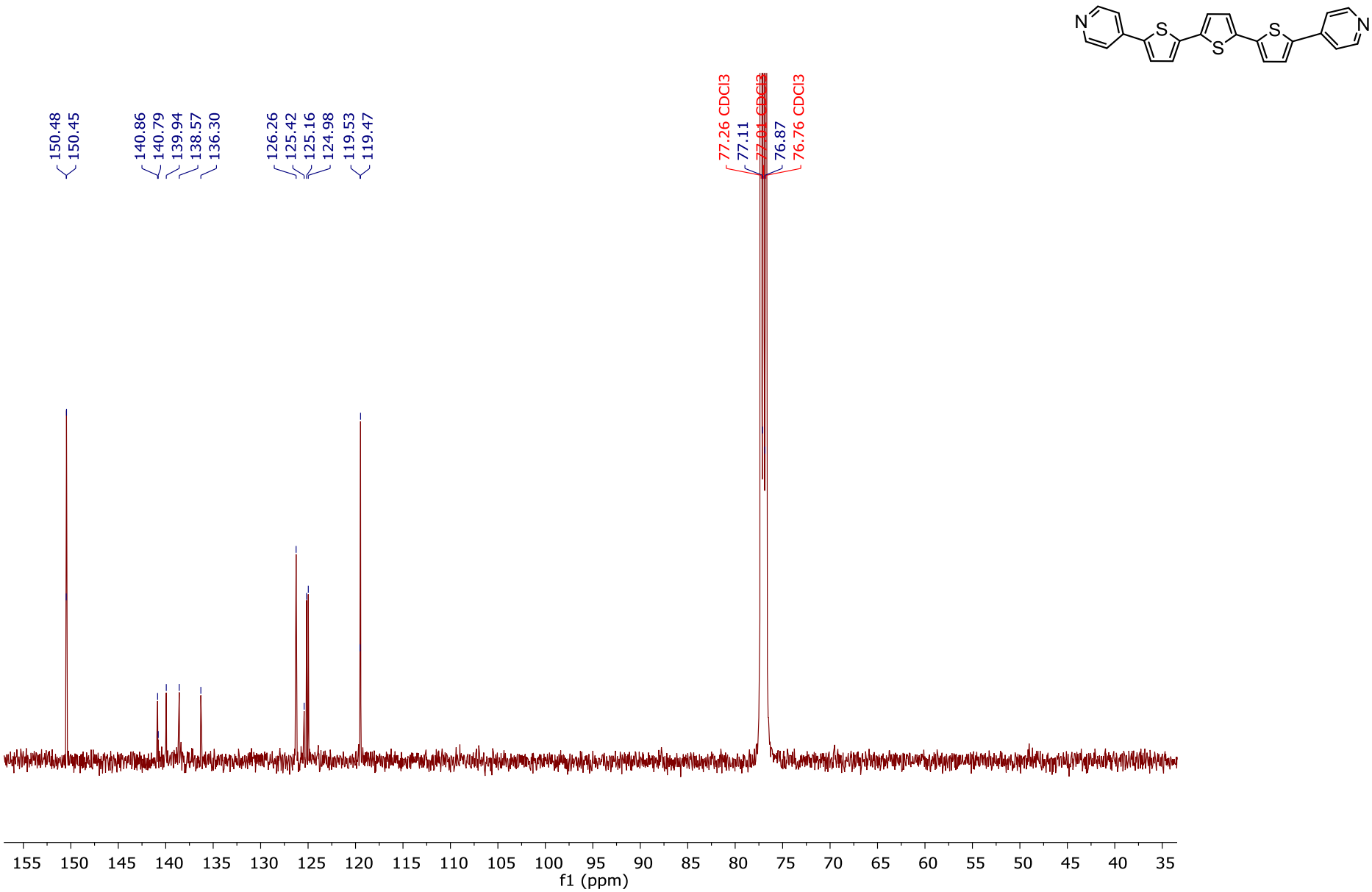

Figure S11. ^{13}C NMR spectrum of compound **4** ($CDCl_3$, 500 MHz).

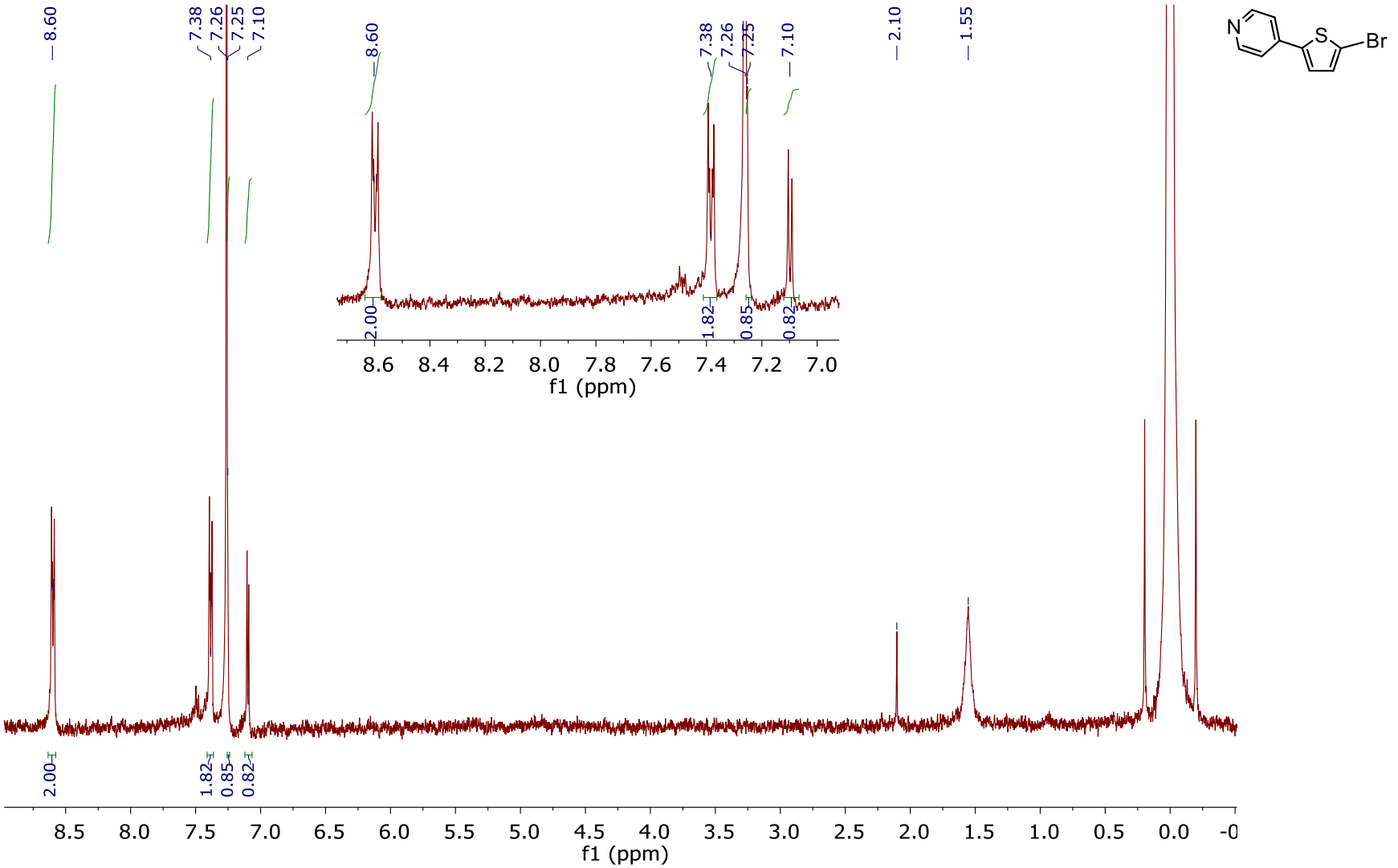

Figure S12. ^{1}H NMR spectrum of compound **5** ($CDCl_3$, 300 MHz).

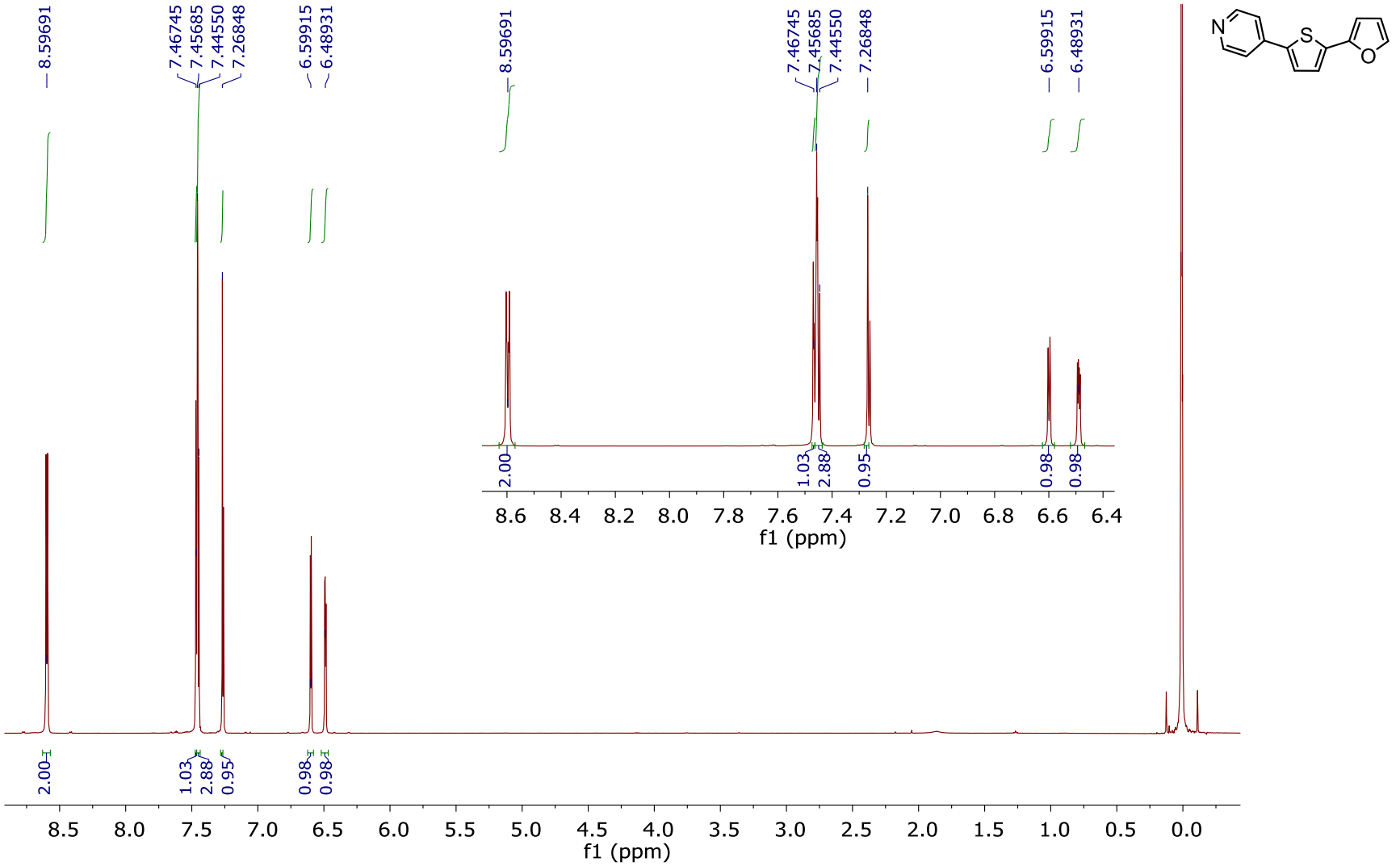

Figure S13. ^{1}H NMR spectrum of compound **6** ($CDCl_3$, 500 MHz).

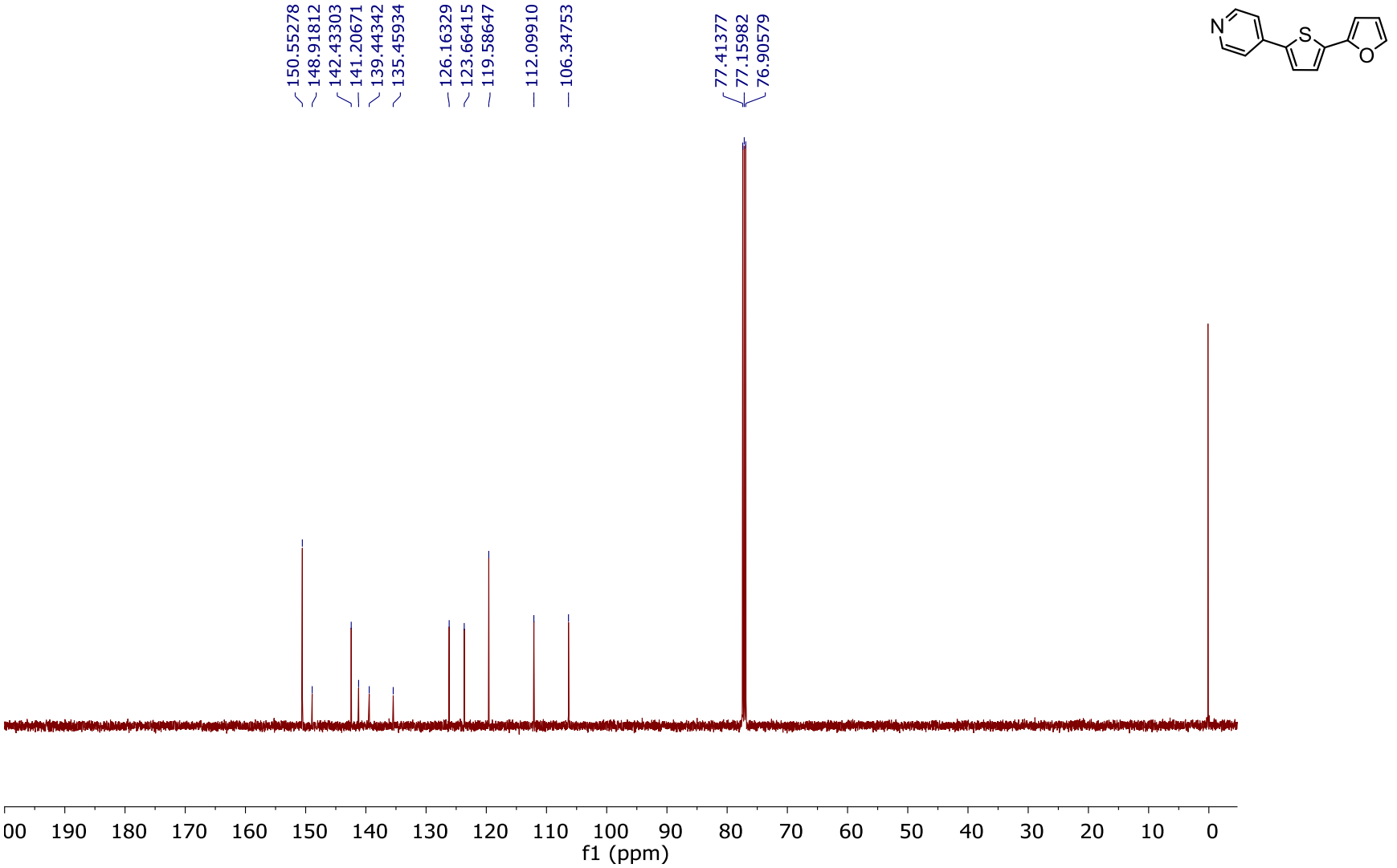

Figure S14. ^{13}C NMR spectrum of compound **6** ($CDCl_3$, 500 MHz).

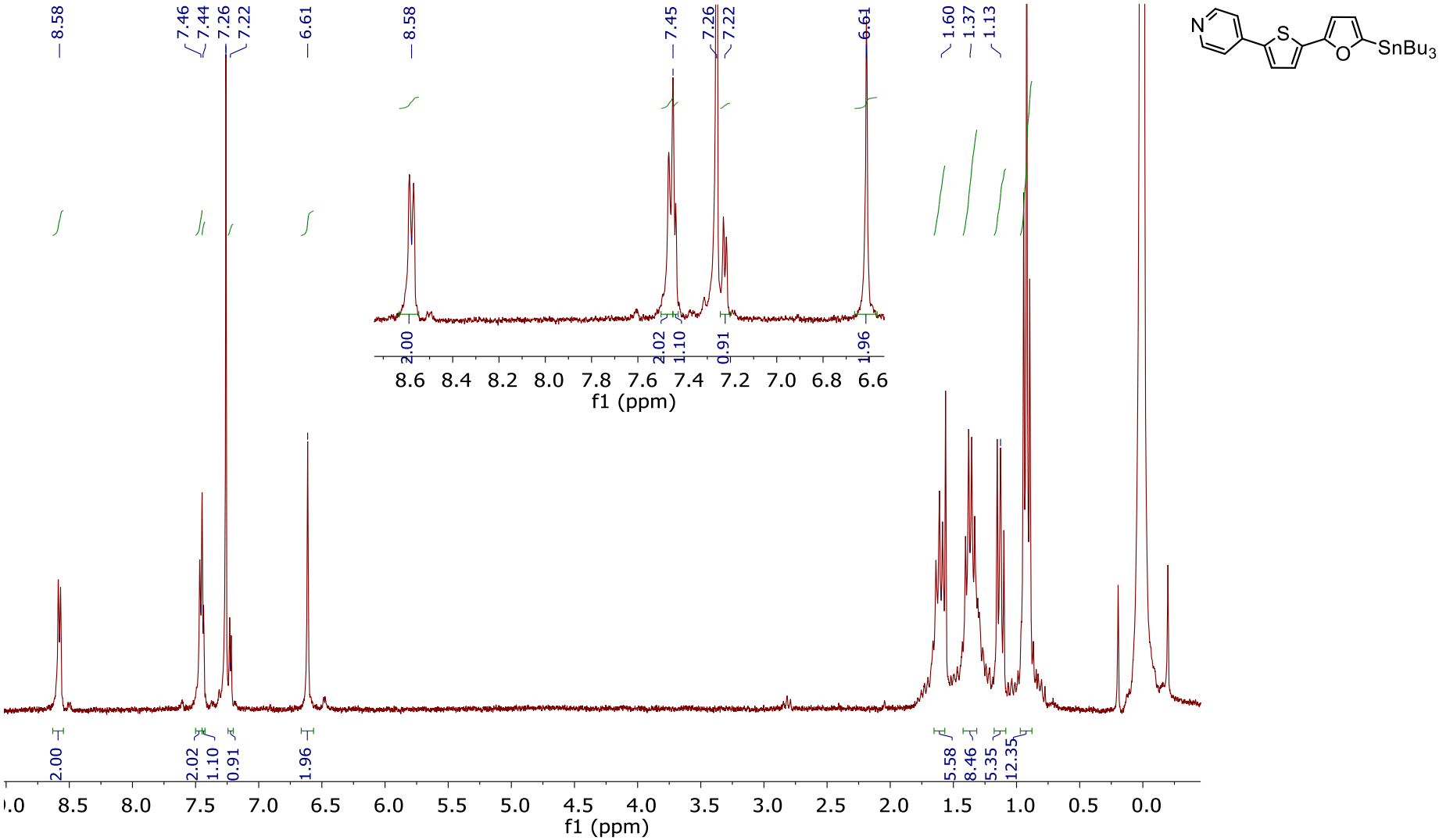

Figure S15. ^{1}H NMR spectrum of compound **7** ($CDCl_3$, 300 MHz).

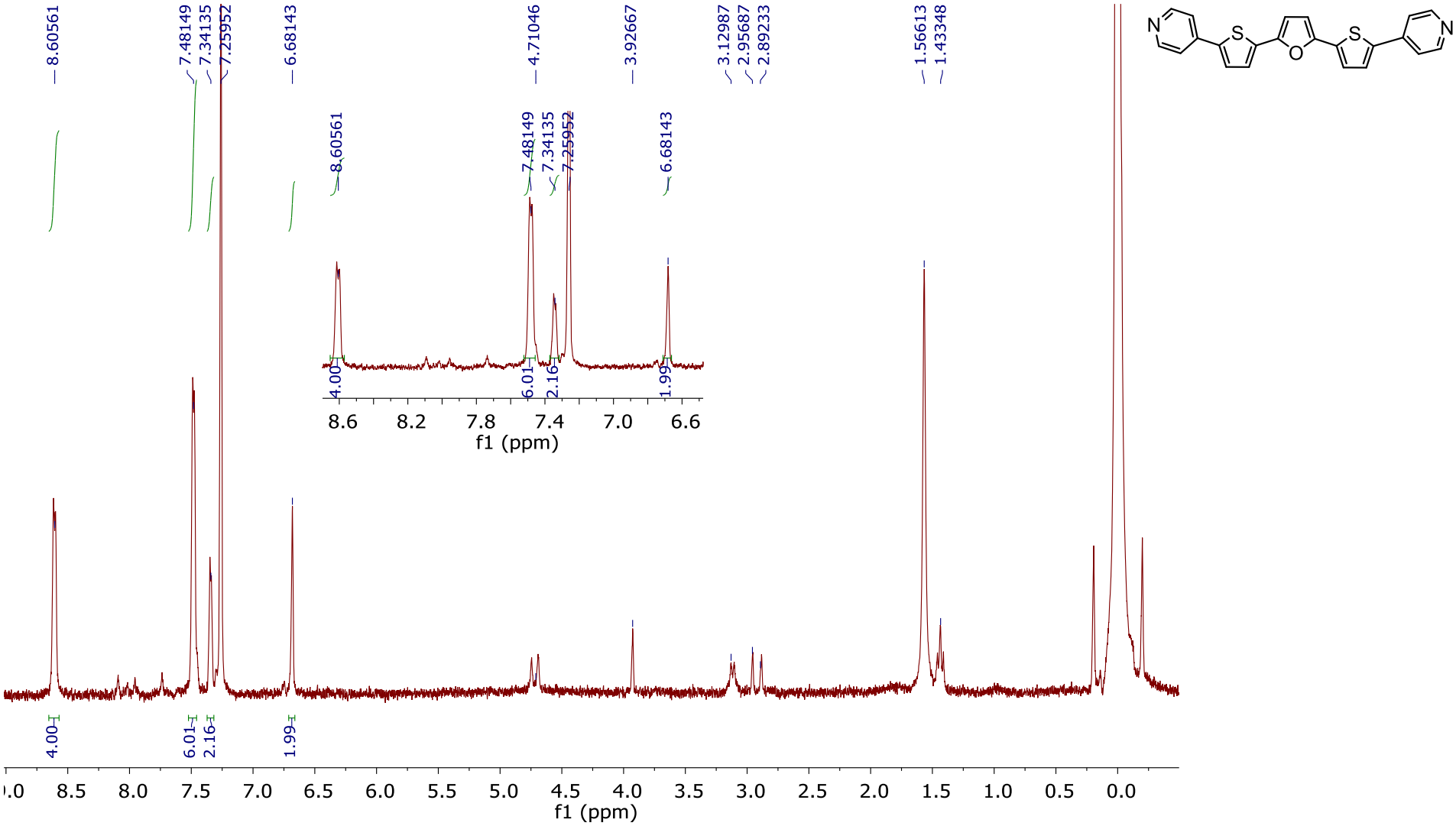

Figure S16. ^{1}H NMR spectrum of compound **8** ($CDCl_3$, 300 MHz). Peaks below 5 ppm are solvent impurities and TEA salts used during purification of the oligomer.

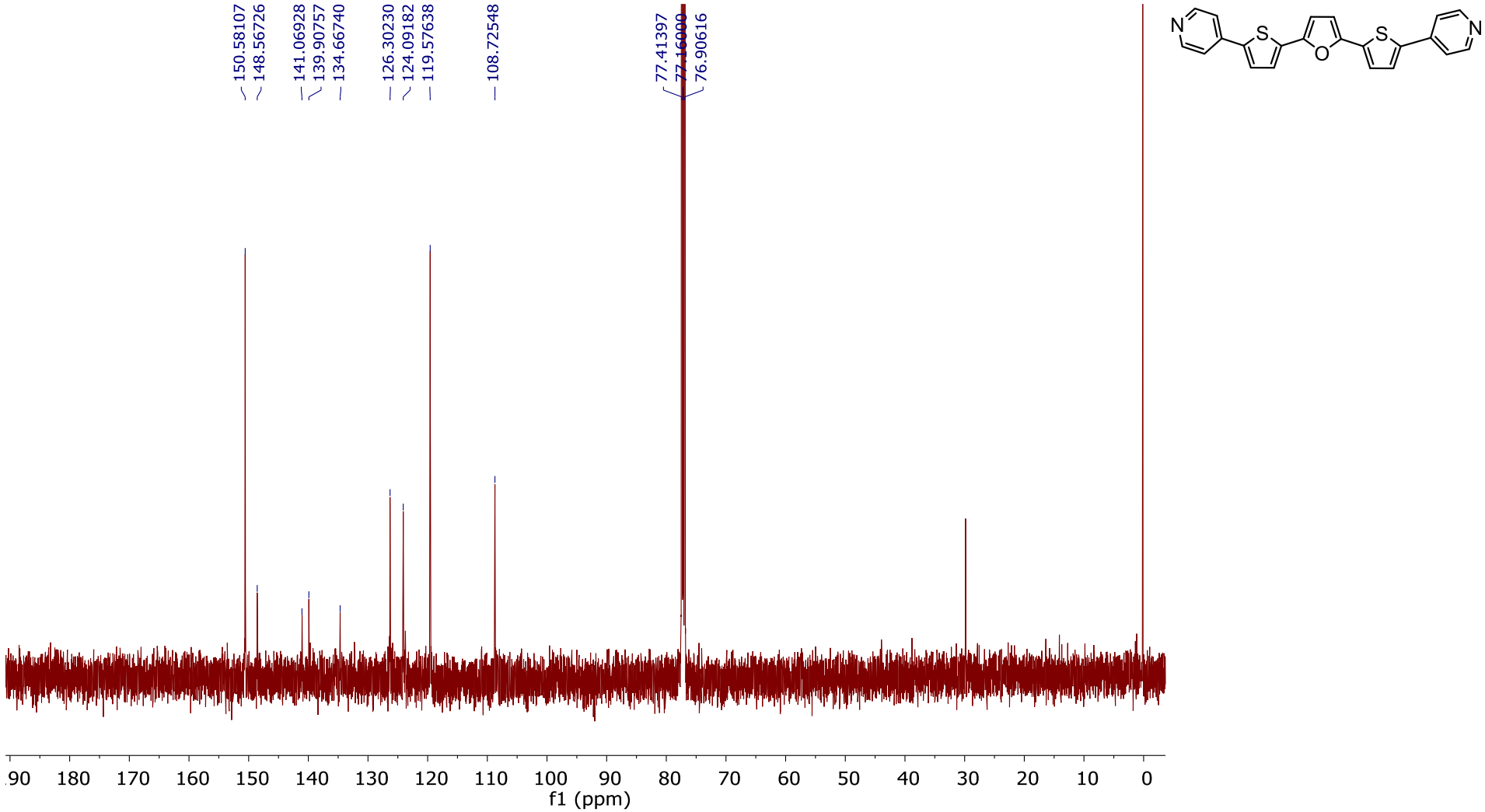

Figure S17. ^{13}C NMR spectrum of compound **8** ($CDCl_3$, 500 MHz).

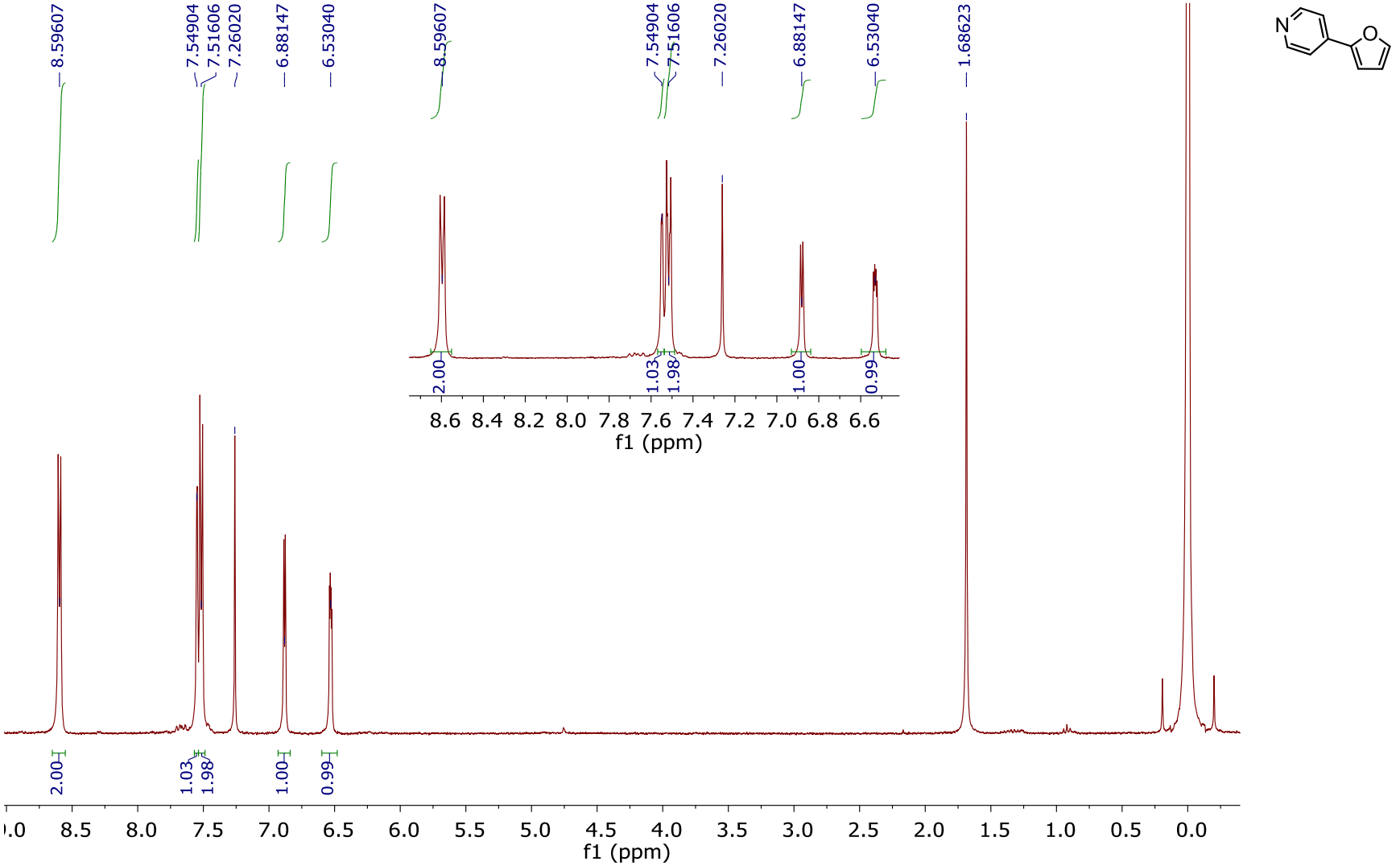

Figure S18. ^{1}H NMR spectrum of compound **9** ($CDCl_3$, 300 MHz).

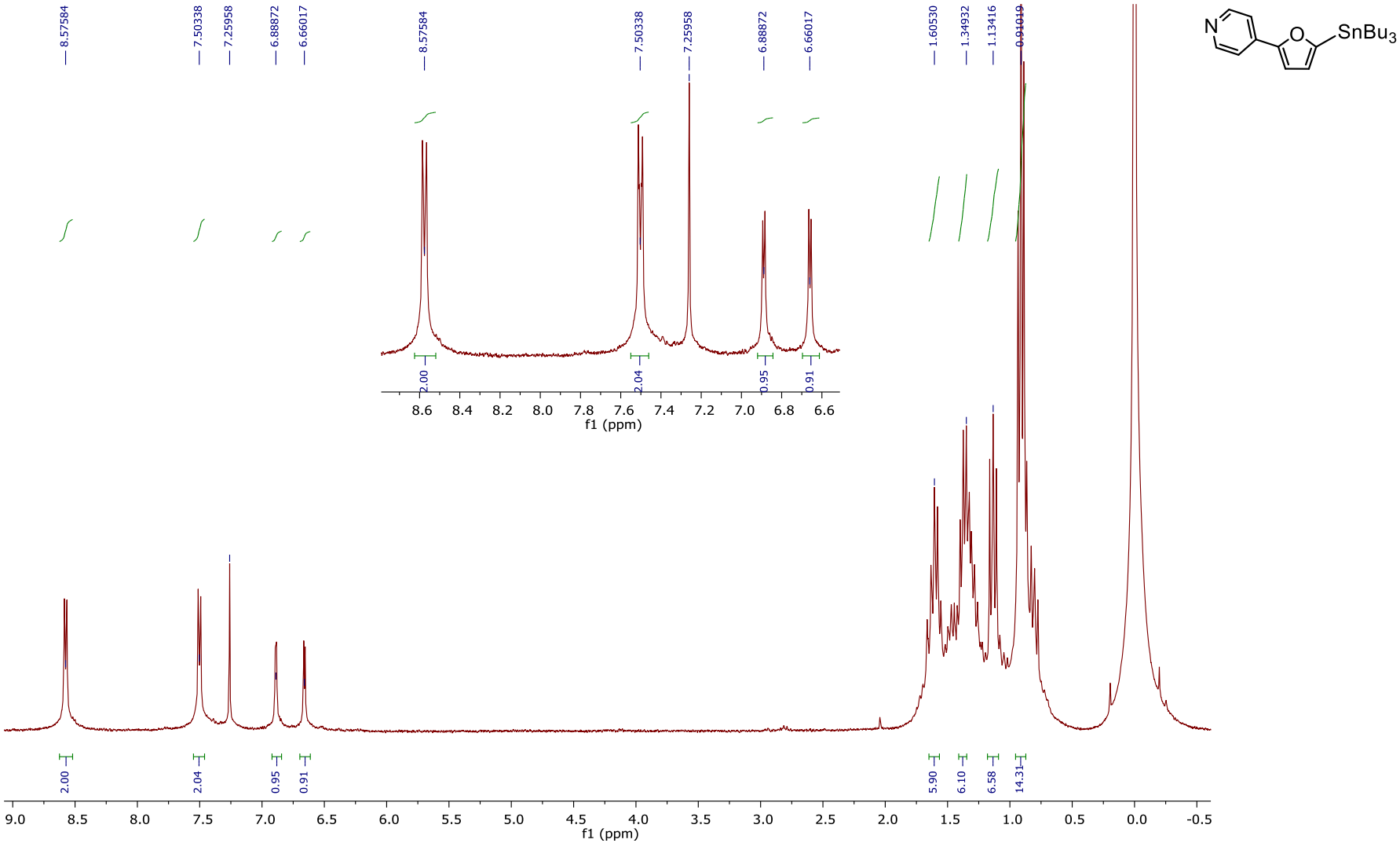

Figure S19. ^{1}H NMR spectrum of compound **10** ($CDCl_3$, 300 MHz).

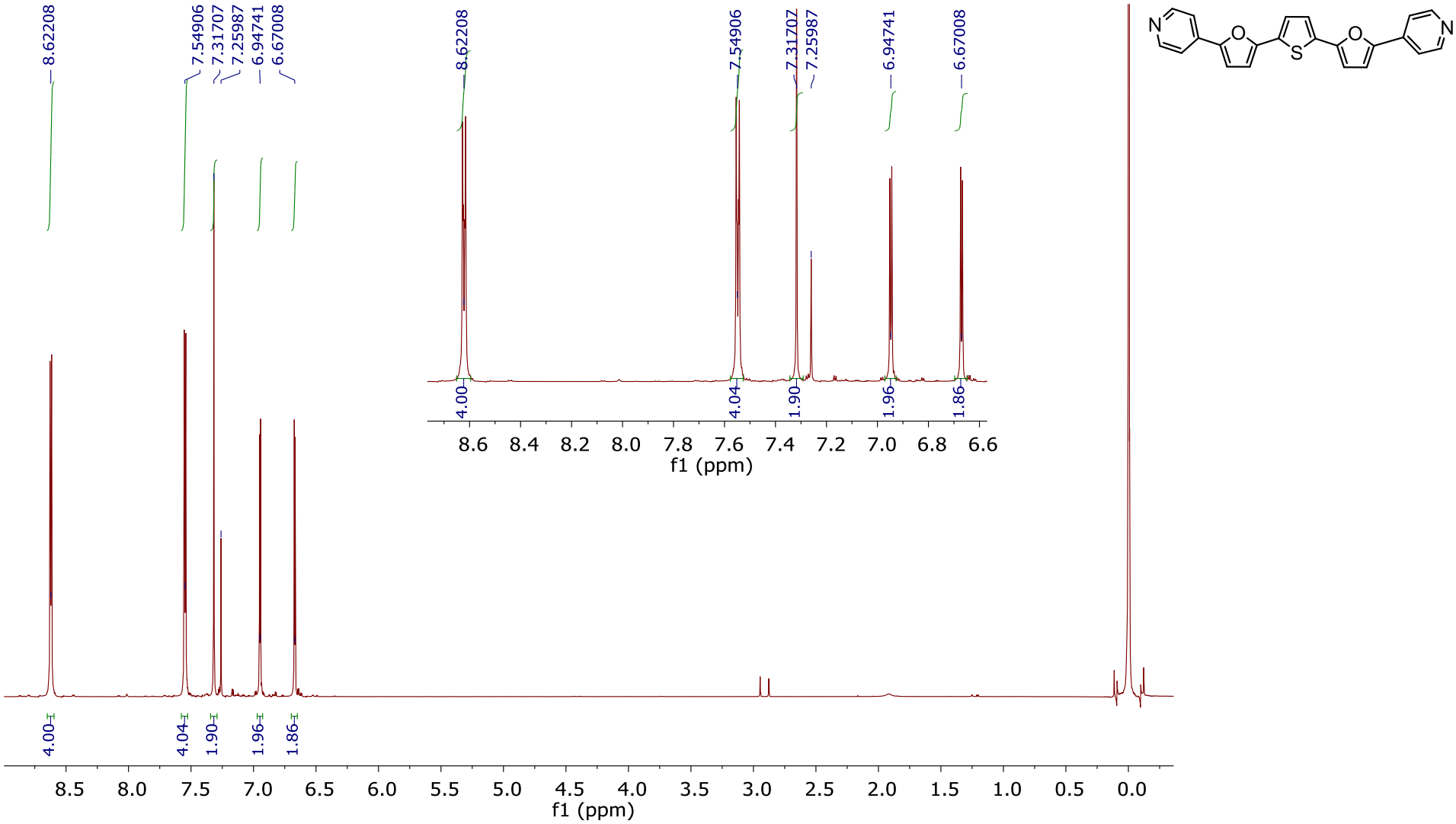

Figure S20. ^{1}H NMR spectrum of compound **11** ($CDCl_3$, 500 MHz).

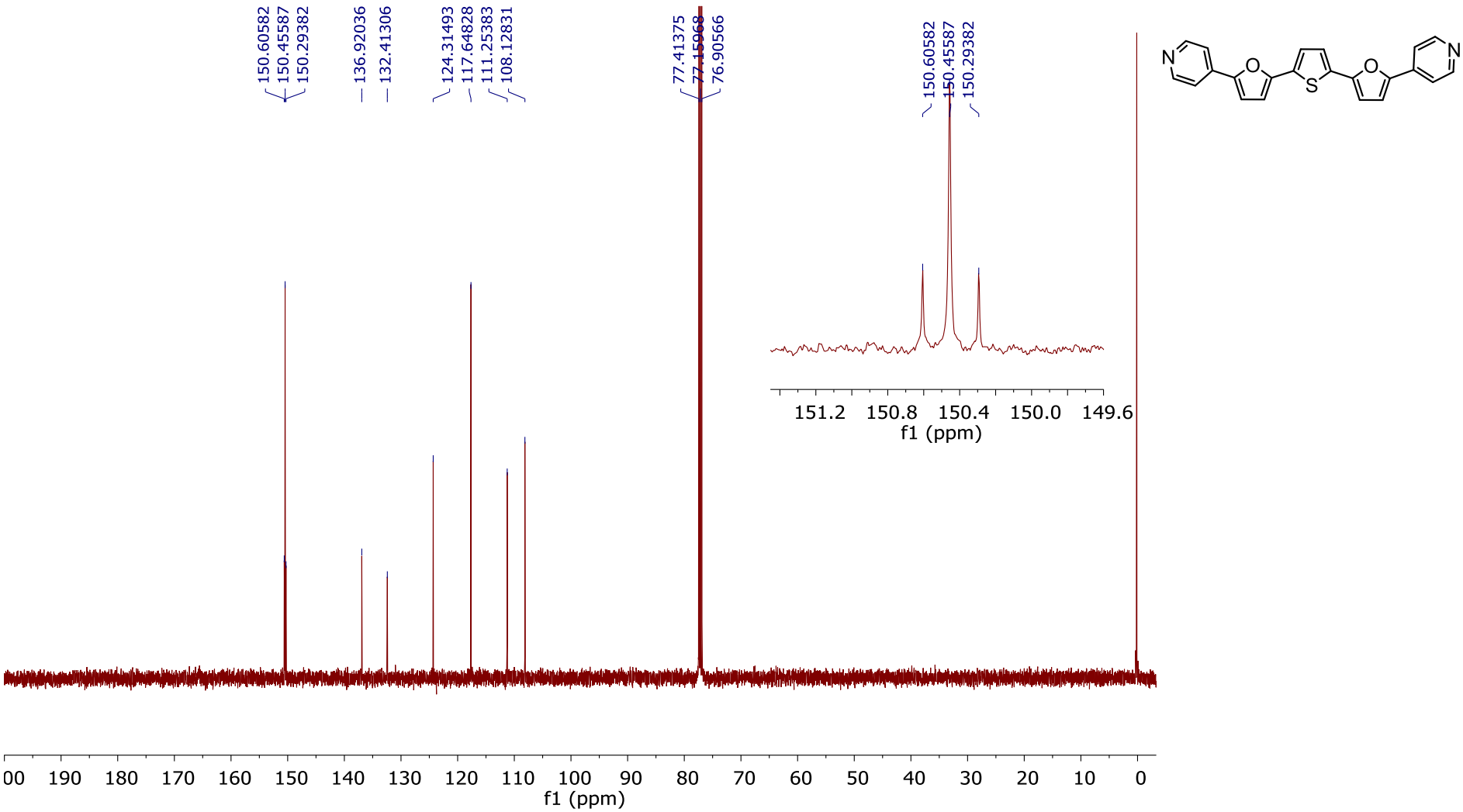

Figure S21. ^{13}C NMR spectrum of compound **11** ($CDCl_3$, 500 MHz).

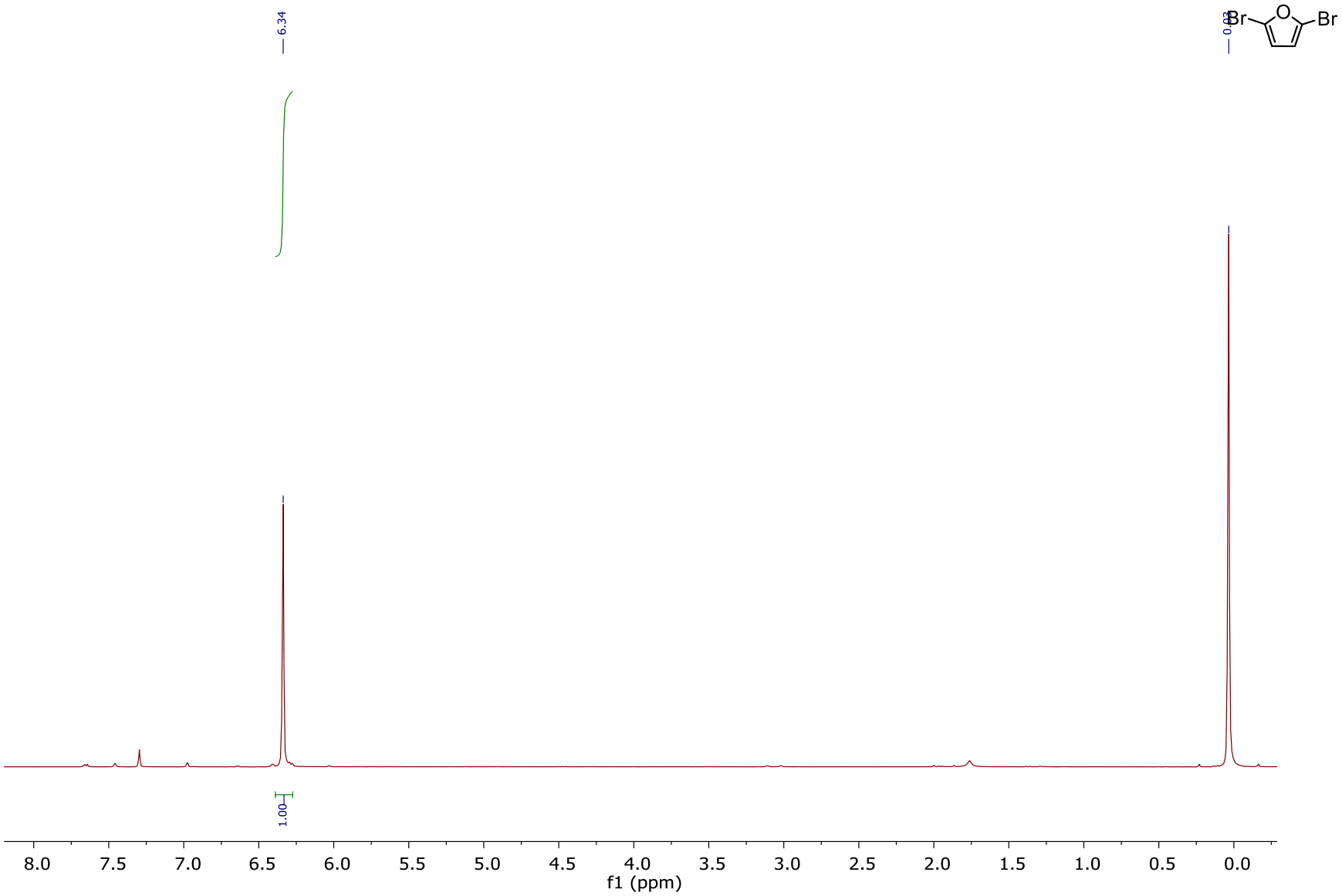

Figure S22. ^{1}H NMR spectrum of compound **13** ($CDCl_3$, 500 MHz).

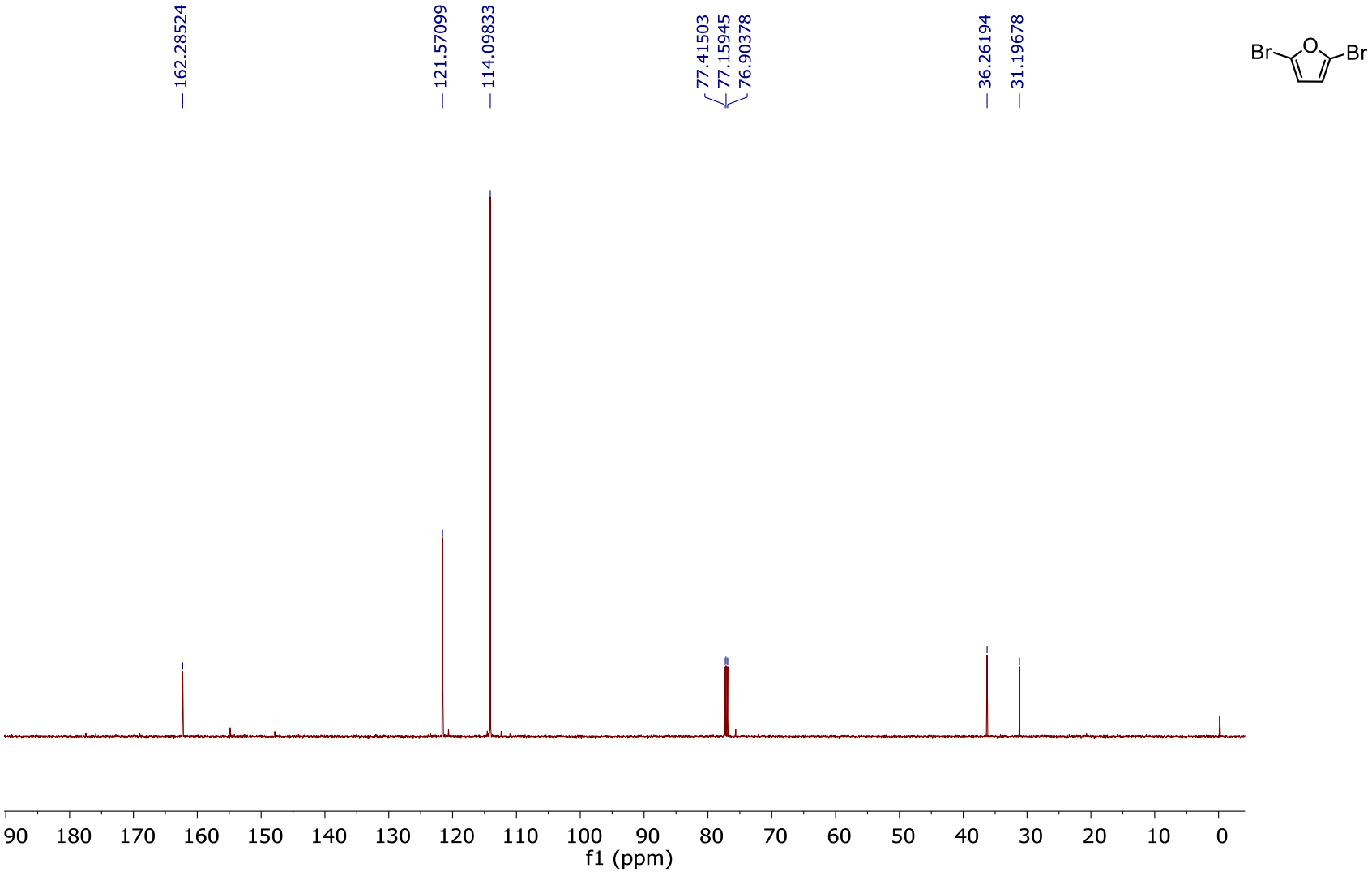

Figure S23. ^{13}C NMR spectrum of compound **13** ($CDCl_3$, 500 MHz).

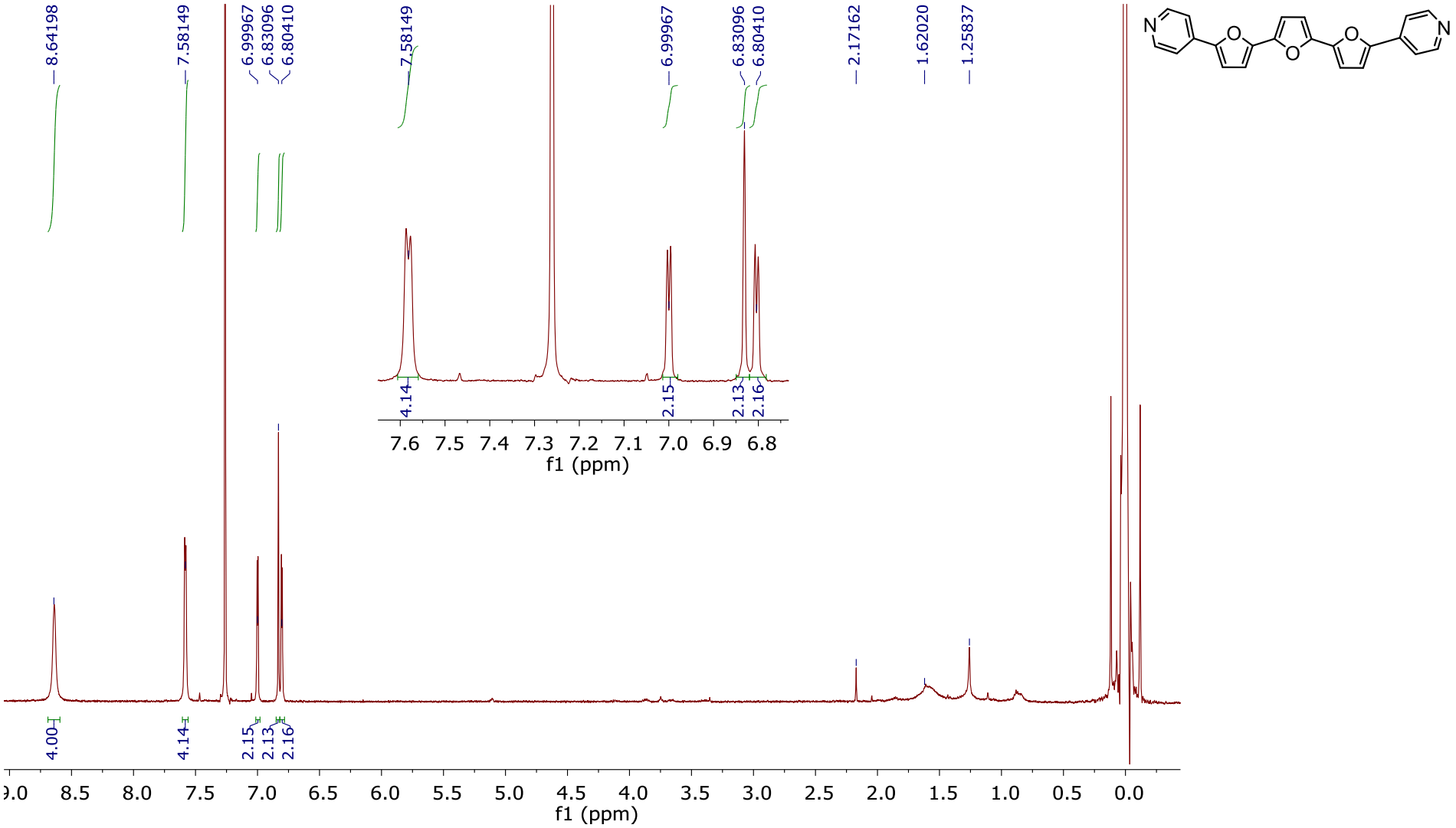

Figure S24. ^{1}H NMR spectrum of compound **14** ($CDCl_3$, 500 MHz).

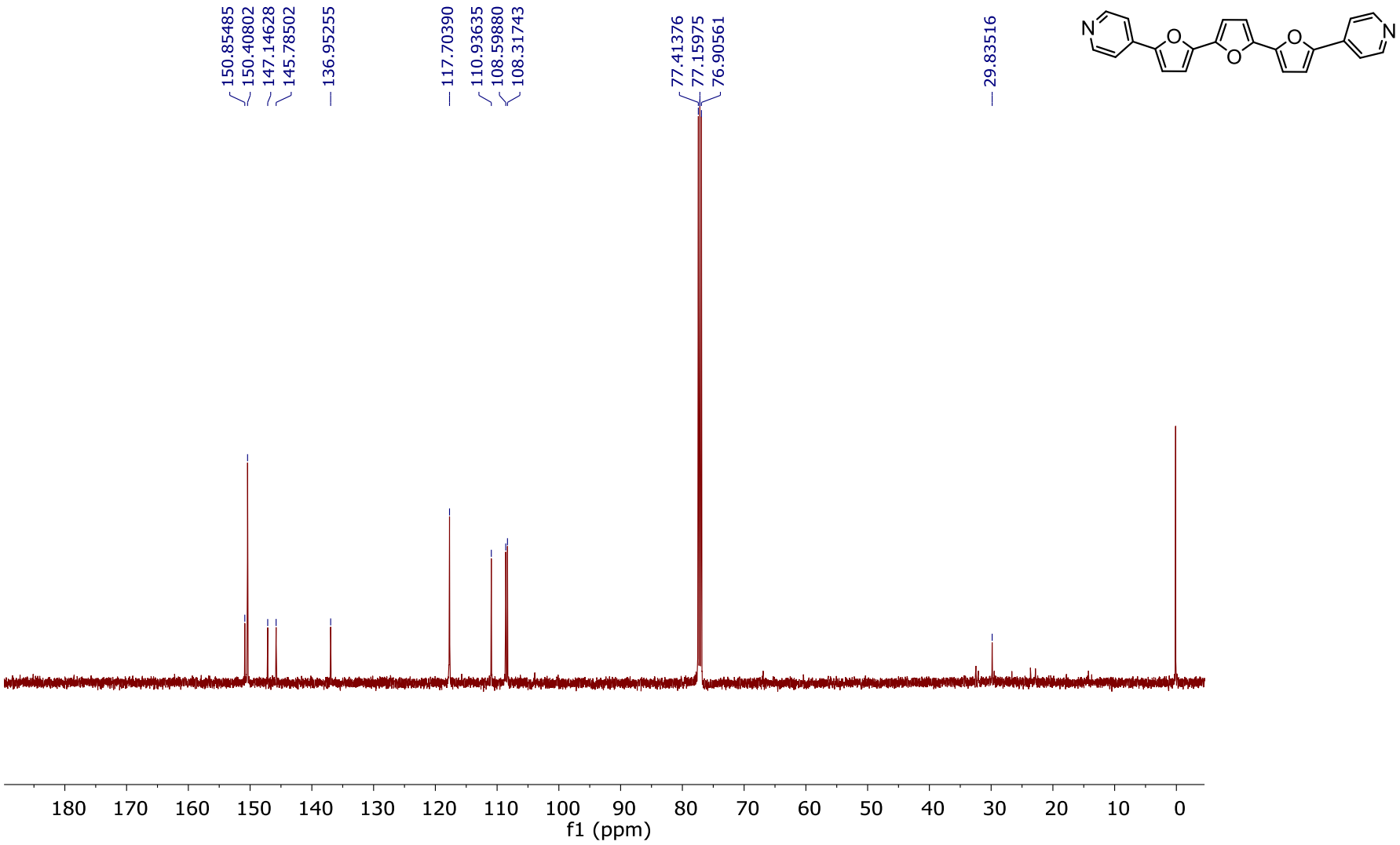

Figure S25. ^{13}C NMR spectrum of compound **14** ($CDCl_3$, 500 MHz).

Mass Spectrometry Analysis Report for Pyr_2T_2F

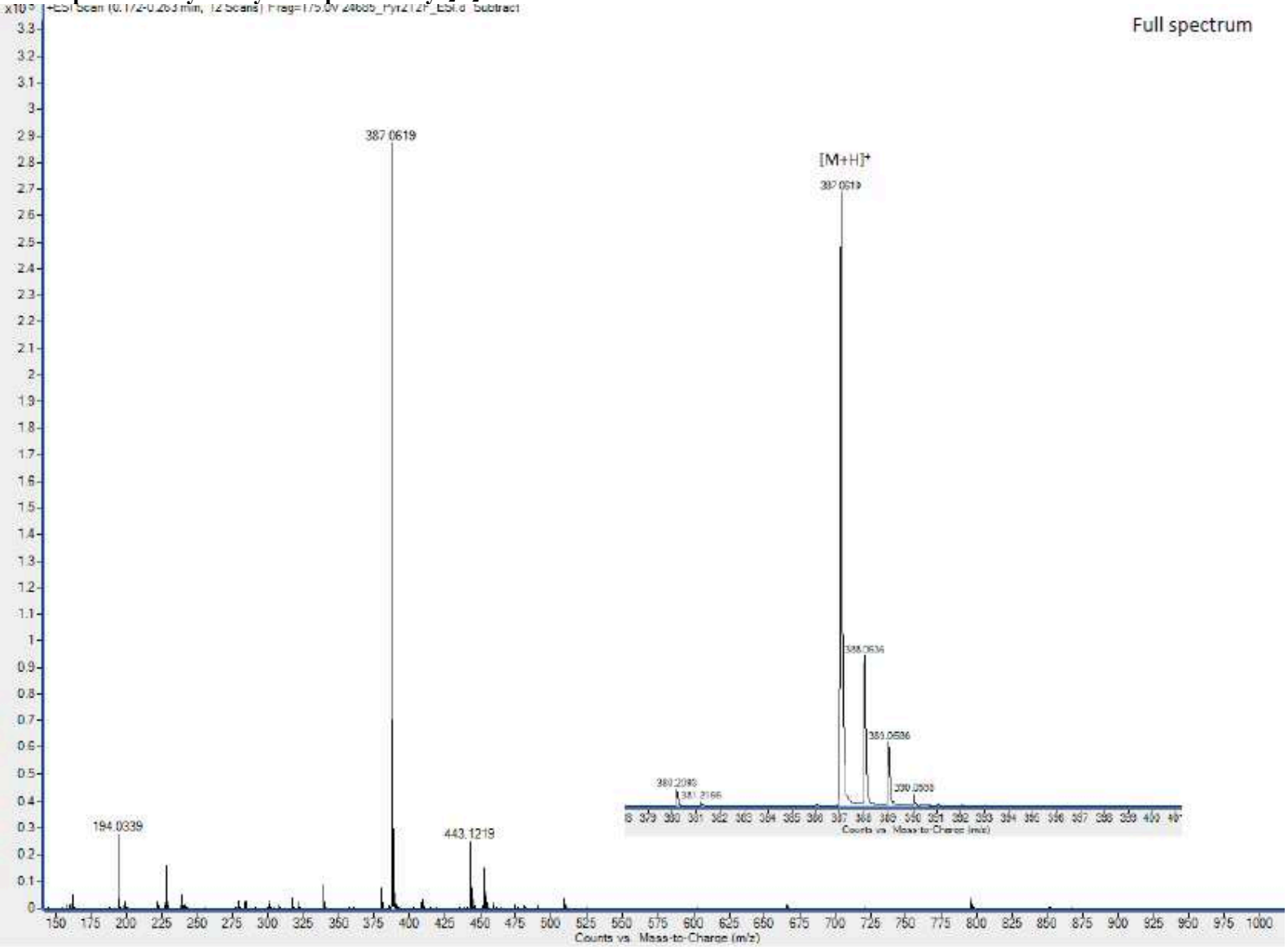

Mass Spectrometry Analysis Report for Pyr_2F_2T

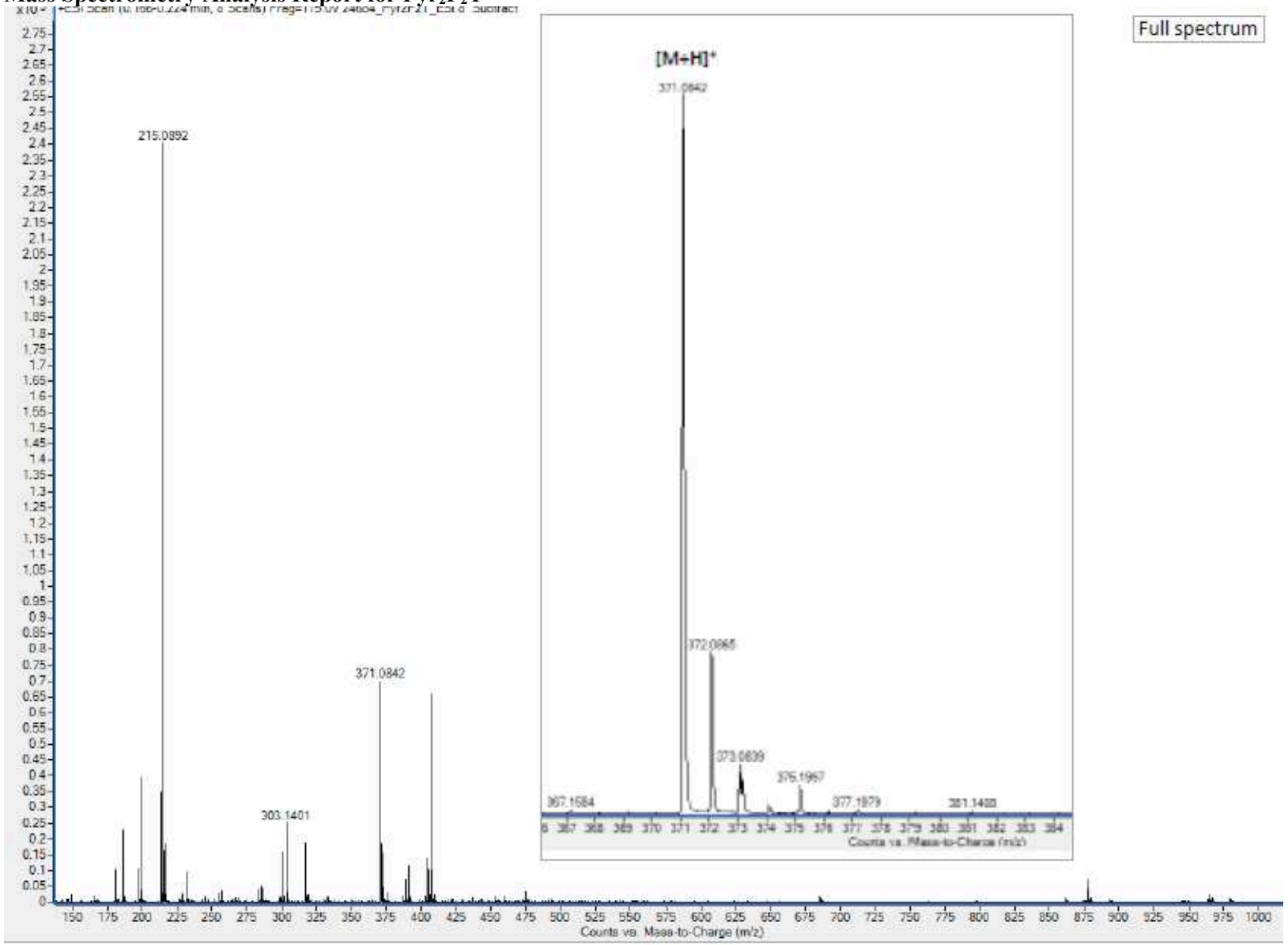

References

1. A. Hucke and M. P. Cava, *The Journal of Organic Chemistry*, 1998, **63**, 7413-7417.
2. P. Arsenyan, E. Paegle and S. Belyakov, *Tetrahedron Letters*, 2010, **51**, 205-208.
3. A. Hayoun Barak, G. de Ruiter, M. Lahav, S. Sharma, O. Gidron, G. Evmenenko, P. Dutta, M. Bendikov and M. E. van der Boom, *Chemistry – A European Journal*, 2013, **19**, 8821-8831.
4. D. Sahu, H. Padhy, D. Patra, D. Kekuda, C.-W. Chu, I. H. Chiang and H.-C. Lin, *Polymer*, 2010, **51**, 6182-6192.
5. Y. Adachi, Y. Ooyama, N. Shibayama and J. Ohshita, *Dalton Transactions*, 2016, **45**, 13817-13826.
6. A. Abbotto, S. Bradamante, A. Facchetti and G. A. Pagani, *The Journal of Organic Chemistry*, 1997, **62**, 5755-5765.
7. S. T. Nguyen, A. L. Rheingold, G. S. Tschumper and D. L. Watkins, *Crystal Growth & Design*, 2016, **16**, 6648-6653.